Title	セルロースナノファイバーの表面修飾による生体材料の開発
Author(s)	袁, 喜達
Citation	
Issue Date	2022-03
Type	Thesis or Dissertation
Text version	ETD
URL	http://hdl.handle.net/10119/17763
Rights	
Description	Supervisor:松村　和明, 先端科学技術研究科, 博士

Development of functional biomaterials using surface modified cellulose nanofibers

by

Yuan Xida

submitted to
Japan Advanced Institute of Science and Technology
in partial fulfillment of the requirements
for the degree of
Doctor of Philosophy

Supervisor: Professor Kazuaki Matsumura

School of Materials Science
Japan Advanced Institute of Science and Technology

March,2022

Abstract

Cellulose nanofiber (CNF) is the most abundant and renewable natural polymer on the planet. Nowadays, since the environmental problems are becoming severe every year, the development of materials based on green materials such as CNF is of great significance. Because of its unique properties such as high specific surface area, high mechanical strength, reactive surface, biocompatibility, biodegradability, and non-toxicity, CNF has become a very attractive biological material. [1] The surface reactivity allows surface modification, hence the modification of cellulose to improve biocompatibility is a very attractive solution. In this dissertation I have used two methods to modify CNF to enhance its adhesion to cells and biodegradability and analyzed the principles of these two methods in order to achieve precise control.

The first method is the grafting of concentrated polymer brushes onto CNF. Polymer brush grafting is a practical surface grafting technique that can easily alter the physical and chemical properties of the surface, such as hydrophilicity, elasticity, and cell adsorption. Concentrated polymer brushes (CPBs), that is, grafted chains at very high concentrations which exhibit unique entropic properties, and CNF grafted with CPBs (CNF-CPBs)can flocculate with cells to form flocs, [2] which is promising as a 3D culture system. There is a possibility that this flocculation phenomenon can be explained by the Derjaguin-Landau-Verwey-Overbeek (DLVO) theory that guides colloidal flocculation, but further proof is needed. According to the DLVO theory, the flocculation phenomenon is influenced by the surface charge and spatial location. Therefore, in Chapter 2, CPBs with different charges were introduced on the CNF surface and co-cultured with cells. The results demonstrated that larger flocs could be obtained at appropriate zeta potentials. In Chapter 3, CNF-CPBs with different fiber lengths were synthesized, and flocculation of the three cell types was observed. Larger flocs are formed in samples of CNF-CPBs with shorter fiber lengths. Equally important was the fact that all three cells exhibited the same flocculation phenomenon. The results proved that flocculation based on CNF-CPBs and cells can be explained by the DLVO theory and has the potential to be applied to a broader range of cell lines. In conclusion, this is the first time the DLVO theory has been used to explain the flocculation phenomenon in cells and CNF-CPBs.

The degradability of materials is also an essential indicator of the adaptability of biomaterials. [3] In this study, the Malaprade reaction introduces dialdehyde into CNF , which can be degraded by the Maillard reaction triggered by the Schiff base reaction of dialdehyde CNF with amino acids in the body. Furthermore, the effect of reaction conditions on the reaction rate, CNF molecular weight, and crystalline index in this series of reactions was systematically investigated in order to better understand and control the degradation behavior of CNF. Briefly, the molecular weight decreased in both the oxidation and decomposition reactions. Crystalline index studies demonstrated that the Malaprade reaction occurred in crystalline region, which leads to a decrease in the crystallization index. While the degradation reaction occurs mainly in the amorphous region, hence the increase in a crystalline index after the degradation reaction.

In this thesis, the biocompatibility of CNF was enhanced by surface grafting of CPBs and triggering the Maillard reaction for CNF based on oxidation of CNF, and the principles of the reaction were explored for precise control.

Keyword: *cellulose nanofiber; concentrated polymer brush; flocculation; DLVO theory; surface charge; fiber length; Malaprade reaction; Maillard reaction*

Reference

[1] Abhishek Pandey. Pharmaceutical and biomedical applications of cellulose nanofibers: a review. *Environmental Chemistry Letters*, pages 1–13, 2021.

[2] Chiaki Yoshikawa, Takashi Hoshiba, Keita Sakakibara, and Yoshinobu Tsujii. Flocculation of cells by cellulose nanofibers modified with concentrated polymer brushes. *ACS Applied Nano Materials*, 1(4):1450–1455, 2018.

[3] Lara Yildirimer and Alexander M Seifalian. Three-dimensional biomaterial degradation—material choice, design and extrinsic factor considerations. *Biotechnology advances*, 32(5):984–999, 2014.

Contents

Chapter 1

General Introduction

1.1 Biomaterials

Biomaterials are generally defined as inert materials designed to interact with biological systems to evaluate, treat, enhance or replace any tissue, organ, or function of the body. [1] Recently, Doherty et al. has proposed a new definition, that is, "A biomaterial is a substance that has been engineered to take a form which, alone or as part of a complex system, is used to direct, by control of interactions with components of living systems, the course of any therapeutic or diagnostic procedure, in human or veterinary medicine." [2]As a comprehensive discipline, biomaterials integrate chemistry, materials science, bioengineering, and medicine. In the past 50 years, the application of biomaterials, including medical and non-medical aspects, has grown to more than 100 billion U.S. dollars. [3]

Modern biomaterials can be traced back to the 1970s when materials were developed to retain the physical properties (mostly) of replacement locations while minimizing toxic reactions. [4]Due to the human body's defense mechanism, when any body material used as an implant enters the human body, it triggers a series of reactions called foreign body reactions. This reaction is similar to the general wound healing reaction, except that the wound healing inflammation will subside on its own, and the foreign body reaction will cause continuous chronic inflammation around the implant. [5]As the trigger point of the foreign body reaction, the step of non-specific protein adsorption is critical. [6]In order to reduce this risk, various metals, ceramics, and other biologically inert tissue reaction materials have been extensively explored and studied, and this is also the first generation of biomaterials. [7]After then, with the advancement of biochemistry, the development of the second generation of biomaterials has focused on biomaterials that can trigger controllable effects and reactions in the physiological environment. [8]Nowadays, for third-generation biomaterials, researchers are exploring biologically-based tissue repair and regeneration methods to stimulate specific cellular responses at the molecular level. More materials such as polymers (natural polymers or synthetic polymers) and composite materials are used in biomaterials, and more and more applications have been developed in tissue engineering scaffolds, sustained drug release, and medical diagnostic imaging. [9–11]The concept of biomaterials has been further expanded, not only for the development of implants but also for drug development or a deeper understanding of life activities. These studies have made outstanding contributions to extending the human life span and improving the quality of life.

1.1.1 Biocompatibility of Biomaterials

The ideal biomaterial should be biocompatible, which was first defined in the 1980s as having an appropriate host response in a specific application. [12]Although the definition is still slightly general, the overall biocompatibility needs to consider the toxicity of the material itself, the components derived from microorganisms, the mechanical properties, and the interaction of the biomaterial with surrounding proteins and cells. [13]Mechanical properties include providing physical support according to different purposes, such as bone repair, blood vessel or *in vitro* culture system, etc., in which biomaterials need to provide physical support for compression or stretching. [14–16] In addition, the microscopic physical structure of biological materials can also provide physical stimulation to cells and trigger particular physiological responses. These reactions are essential for cell growth. [17]

When biological materials come into contact with cells and the cells are physically stimulated, some tissue molecules, especially proteins with high surface activity, get attracted to the material's surface through electrostatic attraction. [18] There are various determinants in protein adsorption, such as the protein molecules' structure, the dehydration of the material surface, the protein distributed at the interface, and the surface structure of the protein. [19] Therefore, protein adsorption is a complicated process due to a combination of many factors.

1.1.2 Modification of Biomaterials

Although the mechanism is complex, effective control of protein adsorption is very important. It is not only the starting point for the foreign body reaction of the implant, as mentioned above. It is also a key determinant of in vitro cell culture, including the subsequent cell adsorption, proliferation, and differentiation processes. [20] Thus, the physical and chemical properties of the surface of biomaterials determine their biocompatibility. Various methods, such as surface polymerization, plasma treatment, peptide grafting. Biomaterials with different properties have been constructed, as shown in Figure 1.1. [21]

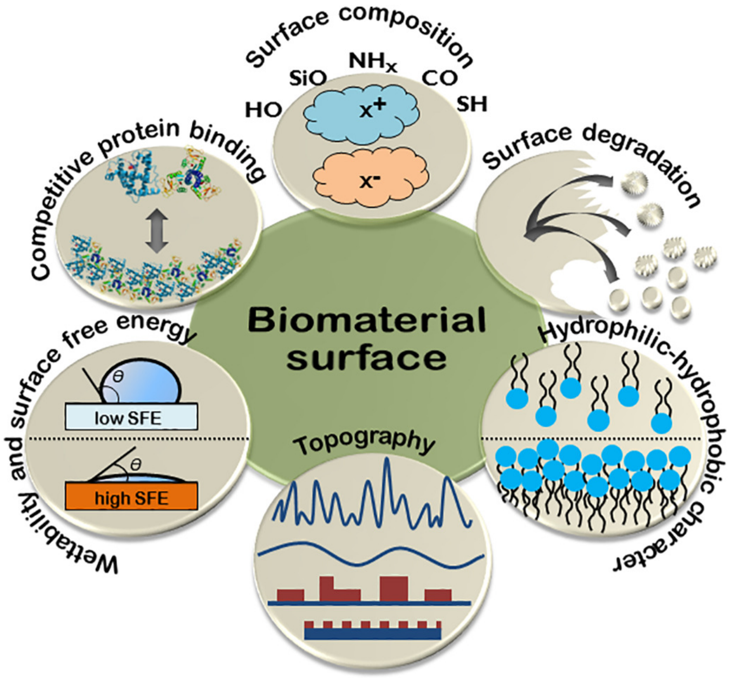

Figure 1.1: Scheme of the key surface parameters and processes in directing biological responses to biomaterials. [21]

One of the essential surface properties is biodegradability. Biodegradable materials do not need to be removed from the living body by means such as surgery, so biological materials have advantages in more applications. [22] For example, for the application of tissue engineering cell scaffolds cultured in vivo or in vitro, after the material is resorbed, there should be no traces of implants or scaffolds, so the defect sites in the body are gradually replaced by the original tissue. [23, 24] And cells cultured in vitro are easier to recover. [25]

In summary, biological adaptability largely depends on Bulk and surface propertity. The polymers used for biomaterials are generally natural or synthetic, while common degradable natural polymers such as polysaccharides and proteins, on the other hand, are degradable synthetic polymers such as polyesters and polyphospholipids. [26] The degradation products of polysaccharides in the biological environment are beneficial to the human body. [27]Many polysaccharides have been developed, such as chitosan, chitin, cellulose and so on, which have been widely used in *in vivo* and *in vitro* cell culture and drug delivery. [28–30]

1.2 Chemical reactions of polysaccharides

Polysaccharides are the most commonly used biological materials and have a wide range of sources in nature. More importantly, polysaccharides have a large number of reactive groups and a wide range of molecular weight, which allows a variety of modifications to be applied. Here, several common reactions related to polysaccharide degradation are introduced.

1.2.1 Malaprade reaction

Periodate can react with adjacent hydroxyl groups in polysaccharides, such as cellulose, to form a dialdehyde group,known as Malaprade reaction. This reaction can be carried out very rapidly under mild conditions. [31]

The Malaprade reaction was first reported in 1928 for compounds with hydroxyl groups on adjacent C atoms. [32] As shown in Figure 1.2, in the first step, a complex of a periodate and an adjacent hydroxyl group is formed. Then, the complex disproportionate to form a dialdehyde and iodate. At the same time, the aldehyde state is not stable and can be rapidly converted to a semi-formaldehyde by reacting with the hydroxyl groups of adjacent unoxidized glyoxal residues in the polymer chain. [33, 34] Furthermore, dialdehydes can be further converted to form different reactive groups. Many biomaterials based on the Malaprade reaction have been successfully developed. [35, 36]

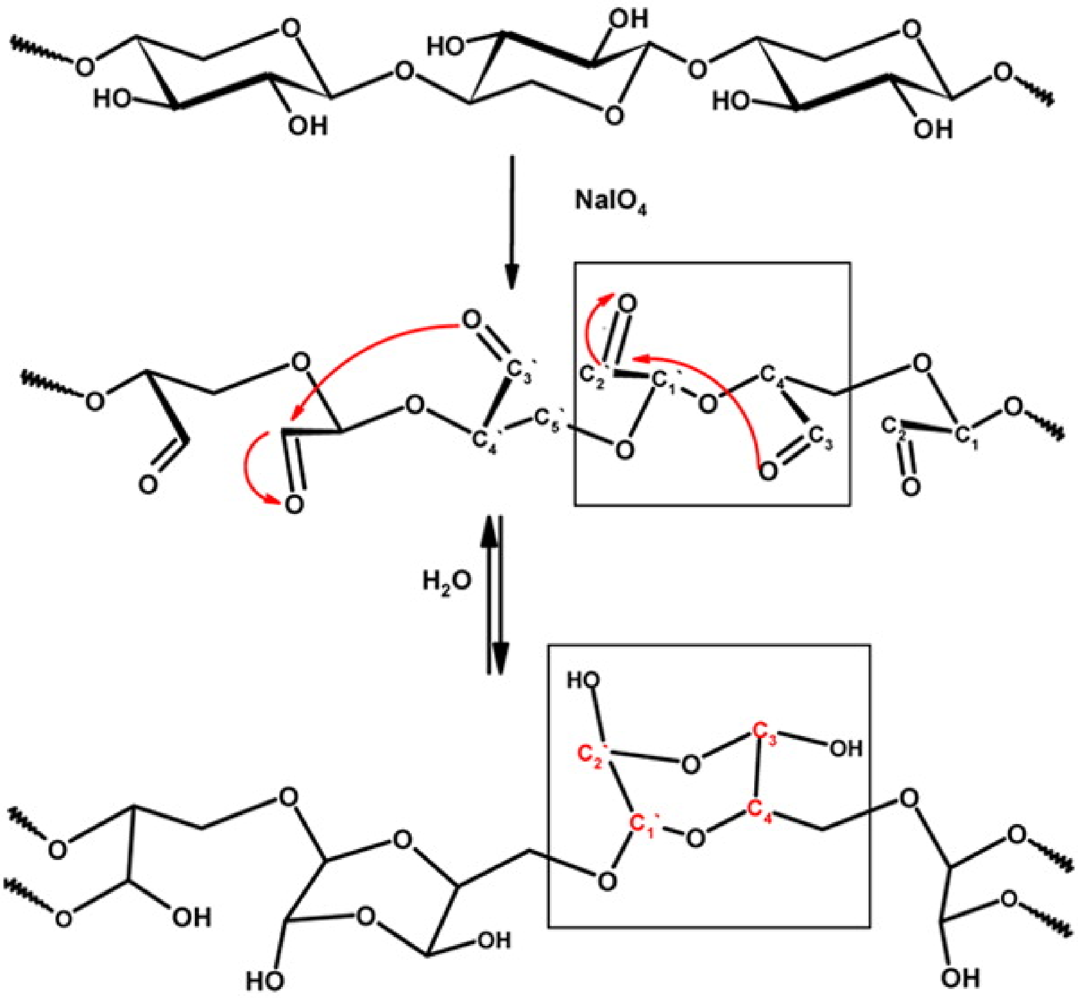

Figure 1.2: General scheme of Malaprade oxidation of polysaccharides. [33]

1.2.2 Schiff base reaction

Schiff bases are compounds containing an imine or methylimine character group (-RC=N-) and are usually formed by the nucleophilic addition of carbonyl-containing aldehydes and ketones to primary amines, as shown in Figure 1.3. This reaction is named after the researcher Hugo Joseph Schiff in honor of his first description of the formation of a Schiff base by the condensation of two aldehydes and amines in equal amounts in 1864. [37]

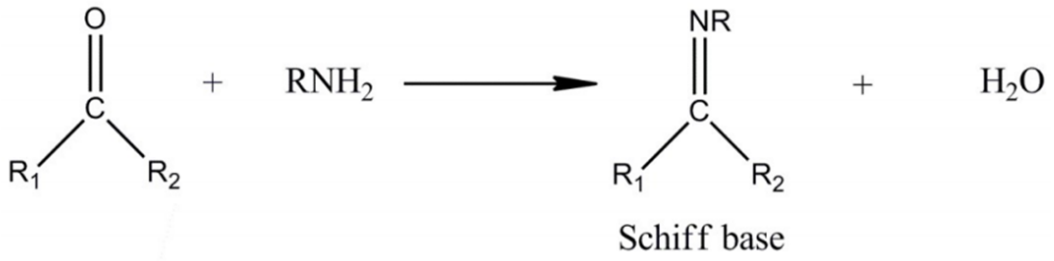

Figure 1.3: The reaction of Schiff base

Schiff bases have a wide range of applications and are of great research value in drug discovery, catalysis and anti-corrosion due to their C=N functional groups and electronic effects. [38, 39] In particular, Schiff bases are among the most commonly used ligands for metal complexes, supporting the flexible design of different metal complexes. [40]

For polysaccharides, the Schiff base reaction involves the cross-linking of a macromolecule containing alcohol, amine, or hydrazide functional group with an aldehyde to form a dynamic covalent imine bond, resulting in a hydrogel network. Another advantage of the Schiff base reaction is that the reaction conditions are mild, and therefore hydrogels with self-healing properties can be made for cell embedding and controlled drug delivery applications. [41] The Schiff base reaction can also be easily triggered on polysaccharides by the dimer produced by the Malaprade reaction. It has been reported that dextran-based hydrogels can be easily developed for drug retardation under mild conditions using the Malaprade and Schiff reactions. [42]

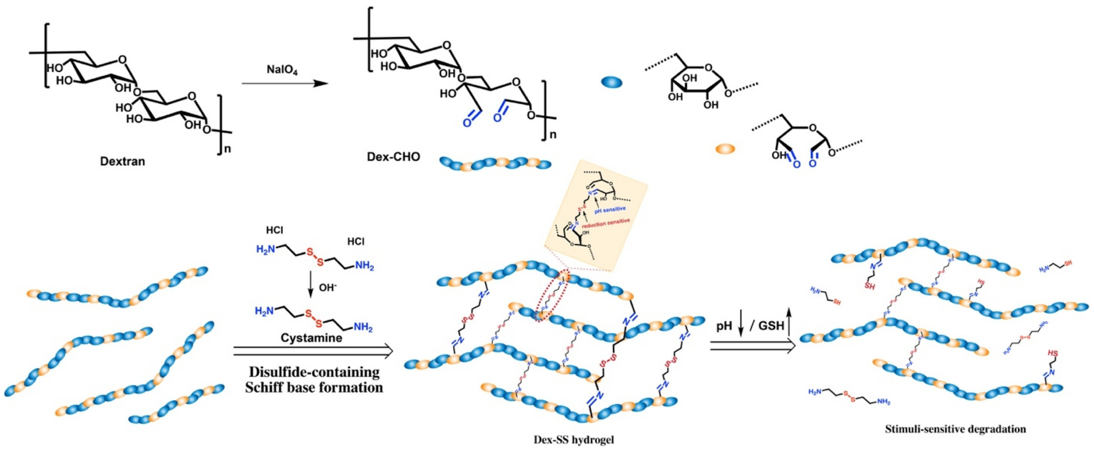

Figure 1.4: Schematic illustration for the formation and stimuli-sensitive degradation of Dex-SS hydrogels synthesized via disulfide-containing Schiff base reactions between polyaldehyde dextran and cystamine. [42]

1.2.3 Maillard reaction

Maillard reaction is a non-enzymatic reaction between the carbonyl group of reducing sugar and the amino group of amino acid, peptide, or protein. The reaction route depends on the type and concentration of reactants, temperature, time, pH, and water activity. [43]

The reaction is divided into three main stages. In the early stages, reducing sugars are condensed with compounds bearing free amino groups to produce N-substituted glycosamines. The N-substituted glycosylamines rearrange to form Amadori rearrangement products (ARP). In subsequent stages, ARP degradation depends on the system pH. When pH ≤ 7, the product is furfural or hydroxymethylfurfural (HMF). At pH > 7, the decomposition of the Amadori compounds consists mainly of a few enolizations to produce 2,3-terminal, dicarbonyl compounds, followed by fission products containing various pyruvic alcohols, pyral, and diacetyl. All these products are highly reactive and participate in further reactions. Among them, dicarbonyl compounds react with amino acids to form aldehydes and alpha-amino ketones. This reaction is known as Strecker degradation. [44]

The final stage undergoes a complex and unclear series of reactions of cyclization, dehydration, reverse porosity expansion, rearrangement, isomerization, and further condensation, culminating in the formation of brown nitrogen-containing polymers and copolymers, collectively referred to as melanoidins. [45]

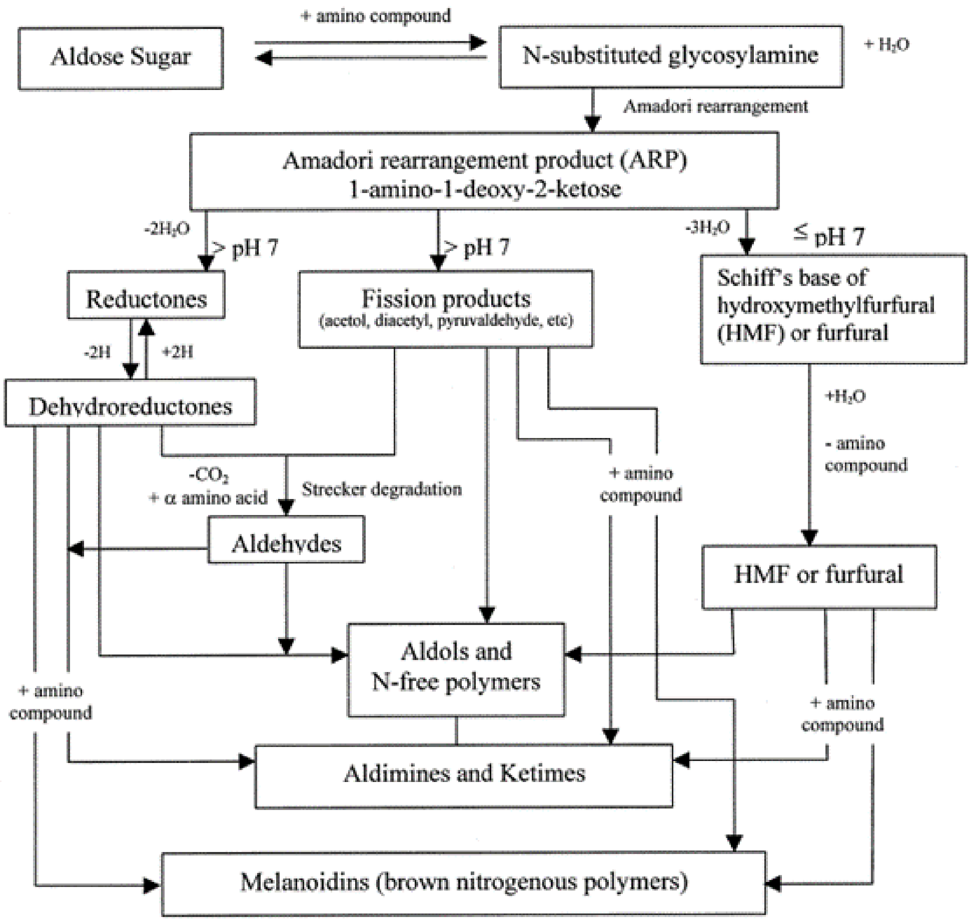

Figure 1.5: Maillard reaction scheme adapted by Hodge. [45]

From previous studies, it is known that the oxidation of dextran and the amine undergo a Schiff base formation reaction, after which the Maillard reaction cleaves the dextran backbone. [46] Figure 1.6(A) shows the Maillard reaction pathway between reducing sugars and amino acids. In particular, Figure 1.6(B) shows the mechanism of molecular cleavage of dextran oxidation due to the reaction with amines. Oxidation of the aldehyde group of the dextrose produces an amino group and a Schiff base (reaction 1). The 1,2-enamine is then produced by Amadori rearrangement (reaction 2). Finally, further degradation shows that the backbone breaks at C5 (reaction 3) and is converted to 1- and 3-deoxy ions. Methylenes are present during the formation of 3-deoxy ions via Amadori rearrangement and lead to Strecker degradation and the formation of melanoidin, which is thought to be responsible for the formation of brown compounds during polysaccharide degradation. [46]

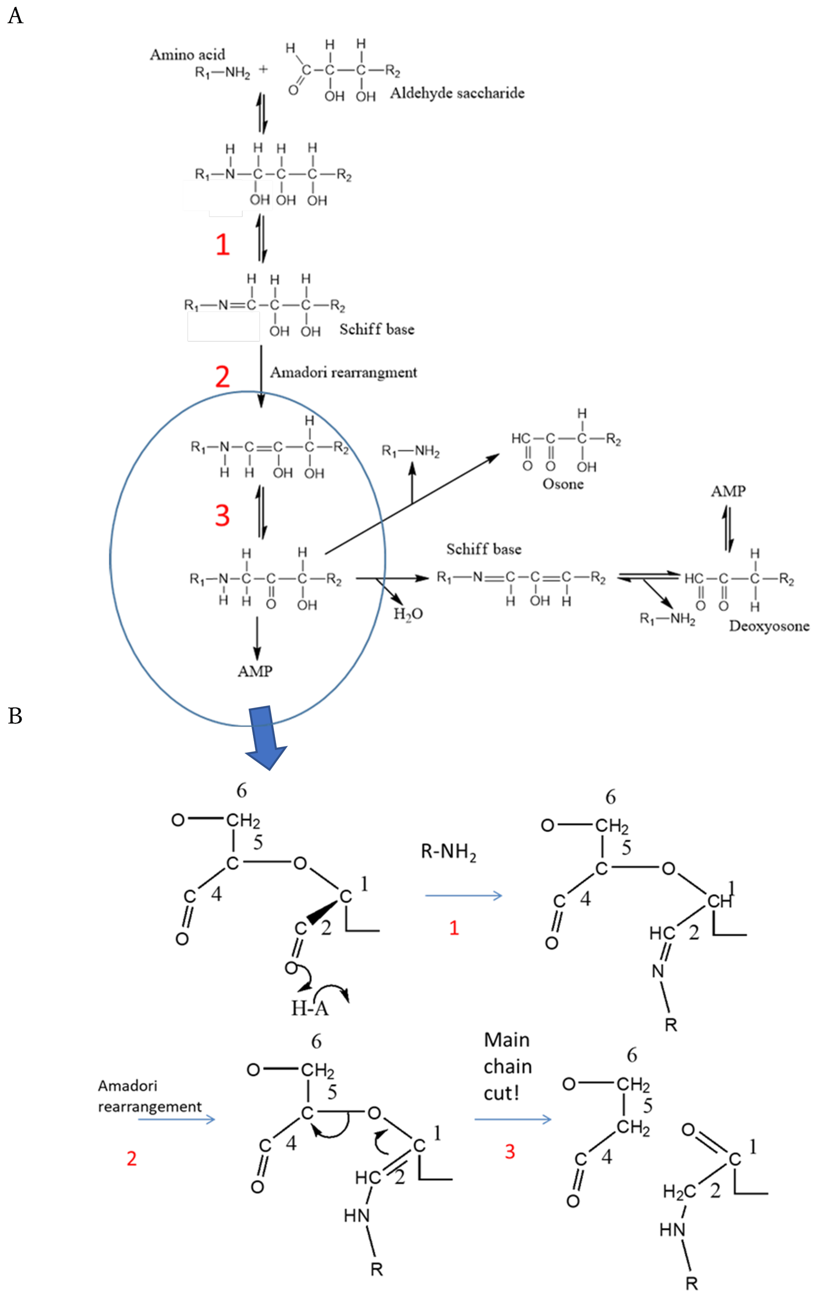

Figure 1.6: (A) Maillard reaction pathway for the reaction of aldehyde saccharides and amino acids. (B) Molecular scission mechanism of oxidized dextran by the reaction with amine

1.3 Cellulose nanofiber (CNF)

1.3.1 Cellulose

In 1838, French chemist Anselme Payen revealed by elemental analysis that the resistant fibrous solids that remain after processing various plant tissues are of the molecular formula represented by C6H10O5. [47]The following year, in 1839, this plant component was first described as "cellulose" in a study submitted by Payan to the French Academy of Sciences. [48]

Cellulose is ubiquitous in plant cell walls and is its most important structural and reinforcing component. It is the most abundant natural polymer on earth, also found in bacteria, fungi, algae, amoebae, and aquatic organisms, and consists of repeating units of D-glucose linked by β-1,4 bonds Figure (1.7). Unlike starch and other polysaccharides, the glucose units in cellulose are linked by β-1,4 glucosidic bonds, and the hydroxyl groups other than the 1,4 position are hydrogen-bonded within and between molecules resulting in a plate-like molecules arrangement. Hydrogen bonding in cellulose affects the solubility, swelling, and critical physical properties of the cellulose structure. [49]

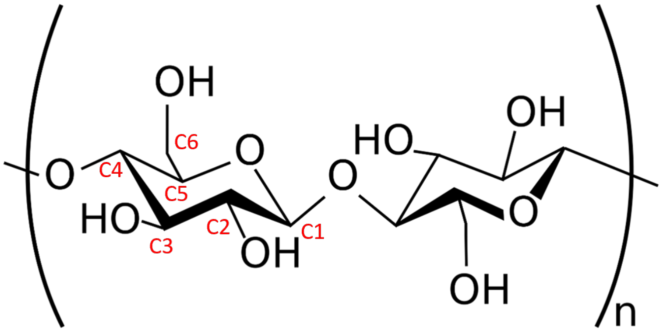

Figure 1.7: Structural formula of cellulose

It is interesting to note that although two dehydrated glucose units make up a dehydrated cellulose disaccharide, which forms the repeating unit of a cellulose polymer. However, the degree of cellulose polymerisation (DP) is usually expressed as the number of dehydrated glucose units. Each dehydrated glucose unit has three hydroxyl groups (on the C2, C3 and C6 atoms), which give the cellulose molecule a high degree of functionality. Reactions using hydroxyl groups include esterification, etherification, selective oxidation, graft copolymerization, and intermolecular crosslinking, as shown in 1.8. [50]

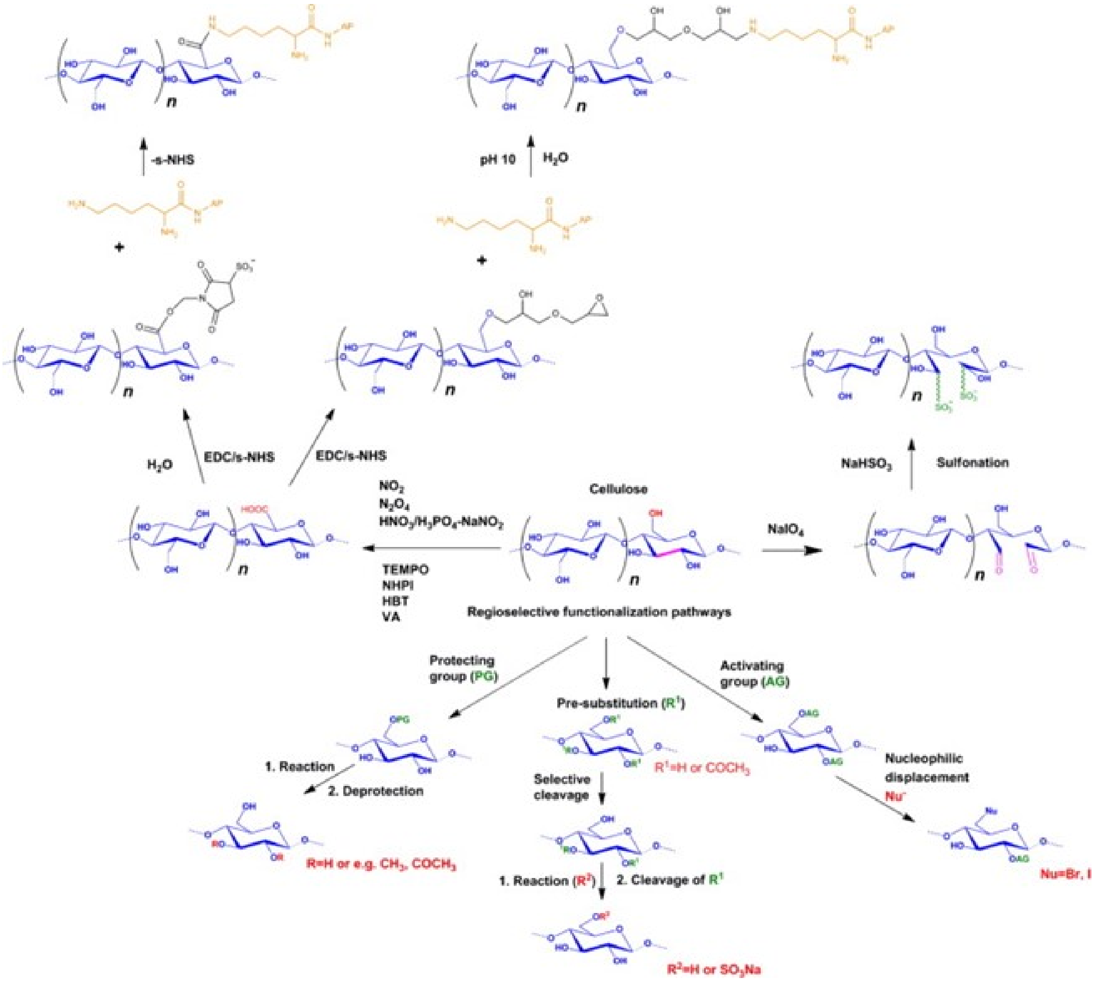

Figure 1.8: Selected pathways for regioselective functionalization of cellulose. [50]

1.3.2 CNF

Cellulose particles with at least one-dimensional nanoscale (1-100 nm) are denoted as nanocellulose. With high strength and stiffness, low weight, and biodegradability, nanocellulose is a promising candidate for the production of bio-nano materials. Generally nanocellulose includes cellulose nanocrystals (CNC) and cellulose nanofibres (CNF), which are primarily of plant origin, and bacterial cellulose (BC), which is produced by bacteria. [51]

BC can be manufactured by a variety of bacteria in a medium containing glycogen and has the advantage of not requiring the presence of plant-derived impurities such as lignin. [52] However, the large-scale production of BC is a great challenge due to the need for bottom-up synthesis from starting glycogen in appropriate culture dishes. [51] CNC fabrication was first reported in 1949 as a rigid material in the form of nanoscale rods obtained by dissolving amorphous areas through acid treatment. [53]

CNF is an excellent renewable material, typically made by mechanical decomposition, with a diameter of approximately 10-50 nm and a length of over 500 nm. [54] CNF has a higher aspect ratio than CNC and can be obtained in different lengths depending on the source. [55] In recent years, the development of pre-treatments such as TEMPO oxidation and enzymatic treatment has facilitated mechanical decomposition, allowing CNF to be produced at a further reduced cost and with more excellent commercial attractiveness. [56,57] CNF also has a structure similar to that of natural ECM. There have been reports in the past that CNF suspension can support cell growth. [58] CNF is, therefore, very promising as a biomaterial. However, CNF has some drawbacks, such as the very low degradability of CNF in vivo, which limits its application as an implant, and the lack of protein binding sites on CNF, making it difficult for cells to attach to CNF. [59,60] In this research, I expect to improve the biocompatibility of this promising material by improving the shortcomings of CNF to expand its application as a biomaterial.

1.4 Surface modification

As mentioned above, surface properties are significant for the biocompatibility and functionality of biomaterials. Due to the diversity of functions, polymers can be used for surface modification to provide hydrophilicity, adhesion, colloidal stabilization, biological activity. [61–63]

There are two general techniques for surface modification with polymers, namely physisorption and covalent bonding. In general, covalent bonding is more attractive as it allows for a higher graft density and does not have the disadvantages of physisorption, such as low thermal stability. [64] Polymers introduced by covalent bonding are also referred to as grafting. Polymers have been grafted onto planes, nanoparticles, or other natural or artificial polymers. [65] For grafting on the solid surface, the configuration in the solution changes as the grafting density increases. [66] At low grafting density, since the distance between the grafting sites is greater than the size of the chain, the grafted polymer chains will not overlap, and there will be almost no mutual influence, thus presenting the so-called "pancake" or "mushroom" conformations. Grafted chains are pulled away from the surface to form a brush as the grafting density increases due to the repulsive force between the grafted chains as shown in Figure1.9. [67]

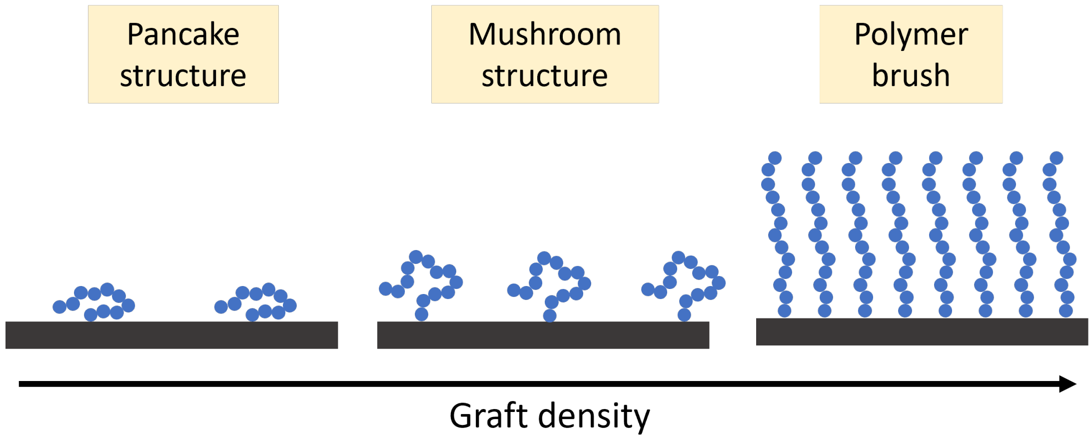

Figure 1.9: The conformation of the graft on the substrate surface changes with the graft density.

The polymer brush is a remarkable structure in which one end of the long-chain polymer molecule is tied to the surface or interface, and the other end is stretched due to volume repulsion. [68] Based on the adjustment of the thickness and chemical composition of polymer brushes, polymer brushes have been widely used in lubrication, biomedical surfaces, colloidal stability, and other directions. [69, 70] There have been many reports on the use of polymer brushes for cellulose. Carry out surface modification to obtain better water solubility and cell adsorption. [71, 72]

1.4.1 surface-initiated atom transfer radical polymerization (SI-ATRP)

There are two common ways to graft polymers to surfaces or substrates, the "graft-to method", and the "graft-from" method (Figure 1.10). [64] The graft-to method involves the synthesis of a free polymer and then anchoring the polymer by reacting the functional groups at the end of the polymer with the surface. The advantage of this method is that the polymer is pre-polymerized, and therefore the grafted polymer can be easily characterized. However, higher density polymer brushes are difficult to achieve as the polymer grafted first strongly prevents grafting of subsequent polymers. In contrast, a bottom-up grafting approach (graft-from) can overcome the spatial barrier between polymers to allow for higher concentrations of polymer brushing. [73]

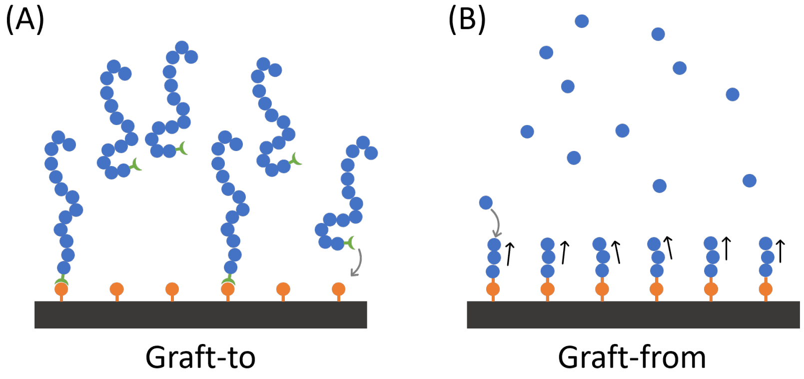

Figure 1.10: Representative preparation strategies of polymer brushes: (A) graft-to method, (B) graft-from method.

Various polymerization techniques such as ring-opening polymerization, anionic polymerization, cationic polymerization, and living radical polymerization (LRP) have been utilized for this grafting method. [74, 75] However, ring-opening, anionic and cationic polymerization methods are limited by the harsh reaction conditions and water-sensitive catalysts. [76] The most widespread of these is living radical polymerisation (LRP), owing to its tolerance to impurities and versatility for various monomers. [77] Recent studies have also shown that surface-initiated LRP can substantially increase the graft density and form well-defined higher concentrations of polymer brushes. [78, 79]

Among the surface-initiated LRPs, a large number of reports indicate that surface-initiated atom transfer radical polymerization (SI-ATRP) is the most widely used technique because it does not require complicated operation steps and can obtain controllable polymer brushes. [74, 77, 80, 81] The first surface-initiated polymerization (SI-ATRP) using ATRP technology was reported in 1997. Cu(I)/bpy was used as a catalytic system and successfully grafted poly(acrylamide) (PAM) brush onto silica gel. [82]

Atom Transfer Radical Polymerization (ATRP) is a particularly attractive method of grafting polymer brushes. Compared with other controllable polymerization methods, ATRP has fewer restrictions on its use; for example, it can provide the possibility of polymerizing a variety of monomers in water, ambient temperature, and other conditions, and at the same time has high kinetics. [75] Generally, ATRP is carried out by transition metal complexes with redox activity (most commonly copper catalysts). As shown in Figure 1.11 The copper catalyst Cu(I)/ligand in the lower oxidation state reacts with the initiator (haloalkane), resulting in the production of active free radicals and Cu(II)/ligand. The formed free radicals react with the monomer to initiate polymerization. At the same time, the active free radicals can also make the growing free-radical chain dormant by reacting with the higher oxidation state of Cu(II)/ligand. This activation and dormancy are repeated randomly at all sites, so macroscopically, all polymer chains grow slowly simultaneously, hence they are controllable. [83] When the initiator is fixed on the surface of the substrate, it can initiate SI-ATRP to obtain highly controllable graft chains with uniform lengths.

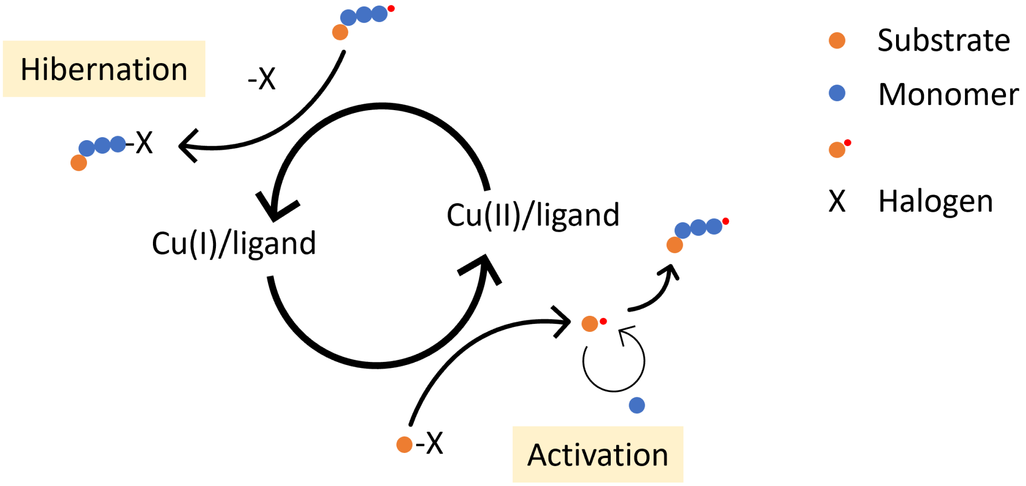

Figure 1.11: General mechanism of ATRP.

1.4.2 Concentrated polymer brushes (CPB)

For polymer brushes, new definitions have been made according to different graft densities (σ). Among them, a highly concentrated polymer brush (CPB) based on SI-ATRP has been reported. Compared to the typical semi-dilute polymer brush (SDPB), the graft density (σ) in a highly-concentrated polymer brush is more than an order of magnitude higher and displays unique characteristics, that is clearly different from that of SDPB. [77, 84, 85]

Among two types of polymer brushes, the folding state of the graft chains can be seen in the relationship between the length of the graft chains and the degree of polymerization. For polymer brushes, σ influences the surface extension of the graft chains and thus their physical properties. [86] σ is defined as the number of grafted polymer chains per unit area of the substrate surface. Theoretically, as σ increases, the graft chains get closer to each other, and the effect of steric hindrance extends the graft chains further. [74] Theoretical studies have reported that the relationship between the length of the graft chain and σ is summarized as

$$h \propto N\sigma^k \tag{1.1}$$

Where h is the average length of the polymerization brush, N is the degree of polymerization and k is the exponent of σ, usually between 0 to 1, depending on σ and solvent. [87, 88] In suitable solvents, SDPB has a k value of 1/3, while CPB can reach an impressive 1. [77, 84, 85] It can be seen here that the graft chain of CPB is almost fully extended in suitable solvents. Thus, it has an extremely high compression resistance, superlubricity, and size rejection effects. [77, 85, 89] Based on its unique physicochemical properties, many applications have been developed in recent years based on CPB, such as anti-fouling, antibacterial, and cell culture. [90–92]

It has also been reported that introducing anionic polymers into CNF through SI-ATRP can introduce unique entropic properties to CNF and effectively facilitate the adsorption of CNF to cells and the occurrence of cellular flocculation. [71] This flocculation phenomenon seems to be explained by the Derjaguin-Landau-Verwey-Overbeek (DLVO) theory, according to which the interaction forces between charged indications can be considered as a balance between van der Waals(vdW) and electrostatic forces. [93] Although initially used to explain colloidal stability, the DLVO theory has been widely used to explain the phenomenon of bacterial adsorption, in which the bacterial cell is treated as a colloidal particle. [94] A large number of materials for bacterial adsorption have been developed based on this approach. [95–97] For the phenomenon of cell flocculation with adsorbent polymers, such as CPB-grafted CNF, can be explained by the DLVO theory when cells are considered as colloidal particles; it provide a fascinating guide for the development of new 3D cell culture methods.

1.5 Research purpose

Despite its many advantages in the biomedical field, CNF's low cytosolic adsorption and inability to degrade *in vivo* limit its application. In previous studies, CPB-grafted CNF exhibited good cytosolic adsorption and was able to flocculate with cells and enhance cellular function. The DLVO theory may provide a theoretical explanation for this phenomenon. In this study, I examined this idea. If the cell flocculation phenomenon of CNF-CPBs can be explained by the DLVO theory, it will provide a clear theoretical guidance for the application of CNF-CPBs as biomaterials, especially for the development of 3D cell culture methods. According to the DLVO theory, the flocculation phenomenon is related to the surface charge and the molecular weight (fibre length) as a flocculant. Therefore, the effects of surface charge and different fibre lengths on flocculation phenomena are investigated in Chapters 2 and 3, respectively, and explained using DLVO theory. Finally, the degradation mechanism of CNF was investigated using the Malaprade reaction and is presented in Chapter 4. It is expected that the application of CNF-CPB as biomass material will be further broadened in the future by endogenous degradation empowerment.

Reference

[1] P. J. Doherty, R. L. Williams, D. F. Williams, and A. J. C. Lee. Bioinaterials-tissue interfaces, 1992.

[2] D. F. Williams. On the nature of biomaterials. *Biomaterials*, 30(30):5897–5909, 2009.

[3] B. D. Ratner and S. J. Bryant. Biomaterials: where we have been and where we are going. *Annu. Rev. Biomed. Eng.*, 6:41–75, 2004.

[4] L. L. Hench. Biomaterials. *Science*, 208:826–831, 1980.

[5] J. M. Anderson, A. Rodriguez, and D. T. Chang. Foreign body reaction to biomaterials. In *Seminars in Immunology*, volume 20, pages 86–100. Elsevier, 2008.

[6] T. N. Salthouse. Some aspects of macrophage behavior at the implant interface. *Journal of Biomedical Materials Research*, 18(4):395–401, 1984.

[7] L. L. Hench and I. Thompson. Twenty-first century challenges for biomaterials. *Journal of the Royal Society Interface*, 7:S379–S391, 2010.

[8] L. L. Hench and J. Wilson. Surface-active biomaterials. *Science*, 226(4675):630–636, 1984.

[9] H. Ueno, T. Mori, and T. Fujinaga. Topical formulations and wound healing applications of chitosan. *Advanced Drug Delivery Reviews*, 52(2):105–115, 2001.

[10] X. Li, L. Wang, X. Yu, Y. Feng, C. Wang, K. Yang, and D. Su. Tantalum coating on porous ti6al4v scaffold using chemical vapor deposition and preliminary biological evaluation. *Materials Science and Engineering: C*, 33(5):2987–2994, 2013.

[11] X. Zhao, Q. Lang, L. Yildirimer, Z. Lin, W. Cui, N. Annabi, K. W. Ng, A. M. Dokmeci, M. R.and Ghaemmaghami, and A. Khademhosseini. Photocrosslinkable gelatin hydrogel for epidermal tissue engineering. *Advanced Healthcare Materials*, 5(1):108–118, 2016.

[12] Da. F. Williams. *Definitions in biomaterials: proceedings of a consensus conference of the European Society for Biomaterials, Chester, England, March 3-5, 1986*, volume 4. Elsevier Science Limited, 1987.

[13] B. D. Ratner and F. J. Schoen. the concept and assessment of biocompatibility. *Biomaterials Science: An Introduction to Materials in Medicine (3rd ed.)*, pages 588–592, 2013.

[14] C. Paredes, F. J. Martínez-Vázquez, A. Pajares, and P.o Miranda. Co-continuous calcium phosphate/polycaprolactone composite bone scaffolds fabricated by digital light processing and polymer melt suction. *Ceramics International*, 47(12):17726–17735, 2021.

[15] S. Ravi and E. L. Chaikof. Biomaterials for vascular tissue engineering. *Regenerative medicine*, 5(1):107–120, 2010.

[16] Q. Hu, X. Liu, H. Liu, L. Yang, X. Yuan, Y. Chen, W. Wu, J. Luo, J. Long, M. Huang, and M. Guo. 3d printed porous microgel for lung cancer cells culture in vitro. *Materials & Design*, 210:110079, 2021.

[17] T. Iskratsch, H. Wolfenson, and M. P. Sheetz. Appreciating force and shape—the rise of mechanotransduction in cell biology. *Nature reviews Molecular cell biology*, 15(12):825–833, 2014.

[18] R. E. Baier and R. C. Dutton. Initial events in interactions of blood with a foreign surface. *Journal of Biomedical Materials Research*, 3(1):191–206, 1969.

[19] L. Xu and C. A. Siedlecki. Effects of surface wettability and contact time on protein adhesion to biomaterial surfaces. *Biomaterials*, 28(22):3273–3283, 2007.

[20] N. Nath, J. Hyun, H. Ma, and A. Chilkoti. Surface engineering strategies for control of protein and cell interactions. *Surface Science*, 570(1-2):98–110, 2004.

[21] M. Jurak, A. E. Wiacek, A. Ladniak, K. Przykaza, and K. Szafran. What affects the biocompatibility of polymers? *Advances in Colloid and Interface Science*, page 102451, 2021.

[22] T. S. Anirudhan, V. Manjusha, and V. ChithraSekhar. A new biodegradable nano cellulose-based drug delivery system for ph-controlled delivery of curcumin. *International Journal of Biological Macromolecules*, 2021.

[23] Y. B. Ji, J. Y. Park, Y. Kang, S. Lee, H. J. Ju, S. Choi, B. Y. Lee, and M. S. Kim. Scaffold printing using biodegradable poly (1, 4-butylene carbonate) ink: printability, in vivo physicochemical properties, and biocompatibility. *Materials Today Bio*, 12:100129, 2021.

[24] Y. Nie, G. Chen, H. Peng, S. Tang, Z. Zhou, F. Pei, and B. Shen. In vitro and 48 weeks in vivo performances of 3d printed porous fe-30mn biodegradable scaffolds. *Acta Biomaterialia*, 121:724–740, 2021.

[25] S. Anju, N. Prajitha, V. S. Sukanya, and P. V. Mohanan. Complicity of degradable polymers in health-care applications. *Materials Today Chemistry*, 16:100236, 2020.

[26] K. M. Colvin, V. D. Gordon, K. Murakami, B. R. Borlee, D. J. Wozniak, G. C. L. Wong, and M. R. Parsek. The pel polysaccharide can serve a structural and protective role in the biofilm matrix of pseudomonas aeruginosa. *PLoS pathogens*, 7(1):e1001264, 2011.

[27] M. M. H. Huisman, H. A. Schols, and A. G. J. Voragen. Enzymatic degradation of cell wall polysaccharides from soybean meal. *Carbohydrate Polymers*, 38(4):299–307, 1999.

[28] M. L. Pita-López, G. Fletes-Vargas, H. Espinosa-Andrews, and R. Rodríguez-Rodríguez. Physically cross-linked chitosan-based hydrogels for tissue engineering applications: A state-of-the-art review. *European Polymer Journal*, 145:110176, 2021.

[29] M. Khajavian, V. Vatanpour, R. Castro-Muñoz, and G. Boczkaj. Chitin and derivative chitosan-based structures-preparation strategies aided by deep eutectic solvents: A review. *Carbohydrate Polymers*, page 118702, 2021.

[30] A. A. Shefa, J. Amirian, H. J. Kang, S. H. Bae, H. Jung, H. Choi, S. Y. Lee, and B. Lee. In vitro and in vivo evaluation of effectiveness of a novel tempo-oxidized cellulose nanofiber-silk fibroin scaffold in wound healing. *Carbohydrate polymers*, 177:284–296, 2017.

[31] V. A. Dyatlov, I. S. Kruppa, S. A. Mamaeva, I. Y. Kutergina, V. I. Gumnikova, T. A. Grebeneva, and V. V. Kireev. Change of polysaccharide molecular-weight

distribution and fraction homogeneity after periodate oxidation. *Chemistry of natural compounds*, 50(6):973–977, 2014.

[32] L. Malaprade. Action of polyalcohols on periodic acid. analytical application. *Bulletin de la Societe Chimique de France*, 43:683–696, 1928.

[33] H. Amer, T. Nypelo, I. Sulaeva, M. Bacher, U. Henniges, A. Potthast, and T. Rosenau. Synthesis and characterization of periodate-oxidized polysaccharides: dialdehyde xylan (dax). *Biomacromolecules*, 17(9):2972–2980, 2016.

[34] A. D. Rogalsky, H. J. Kwon, and P. Lee-Sullivan. Compressive stress–strain response of covalently crosslinked oxidized-alginate/n-succinyl-chitosan hydrogels. *Journal of Biomedical Materials Research Part A*, 99(3):367–375, 2011.

[35] V. Verma, P. Verma, P. Ray, and A. R. Ray. 2, 3-dihydrazone cellulose: Prospective material for tissue engineering scaffolds. *Materials Science and Engineering: C*, 28(8):1441–1447, 2008.

[36] B. Gupta, M. Tummalapalli, B. L. Deopura, and M. S. Alam. Functionalization of pectin by periodate oxidation. *Carbohydrate polymers*, 98(1):1160–1165, 2013.

[37] H. Schiff. Mittheilungen aus dem universitätslaboratorium in pisa: eine neue reihe organischer basen. *Justus Liebigs Annalen der Chemie*, 131(1):118–119, 1864.

[38] X. Feng, D. Li, J. Han, X. Zhuang, and J. Ding. Schiff base bond-linked polysaccharide–doxorubicin conjugate for upregulated cancer therapy. *Materials Science and Engineering: C*, 76:1121–1128, 2017.

[39] H. Ashassi-Sorkhabi, B. Shaabani, and D. Seifzadeh. Corrosion inhibition of mild steel by some schiff base compounds in hydrochloric acid. *Applied Surface Science*, 239(2):154–164, 2005.

[40] W. Radecka-Paryzek, V. Patroniak, and J. Lisowski. Metal complexes of polyaza and polyoxaaza schiff base macrocycles. *Coordination Chemistry Reviews*, 249(21-22):2156–2175, 2005.

[41] J. Xu, Y. Liu, and S. Hsu. Hydrogels based on schiff base linkages for biomedical applications. *Molecules*, 24(16):3005, 2019.

[42] H. Su, R. Zheng, L. Jiang, N. Zeng, K. Yu, Y. Zhi, and S. Shan. Dextran hydrogels via disulfide-containing schiff base formation: Synthesis, stimuli-sensitive degradation and release behaviors. *Carbohydrate Polymers*, 265:118085, 2021.

[43] I. G. Hwang, H. Y. Kim, K. S. Woo, J. Lee, and H. S. Jeong. Biological activities of maillard reaction products (mrps) in a sugar–amino acid model system. *Food Chemistry*, 126(1):221–227, 2011.

[44] J. E. Hodge. Dehydrated foods, chemistry of browning reactions in model systems. *Journal of agricultural and food chemistry*, 1(15):928–943, 1953.

[45] S. I. F. S. Martins, W. M. F. Jongen, and M. A. J. S. Van Boekel. A review of maillard reaction in food and implications to kinetic modelling. *Trends in food science & technology*, 11(9-10):364–373, 2000.

[46] W. Chimpibul, T. Nagashima, F. Hayashi, N. Nakajima, S. H. Hyon, and K. Matsumura. Dextran oxidized by a malaprade reaction shows main chain scission through a maillard reaction triggered by schiff base formation between aldehydes and amines. *Journal of Polymer Science Part A: Polymer Chemistry*, 54(14):2254–2260, 2016.

[47] A. Payen. Mémoire sur la composition du tissu propre des plantes et du ligneux. *Comptes Rendus*, 7:1052–1056, 1838.

[48] A. Brogniart, A. B. Pelonze, and R. Dumas. Report on a memoir of m. payen, on the composition of the woody nature. *Comptes Rendus*, 8:51–53, 1839.

[49] Y. Zhang, T. Nypelö, C. Salas, J. Arboleda, I. C. Hoeger, and O. J. Rojas. Cellulose nanofibrils. *Journal of Renewable Materials*, 1(3):195–211, 2013.

[50] J. Liu, S. Willför, and C. Xu. A review of bioactive plant polysaccharides: Biological activities, functionalization, and biomedical applications. *Bioactive Carbohydrates and Dietary Fibre*, 5(1):31–61, 2015.

[51] O. Nechyporchuk, M. N. Belgacem, and J. Bras. Production of cellulose nanofibrils: A review of recent advances. *Industrial Crops and Products*, 93:2–25, 2016.

[52] D. Klemm, D. Schumann, U. Udhardt, and S. Marsch. Bacterial synthesized cellulose—artificial blood vessels for microsurgery. *Progress in polymer science*, 26(9):1561–1603, 2001.

[53] B. G. Ranby. Aqueous colloidal solutions of cellulose micelles, 1949.

[54] Y. Habibi, L. A. Lucia, and O. J. Rojas. Cellulose nanocrystals: chemistry, self-assembly, and applications. *Chemical reviews*, 110(6):3479–3500, 2010.

[55] I. Siró and D. Plackett. Microfibrillated cellulose and new nanocomposite materials: a review. *Cellulose*, 17(3):459–494, 2010.

[56] M. Henriksson, G. Henriksson, L. A. Berglund, and T. Lindström. An environmentally friendly method for enzyme-assisted preparation of microfibrillated cellulose (mfc) nanofibers. *European polymer journal*, 43(8):3434–3441, 2007.

[57] T. Saito, Y. Nishiyama, J. Putaux, M. Vignon, and A. Isogai. Homogeneous suspensions of individualized microfibrils from tempo-catalyzed oxidation of native cellulose. *Biomacromolecules*, 7(6):1687–1691, 2006.

[58] M. Bhattacharya, M. M. Malinen, P. Lauren, Y. Lou, S. W. Kuisma, L. Kanninen, M. Lille, A. Corlu, C. GuGuen-Guillouzo, O. Ikkala, Laukkanen A., Urtti A., and M Yliperttula. Nanofibrillar cellulose hydrogel promotes three-dimensional liver cell culture. *Journal of Controlled Release*, 164(3):291–298, 2012.

[59] K. Madub, N. Goonoo, F. Gimié, I. A. Arsa, H. Schönherr, and A. Bhaw-Luximon. Green seaweeds ulvan-cellulose scaffolds enhance in vitro cell growth and in vivo angiogenesis for skin tissue engineering. *Carbohydrate Polymers*, 251:117025, 2021.

[60] R. Kummala, D. Soto Veliz, Z. Fang, W. Xu, T. Abitbol, C. Xu, and M. Toivakka. Human dermal fibroblast viability and adhesion on cellulose nanomaterial coatings: influence of surface characteristics. *Biomacromolecules*, 21(4):1560–1567, 2020.

[61] C. G. Gölander, S. Jönsson, T. Vladkova, P. Stenius, and J. C. Eriksson. Preparation and protein adsorption properties of photopolymerized hydrophilic films containing n-vinylpyrrolidone (nvp), acrylic acid (aa) or ethyleneoxide (eo) units as studied by esca. *Colloids and surfaces*, 21:149–165, 1986.

[62] L. Moroni, M. K. Gunnewiek, and E. M. Benetti. Polymer brush coatings regulating cell behavior: Passive interfaces turn into active. *Acta Biomaterialia*, 10(6):2367–2378, 2014.

[63] J. M. Anderson. The future of biomedical materials. *Journal of Materials Science: Materials in Medicine*, 17(11):1025–1028, 2006.

[64] B. Zhao and W. J. Brittain. Polymer brushes: surface-immobilized macromolecules. *Progress in Polymer Science*, 25(5):677–710, 2000.

[65] J. C. Foster, S. C. Radzinski, and J. B. Matson. Graft polymer synthesis by raft transfer-to. *Journal of Polymer Science Part A: Polymer Chemistry*, 55(18):2865–2876, 2017.

[66] A. Halperin, M. Tirrell, and T. P. Lodge. Tethered chains in polymer microstructures. *Macromolecules: Synthesis, Order and Advanced Properties*, pages 31–71, 1992.

[67] G. Liu, L. Yan, X. Chen, and G. Zhang. Study of the kinetics of mushroom-to-brush transition of charged polymer chains. *Polymer*, 47(9):3157–3163, 2006.

[68] S. T. Milner. Polymer brushes. *Science*, 251(4996):905–914, 1991.

[69] O. Azzaroni. Polymer brushes here, there, and everywhere: Recent advances in their practical applications and emerging opportunities in multiple research fields. *Journal of Polymer Science Part A: Polymer Chemistry*, 50(16):3225–3258, 2012.

[70] W. Yang and F. Zhou. Polymer brushes for antibiofouling and lubrication. *Biosurface and Biotribology*, 3(3):97–114, 2017.

[71] C. Yoshikawa, T. Hoshiba, K. Sakakibara, and Y. Tsujii. Flocculation of cells by cellulose nanofibers modified with concentrated polymer brushes. *ACS Applied Nano Materials*, 1(4):1450–1455, 2018.

[72] J. Majoinen, A. Walther, J. R. McKee, E. Kontturi, V. Aseyev, J. M. Malho, J. Ruokolainen, and O. Ikkala. Polyelectrolyte brushes grafted from cellulose nanocrystals using cu-mediated surface-initiated controlled radical polymerization. *Biomacromolecules*, 12(8):2997–3006, 2011.

[73] S. Edmondson, V. L. Osborne, and W. T. S. Huck. Polymer brushes via surface-initiated polymerizations. *Chemical society reviews*, 33(1):14–22, 2004.

[74] M. Kim, S. K. Schmitt, J. W. Choi, J. D. Krutty, and P. Gopalan. From self-assembled monolayers to coatings: Advances in the synthesis and nanobio applications of polymer brushes. *Polymers*, 7(7):1346–1378, 2015.

[75] A. Olivier, F. Meyer, J. M. Raquez, P. Damman, and P. Dubois. Surface-initiated controlled polymerization as a convenient method for designing functional polymer brushes: From self-assembled monolayers to patterned surfaces. *Progress in polymer science*, 37(1):157–181, 2012.

[76] F. J. Xu, K. G. Neoh, and E. T. Kang. Bioactive surfaces and biomaterials via atom transfer radical polymerization. *Progress in polymer science*, 34(8):719–761, 2009.

[77] Y. Tsujii, K. Ohno, S. Yamamoto, A. Goto, and T. Fukuda. Structure and properties of high-density polymer brushes prepared by surface-initiated living radical polymerization. *Surface-initiated polymerization I*, pages 1–45, 2006.

[78] C. Tadokoro, K. Sato, T. Nagamine, K. Nakano, S. Sasaki, T. Sato, K. Sakakibara, and Y. Tsujii. Concentrated polymer brush as reciprocating seal material for low leakage and low friction. *Tribology Transactions*, 63(1):20–27, 2020.

[79] D. Dukes, Y. Li, S. Lewis, B. Benicewicz, L. Schadler, and S. K. Kumar. Conformational transitions of spherical polymer brushes: synthesis, characterization, and theory. *Macromolecules*, 43(3):1564–1570, 2010.

[80] R. Barbey, L. Lavanant, D. Paripovic, N. Schuwer, C. Sugnaux, S. Tugulu, and H. A. Klok. Polymer brushes via surface-initiated controlled radical polymerization: synthesis, characterization, properties, and applications. *Chemical reviews*, 109(11):5437–5527, 2009.

[81] C. Hui, J. Pietrasik, M. Schmitt, C. Mahoney, J. Choi, M. R. Bockstaller, and K. Matyjaszewski. Surface-initiated polymerization as an enabling tool for multifunctional (nano-) engineered hybrid materials. *Chemistry of Materials*, 26(1):745–762, 2014.

[82] X. Huang and M. J. Wirth. Surface-initiated radical polymerization on porous silica. *Analytical chemistry*, 69(22):4577–4580, 1997.

[83] K. Matyjaszewski and N. V. Tsarevsky. Macromolecular engineering by atom transfer radical polymerization. *Journal of the American Chemical Society*, 136(18):6513–6533, 2014.

[84] S. Yamamoto, M. Ejaz, Y. Tsujii, and T. Fukuda. Surface interaction forces of well-defined, high-density polymer brushes studied by atomic force microscopy. 2. effect of graft density. *Macromolecules*, 33(15):5608–5612, 2000.

[85] S. Yamamoto, M. Ejaz, Y. Tsujii, M. Matsumoto, and T. Fukuda. Surface interaction forces of well-defined, high-density polymer brushes studied by atomic force microscopy. 1. effect of chain length. *macromolecules*, 33(15):5602–5607, 2000.

[86] K. Binder and A. Milchev. Polymer brushes on flat and curved surfaces: How computer simulations can help to test theories and to interpret experiments. *Journal of Polymer Science Part B: Polymer Physics*, 50(22):1515–1555, 2012.

[87] L. C. H. Moh, M. D. Losego, and P. V. Braun. Solvent quality effects on scaling behavior of poly (methyl methacrylate) brushes in the moderate-and high-density regimes. *Langmuir*, 27(7):3698–3702, 2011.

[88] E. B. Zhulina, O. V. Borisov, V. A. Pryamitsyn, and T. M. Birshtein. Coil-globule type transitions in polymers. 1. collapse of layers of grafted polymer chains. *Macromolecules*, 24(1):140–149, 1991.

[89] A. Nomura, K. Okayasu, K. Ohno, T. Fukuda, and Y. Tsujii. Lubrication mechanism of concentrated polymer brushes in solvents: effect of solvent quality and thereby swelling state. *Macromolecules*, 44(12):5013–5019, 2011.

[90] C. Yoshikawa, A. Goto, Y. Tsujii, T. Fukuda, K. Yamamoto, and A. Kishida. Fabrication of high-density polymer brush on polymer substrate by surface-initiated living radical polymerization. *Macromolecules*, 38(11):4604–4610, 2005.

[91] W. Liu, Y. Li, T. Wang, D. Li, L. Fang, S. Zhu, H. Shen, J. Zhang, H. Sun, and B. Yang. Elliptical polymer brush ring array mediated protein patterning and

cell adhesion on patterned protein surfaces. *ACS applied materials & interfaces*, 5(23):12587–12593, 2013.

[92] C. Yoshikawa, A. Goto, N. Ishizuka, K. Nakanishi, A. Kishida, Y. Tsujii, and T. Fukuda. Size-exclusion effect and protein repellency of concentrated polymer brushes prepared by surface-initiated living radical polymerization. In *Macromolecular symposia*, volume 248, pages 189–198. Wiley Online Library, 2007.

[93] P. Linse and V. Lobaskin. Electrostatic attraction and phase separation in solutions of like-charged colloidal particles. *Physical review letters*, 83(20):4208, 1999.

[94] K. C. Marshall, R. STOUT, and R. Mitchell. Mechanism of the initial events in the sorption of marine bacteria to surfaces. *Microbiology*, 68(3):337–348, 1971.

[95] H. H. M. Rijnaarts, W. Norde, J. Lyklema, and A. J. B. Zehnder. Dlvo and steric contributions to bacterial deposition in media of different ionic strengths. *Colloids and Surfaces B: Biointerfaces*, 14(1-4):179–195, 1999.

[96] M. Hermansson. The dlvo theory in microbial adhesion. *Colloids and surfaces B: Biointerfaces*, 14(1-4):105–119, 1999.

[97] A. Vilinska and K. H. Rao. Surface thermodynamics and extended dlvo theory of leptospirillum ferrooxidans cells' adhesion on sulfide minerals. *Mining, Metallurgy & Exploration*, 28(3):151–158, 2011.

Chapter 2

Flocculation of Cells with Cellulose Nanofibers Surface-Modified with Concentrated Polymer Brushes: Effect of Surface Charge

2.1 Chapter Introduction

When designing and developing biomaterials for tissue engineering and regenerative medicine, it is essential to consider the physical and chemical properties of the biomaterial's surface to modulate the effect on the cells. [1] In recent years, as the understanding of the extracellular matrix (ECM) has increased, more and more 3D cell culture materials have been developed. The most significant advantage of 3D cell culture over 2D culture is that it can better mimic the in vivo microenvironment, reducing the gap between in vitro culture and the biologic environment. [2] This makes it highly advantageous for drug development or cancer research, as it has been shown that results based on traditional 2D culture systems vary considerably from the reality. In order to achieve 3D culture, cell scaffolds also need to provide cells with an ECM-like surface to provide a platform for cell adsorption, value addition, and differentiation. Polymer brush grafting is an attractive means of modifying surface properties and can mimic the structure of ECM well to induce cell adsorption and growth. [3, 4] There have been reported that polymer brush-coated materials used in 3D cell culture can increase cell adsorption and influence cell growth and cell function. [5, 6]

Polymer brushes are unique structures in which one end of the polymer chain is grafted onto the surface, and the other end extends outwards due to repulsion between the graft chains. [7] Many methods such as anionic, cationic, and ring-opening polymerization have been used to graft polymer brushes, and the most widely interesting method is living radical polymerization (LRP), as this method allows precise control of many important parameters, including brush thickness, composition, and graft density. [8] Recently, it has become possible to form concentrated polymer brushes (CPB) with constant growth and ultra-high graft density on materials by applying surface-initiated LRP. [9–11] The graft density is more than an order of magnitude higher than conventional semi-dilute polymer brushes (SDPB) and CPB. In suitable solvents, the graft chains of the swollen CPB are highly stretched to almost full length. This unique polymer brush structure gives the swollen brushes unique properties such as extreme compression resistance, superlubricity, and size rejection effects. [12–14] Compared to SDPB, CPB brushes also confer a higher level of compatibility with biological materials and therefore have good prospects for application on the biological side. [11]

In past studies, PSSNa was grafted onto the surface of CNF (CNF-PSSNa) by atom transfer radical polymerization (SI-ATRP, an LRP method), which can flocculate with HepG2 cells and can enhance cell function. [15] This flocculation phenomenon with CNF-PSSNa concentration is relatively consistent with that described by the classic Derjaguin-Landau-Verwey-Overbeek (DLVO) theory when we consider cells and CNF-PSSNa as colloidal particles and absorbent polymers, respectively. [16] According to DLVO theory, the flocculation of colloidal particles and absorbent polymers is caused by a balance of van der Waals and electrostatic forces, so the importance of investigating the relationship between surface charge and flocculation behavior cannot be overstated. However, the CNF-PSSNa surface charge variation was not addressed in the study here. It is, therefore, necessary to introduce different surface charges on the CNF surface to demonstrate the variation with cellular flocculation.

In this study, four charged polymers were introduced on the CNF surface using SI-ATRP. In addition to PSSNa (containing anionic sulfonic acid), Poly (acrylic acid) (PAA) (containing anionic carboxylic acid), poly(2-(dimethylamino) ethyl methacrylate) (PDMAEMA) (containing cations primary amine salt), and Poly([(2-methacryloyloxy) ethyl]trimethylammonium chloride)(PDMTAC) (containing cationic quaternary ammonium salt) were used. [17–19] All are commonly used polymers for biomaterials with the same main chain portion and have been used in antibacterial or cell culture applications. It is worth noting that the carboxylic acid group of PAA is challenging to synthesize via ATRP as it reacts with the catalyst of ATRP. Therefore, we adopted a synthetic route by first synthesizing poly (*tert*-butyl acrylate) (P*t*BA) and then converting P*t*BA to PAA by hydrolysis. [18]

This is the first paper to discuss the flocculation of cells and CNF-CPB using DLVO theory. Herein, CPBs with different charges and potentials were grafted on the CNF surface (CNF-CPBs), and the DLVO theory was used to explain the flocculation of these CNF-CPBs with cells(Figure 2.1). Since cells are not colloidal particles, cationic CNF-CPBs lead to cell death duo to cytotoxicity. [20] For anionic CNF-CPBs, CNF-PSSNa with a smaller zeta-potential can form larger flocs and has better gene expression than PAA with a larger zeta-potential. The results demonstrated that appropriate electrostatic interactions are essential for floc formation and improved cell function. This finding is helpful for the development of CNF-CPB in regenerative medicine scaffolds and drug discovery studies.

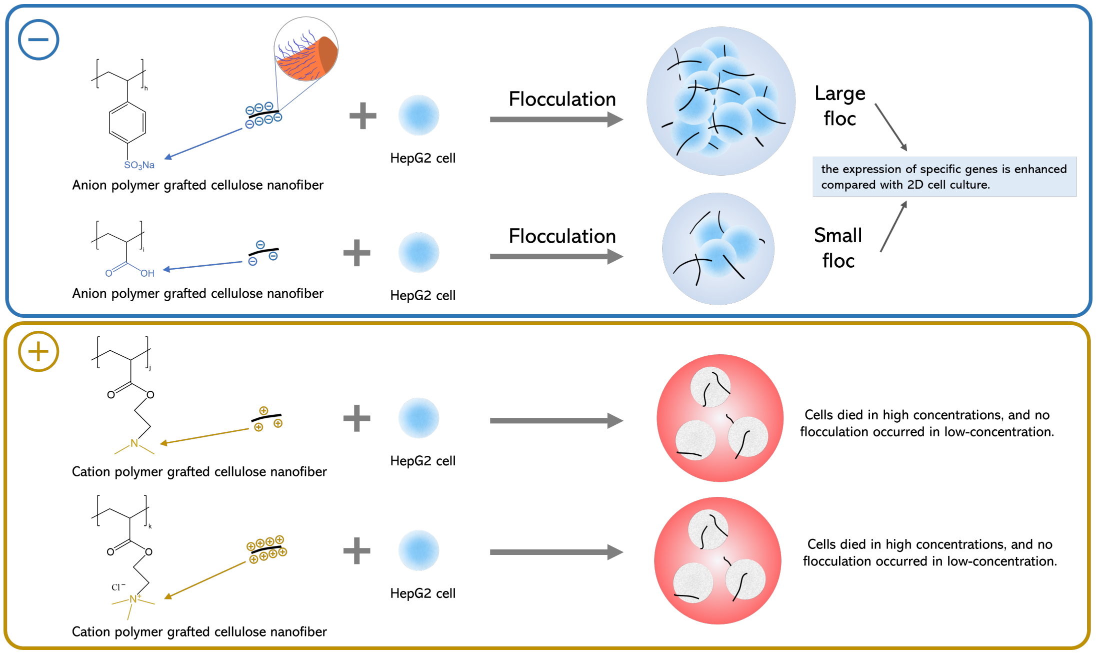

Figure 2.1: Cellar flocculation using CNF-CPBs with different surface charge.

2.2 Materials and methods

2.2.1 Materials

2-Bromoisobutyryl bromide (BiBB, 97%) was bought from Alfa Aesar, Co., Inc., Ward Hill, United States. anhydrous pyridine, N-methylpyrrolidone (NMP), toluene, CuBr (99.99%), CuBr2 (99.99%), *tert*-Butyl acrylate (*t*BA, wako), anisole, Pentamethyldiethylenetriamine (PMDETA), 2-(Dimethylamino) ethyl methacrylate (DMAEMA), DMF super dehydrated and sodium dodecyl sulfate (SDS) were purchased from Wako Pure Chemicals, Osaka, Japan. *p*-Styrenesulfonic acid sodium salt(SSNa, 99.9%), poly(ethylene glycol) methyl ether 2-bromoisobutyrate (PEGBr, Sigma Aldrich), 1,1,4,7,10,10-Hexamethyltriethylenetetramine (HMTETA, 97%), and [2-(methacryloyloxy) ethyl] trim- ethyl ammonium chloride (MTAC, 75 wt%) were obtained from Sigma-Aldrich, Missouri, United States. 2,2'-bipyridine (bpy, 99.9%) was purchased from Nacalai Tesque, INC., Kyoto, Japan. Ethyl 2-Bromoisobutyrate(EBIB) and Trifluoroethanol (TFE) were bought from TCI, Kyoto ,Japan. Dichloromethane and Trifluoroacetic acid (TFA) were obtained from KISHIDA CHEMICAL Co., Ltd., Japan. All the chemicals above were directly used without further purification.

2.2.2 Synthesis of CNF-Br

CNF-Br was prepared according to a previous study. [15] To begin this process, the water in CNF suspension (2 g dry mass; 12.3 mmol per anhydroglucose unit) was successively displaced to acetone via repeated centrifugation. For further dehydration, the precipitate was then resuspended into an NMP-toluene solution (400 ml/200 ml) and distilled for 5 h at 160 °C where the anhydrous CNF slurry in NMP was yielded. Subsequently, Anhydrous pyridine (11.9 mL, 148 mmol) and BiBB (9.16 mL, 74.1 mmol) were added at 0 °C and stirred at room temperature. Finally, the initiator-modified CNF (CNF-Br) suspended in methanol was obtained via four times methanol wash by centrifugation at 9,000 rpm for 15 min.

2.2.3 SI-ATRP of SSNa

SI-ATRP of SSNa from CNF-Br was carried out according to our previous report. [15] Briefly, A methanol (2.5 mL) solution of CuBr (1.5 mM), $CuBr_2$ (0.65 mM), and 2,2-bipyridine (5.0 mM) were prepared in a glove box purged with N_2 gas (UNIlab, MBRAUN GmbH, Germany). It was then transferred to the mixture of miliQ water (7.5 ml), SSNa (0.44 M), PEGBr (1.7 mM), and CNF-Br (20 mg), which was purged with N_2 gas. The polymerization solution was allowed to perform at 30 °C for 5h. The ^{1}H Nuclear magnetic resonance (^{1}H NMR) was carried out with a ESC-400 spectrometer (JEOL, Tokyo, Japan) in D_2O to determine the conversion. The number-average molecular weight (M_n) and polydispersity index (M_w/M_n) were determined using PSSNa-calibrated gel permeation chromatography (GPC) system, which was performed with Shodex GPC-101 (Tokyo) equipped with two Shodex gel columns SB-804HQ (Tokyo). LiCl (10 mM) in acetonitrile/water (4/6, v/v) was used as eluent, with 0.8 mL/min flow rate (40 °C). PSSNa standards were used as the reference. The grafting density (σ, chains/nm^2) of PSSNa estimation by sulfur content analyzed using Elemental analyses (EA) at the Microanalytical Laboratory of the Institute for Chemical Research, Kyoto University, as mentioned in our previous report. [15]

2.2.4 SI-ATRP of *t*BA

The mixture of *t*BA (3.63 M), EBIB (18.0 mM), PMDETA (18.2 mM), and CNF-Br (5 mg) in anisole (2.0 g) was deoxygenated by bubbling with N_2 for 10 min. The mixture was transferred to a Schlenk tube containing CuBr (18.2 m) under an N_2-purged glove box. The polymerization was allowed in an oil bath at 90 °C for 20 min. When the reaction was finished, an aliquot of the polymer solution was diluted with Tetrahydrofuran (THF) and passed through a column filled with alumina to remove the copper-ligand complex. The resulting aliquot of mixture was diluted with THF and analyzed by GPC, which was performed by Shodex GPC-101 equipped with Shodex KF-804L column. THF was used as eluent, with 0.8 mL/min flow rate (40 °C) to investigate M_n and M_w/M_n. The polystryrene (PS, PstQuick, TOSOH)) standards were used as reference. The conversion rate was determined by ^{1}H NMR analysis. To determine the σ of PtBA, the known amount of PtBA and CNF-Br were mixed and subjected to measure FT-IR. The calibration graph was prepared by the integrated ratio of carbonyl group peak (1740 cm^{-1}) of CNF-Br and the increasing of carbonyl group peak after adding PtBA. The graft amount of PtBA was estimated by using calibration graph.

2.2.5 Hydrolysis of PtBA to Poly(acrylic acid) (PAA)

Free polymer (PtBA, 0.1 g) was then dissolved in CH_2Cl_2 (10 ml) followed by cooling down in an ice bath for 20 mins. After that, TFA (4 ml) was added, and the reaction was carried out at 25 °C under stirring for 24 h. After the reaction, the free PAA was vacuum dried and subjected to GPC. CNF-PtBA was hydrolyzed to CNF-PAA using the similar condition. The obtained CNF-PAA was washed with miliQ water and stored until use.

2.2.6 SI-ATRP of DEMEMA

The DMF solution (3 mL) of CuBr (18.9 mM), CuBr2 (8.1 mM), and HMTETA (27.0 mM) were prepared under N_2-purged glove box. It was then transferred to the mixture of DMAEMA (2.7 M), EBIB (13.2 mM), and CNF-Br (10 mg), which was purged with N_2 gas for 5 min. The SI-ATRP of DEMEMA was allowed in a water bath at 30 °C for 45 min. The polymer solution was also purified with an alumina column. After that, the purified solution was diluted with DMF and then subjected to GPC using a HLC-8220 instrument (TOSOH Corporation, Tokyo, Japan) with a Shodex LF-804 column (40 °C) and 10 mM LiCl in DMF as the eluent with a flow rate of 0.8 mL/min. The poly(methyl methacrylate) (PMMA) standards were used as reference to determine M_n and M_w/M_n. The ^{1}H NMR was used to investigate the conversion rate. The nitrogen content measured by EA was used to estimate σ.

2.2.7 SI-ATRP of MTAC

To a Schlenk tube equipped with a magnetic stirring bar was added the mixture of MTAC (1.19 M), EBIB (7.0 mM), water (1.6 g), and CNF-Br (40 mg). The mixture was deoxygenated under N_2 gas for 10 min. The copper-ligand complex of CuBr (15.9 mM) and bpy (31.8 mM) in TFE (11.1 g) was prepared under N_2-regulated glove box. The solution of the copper-ligand complex was then transferred to the mixture in that of Schlenk tube. The polymerization has proceeded at 30 °C for 30 min. The polyethyene glycol (PEG)-calibrated GPC system of free solution of PMTAC was performed to determine M_n and M_w/M_n, and the conversion rate was determined by ^{1}H NMR analysis. Briefly, GPC was performed with Shodex GPC-101 equipped with two Shodex gel columns SB-804HQ using acetonitrile/water (1/1, v/v) contained 0.5 M acetic acid and 0.2 M $NaNO_3$ as fluent and used PEG (TSK standard, TOSOH) as standards reference. As for the σ estimation was calculated by nitrogen content measured by EA.

2.2.8 Calculation of graft density

The graft density (σ, groups/nm^2) refers to the number of polymer brushes grafted on a unit surface area of CNF, which can be calculated by the following equation

$$\sigma = \frac{A \times N_A}{M_n \times S} \tag{2.1}$$

where A(g/g) is graft amount which means weights of grafted PSSNa per unit CNF, M_n is Avogadro number and S (nm^2/g) is surface area. The determination of A was calculated by FI-IR measurement or EA as mentioned. S was estimated from the diameter (20 nm) and density (1.5 g/cm^3) of the CNF.

σ describes the grafting density of the polymer on the CNF surface. And the effective graft density (σ_{eff}) was expressed as the grafted density of the peripheral outermost surface using a fully stretched core-shell model, [21] which was assumed as

$$\sigma_{eff} = \sigma \times (r_0/r) \tag{2.2}$$

r is the radius of the polymer grafted CNF and was estimated as ($r = r_0 + \mathrm{DP}{*}l$), where DP is the polymerization degree of the grafted polymer, and l is the length of per monomeric unit ($l = 0.25$ nm for SSNa, *t*BA, DMAEMA and MTAC).

Dimensionless graft density (σ^*) describing the proportion of the CNF surface area occupied by the grafted polymer is calculated based on σ and is given by the following equation

$$\sigma^* = \sigma_{eff} \times S_c \tag{2.3}$$

Here S_c is the cross-sectional area of different polymer brushes respectively, which was estimated using the length of per monomeric unit l, and the density of monomers (1 g/cm^3).

2.2.9 Cleavage of grafted polymers from CNF

The CPBs were cleaved from CNF to confirm the coincident M_n of the free polymer. The cleavage of CNF-PSSNa was detailed as an example. The CNF-PSSNa (20 mg) was dispersed in 10 ml of KOH solution (1 mol/L). The hydrolysis was performed by reflux at 95 °C for 24 h. The mixture was neutralized with HCl solution (1 mol/L) and centrifuged at 12,000 rpm for 10 min. The CNF residual was precipitated while the PSSNa part was dissolved in the aqueous phase. The PSSNa solution was purified by dialysis against water (MWCO = 3.5 kD, Spectra Pore® 3) and subjected to lyophilization. M_n of cleaved CPBs was determined by GPC.

2.2.10 Zeta-potential measurement

The zeta potential was determined on Zeta-potential & Particle size Analyzer ELSZ-1000 (Otsuka Electronics Co., Ltd., Japan) for 0.5 wt% CNF-CPBs suspension in PBS. The CNF-CPBs were washed with PBS for 5 times and further redispersed in PBS to reach the concentration of 0.5 wt%. Their zeta potential was investigated using zeta flow cells (Otsuka Electronics Co., Ltd.). In addition, the zeta potential of CNF-CPBs after protein adsorption was also investigated. The CNF-CPBs (10 mg) were suspended in 10 mL of medium containing 10% fetal bovine serum (FBS, Sigma-Aldrich Co. LLC, St. Louis, United States) and incubated at 37 °C for 1 h. The CNF-CPBs were collected by centrifugation (12000 rpm, 10 min), washed with PBS 5 times to remove unabsorbed protein. Subsequently, redispersed with PBS at 0.5 wt% zeta-potential analysis was carried out. All measurements were performed in triplicate.

2.2.11 Protein adsorption test

CNF-CPBs were suspended at 0.5 wt% in 1 ml of low glucose Dulbecco's modified Eagle's medium (DMEM, Thermo Fisher Scientific, Inc., Massachusetts, United States), containing 10% FBS. After incubation at 37 °C for 1 h, the CNF-CPBs were collected and washed with PBS several times to remove unbound proteins. To recover adsorbed proteins, the CNF-CPBs were then placed in 1 ml of 5% SDS, vortexed and sonicated several times. The supernatants were collected and subjected to determine the protein concentrations with BCA assay kit using an albumin BSA standard curve according to the manufacturer's instruction (Thermo Fisher Scientific). The absorbance of the BCA solutions was then measured at 570 nm using a microplate reader (Infinite M Nano+, Tecan Japan Co., Ltd., Kawasaki, Japan). The adsorption test was triplicated for average.

2.2.12 Cell cultures

Human hepatocellular carcinoma cells (HepG2) (Cellular Engineering Technologies Inc., Iowa, United States) were cultured in DMEM containing 10% (v/v) fetal bovine serum (FBS) and 1% (v/v) penicillin/streptomycin (Thermo Fisher Scientific) at 37 °C in a humidified incubator with 5% CO_2.

2.2.13 Cell culture with CNF-CPBs

Cells were gently added in DMEM containing 10% FBS with CNF-CPBs in different concentrations (0.005, 0.05, and 0.1 wt%), respectively. Cells density was adjusted to 1×10^5 cells/mL. The mixtures were then seeded on 24-well plates (Greiner Bio-One, North Carolina, United States) with 1 mL per well. The medium was changed every 2-3 days.

2.2.14 Confocal laser microscope observation

After incubation, the flocs (aggregation of cells and CNF-CPBs) were gently washed with PBS, and 4% paraformaldehyde in PBS was added to fix for 30 min at 25 °C. After removing the solution and washed with PBS, 0.1% Triton X-100 in PBS was carefully added to permeabilized cells. Again washed with PBS after 15 mins, and 1% bovine serum albumin (BSA) in PBS was used to incubate with flocs for 30 min. The flocs were then incubated in the solution of Alexa Fluor 555-conjugated phalloidin (Invitrogen, California, United States) and DAPI at 4 °C, overnight to visualize F-actin and nuclei, respectively. Flocs were washed with PBS, mounted on a slide glass with SlowFade™ Diamond Antifade Mountant (Invitrogen), and observed cell aggregation by a confocal laser microscope (TCS SP5, LEICA Microsystems GmbH, Germany).

2.2.15 Quantitative real-time polymerase chain reaction (RT-qPCR)

albumin (ALB) and hepatocyte nuclear factor 4α (HNF4A), were selected for analysis. After 7 days of incubation, The RNA was extracted and purified using Qiagen RNeasy Mini kit (QIAGEN) according to the manufacturer's protocol. In brief, the flocs were collected and washed with PBS. The RNeasy Lysis Buffer was applied for the lysis of cells before RNA isolation. The samples were kept at -80 °C until use. Then the samples were crushed by a electric tissue grinde with a 1.5ml pestle (Mini Cordless Grinder, Funakoshi Co. Ltd., Tokyo, Japan). After centrifugation, the homogenized lysate was collected, 70% ethanol was added, and mixed well by pipetting. The samples were subsequently passed through RNeasy spin column. The total RNA binded into the column. The RNA was purified by washing with Buffer RW1 and Buffer RPE, respectively. The extracted RNA was eluted from the column by RNase-free water. The RNA concentration was measured by a NanoDrop 2000 spectrophotometer (Thermo Scientific), and 15 ng of extracted RNA was subsequently reacted with PrimeScript RT reagent kit (TAKARA) at 37 °C for 15 min and 85 °C for 5 sec to synthesize the cDNA by reverse transcription. The expression levels of target genes and housekeeping genes were conducted using LightCycler® 480 SYBR Green I Master (Roche, Germany). The primers used for qPCR are listed in Table 2.1. The reaction mixture of 2x Master mix (7.5 μL), forward and reverse primers (0.15 μL, 50 μM stock), cDNA (5.0 μL), and DEPC water (2.2 μL) was then performed on LightCycler480. Expression of the target genes was normalized to that of the housekeeping gene, glyceraldehyde-3-phosphate dehydrogenase (GAPDH).

Table 2.1: Primers used in RT-qPCR analysis.

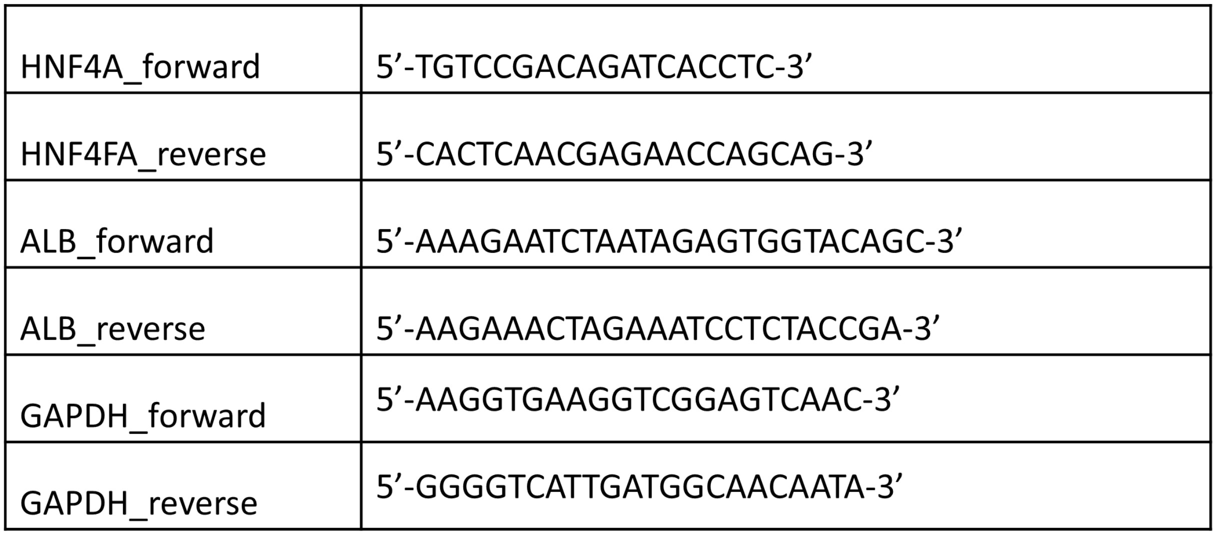

HNF4A_forward	5’-TGTCCGACAGATCACCTC-3’
HNF4FA_reverse	5’-CACTCAACGAGAACCAGCAG-3’
ALB_forward	5’-AAAGAATCTAATAGAGTGGTACAGC-3’
ALB_reverse	5’-AAGAAACTAGAAATCCTCTACCGA-3’
GAPDH_forward	5’-AAGGTGAAGGTCGGAGTCAAC-3’
GAPDH_reverse	5’-GGGGTCATTGATGGCAACAATA-3’

2.2.16 Live/dead assay

After removing the medium, The mixture of cells and CNF-CPBs cultured for 7 days were washed with PBS, and 500 μL of the staining solution was then added directly to culture wells. To produce the staining solution, calceinAM (20 μL, Dojindo Molecular Technologies, Maryland, United States) and ethidium homodimer-1 (20 μL, FUJIFILM Wako Pure Chemical Co., Ltd., Osaka, Japan) was added into PBS (10 mL). Fluorescence images were obtained under a fluorescent microscope (BZ-X800, Keyence Co., Ltd., Osaka, Japan) after 30 min of incubation.

2.2.17 Statistical Analysis

All data are expressed as mean ± standard deviation (SD). To compare data among more than 3 groups, a two-way ANOVA with Tukey’s test was used. Differences with less than 0.05 P values were considered statistically significant.

2.3 Results and Discussion

2.3.1 Preparation of CNF-CPBs

The synthesis of CNF-CPBs was carried out in two steps, as shown in Figur 2.2A. First, the initiation site for polymerization was introduced, and then the charged polymers (PSSNa, P*t*BA, PDMAEMA and PMTAC) were grafted from CNF-Br by SI-ATRP (Figure 2.2B).

First, ATRP conditions were optimized under homogeneous condition using EBIB instead of CNF-Br. Figures 2.3-2.6 show first-order kinetic plot and M_n and M_w/M_n vs conversion for the polymerization of SSNa, *t*BA, DMAEMA and MTAC. For the polymerization of SSNa [15] (Figure 2.3), the first-order plot was almost linear, indicating that the radical concentration was constant throughout the examined polymerization time. However, the plot did not cross the origin. This was probably because the polymerization started before heating at 30 °C. M_ns were almost equal to the theoretical value. M_w/M_n (PDI) was relatively low (∼1.3) (Figure 2.3). Furthermore, as shown in Figure 2.4, the first-order plot of the polymerization of *t*BA [18] tended to be linear for the first 20 mins, after which it rapidly plateaus, indicating that the free radicals were rapidly deactivated after 20 mins. The M_ns was lower than the theoretical value line, reasonably because PS was used as standards for the calibration curve of the GPC measurements. PDI was between 1.1 and 1.4. As for PDMAEMA [22] (Figure 2.5), the first-order curve was almost linear and the radical concentration remains essentially constant. M_ns started to show a large deviation after conversion equals 10%, which may due to different polymer (PMMA) was used to make the standard curve. PDI increases with conversion and stabilizes after conversion above 20% in a narrow range (∼1.27). Moreover, for the polymerization of MTAC (Figure 2.6), the first-order plot passes through the origin and was relatively linear. This indicates that the reaction was stable in terms of radical concentration within the experimental time. It is worth mentioning that the standard for PMTAC were also different polymer (PEG). the PDI was relatively narrow (1.3∼1.4).

These results indicate that a controlled polymerization reaction occurs under the given conditions. After examining the solution polymerization, the subsequent SI-ATRP was carried out under the condition that conversion=20% for all monomers.

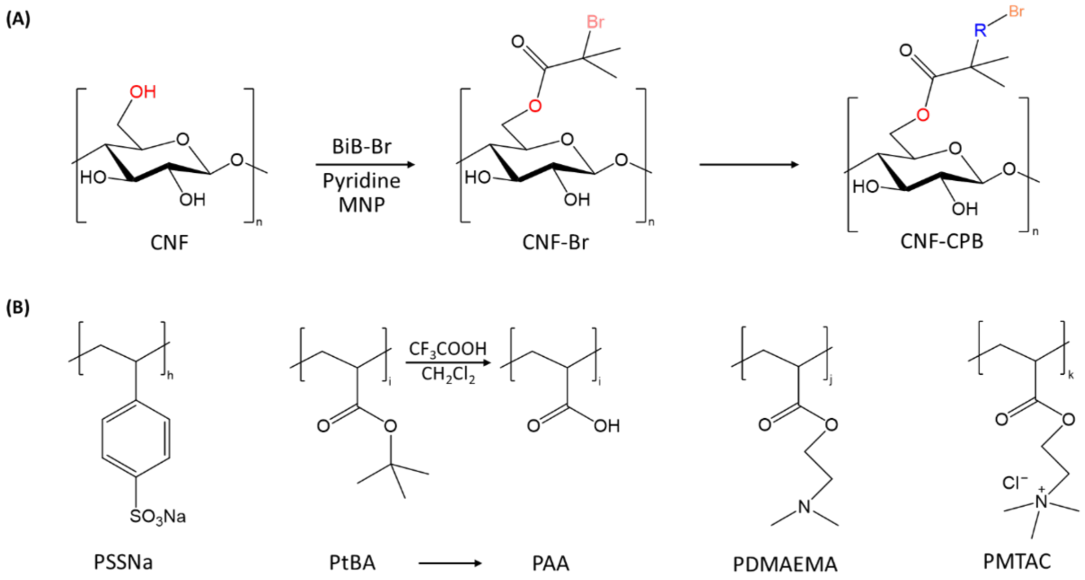

Figure 2.2: Scheme of SI-ATRP, (A) Synthesis steps of CNF-CPBs. (B) Chemical formula represented by R group in different CNF-CPBs.

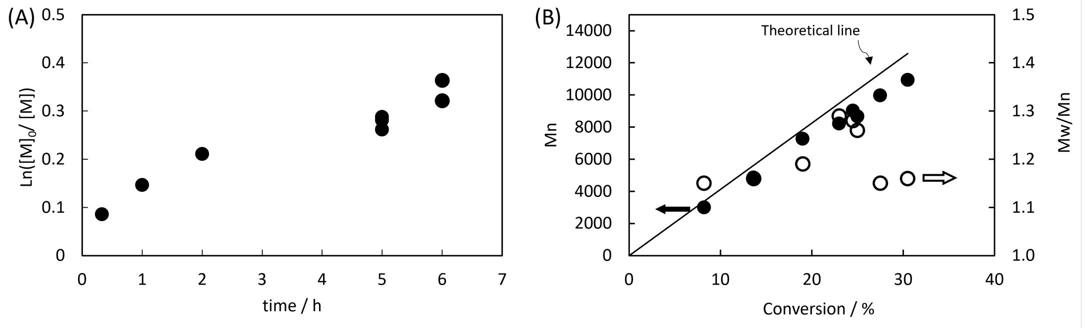

Figure 2.3: Plot of (A) ln([M]$_0$/[M]) vs time and (B) M_n, M_w/M_n vs conversion of ATRP SSNa at 30 °C. [PEGBr]/[SSNa]/[Cu(I)Br]/[Cu(II)Br]/[bpy] = 1/200/0.7/0.3/2.

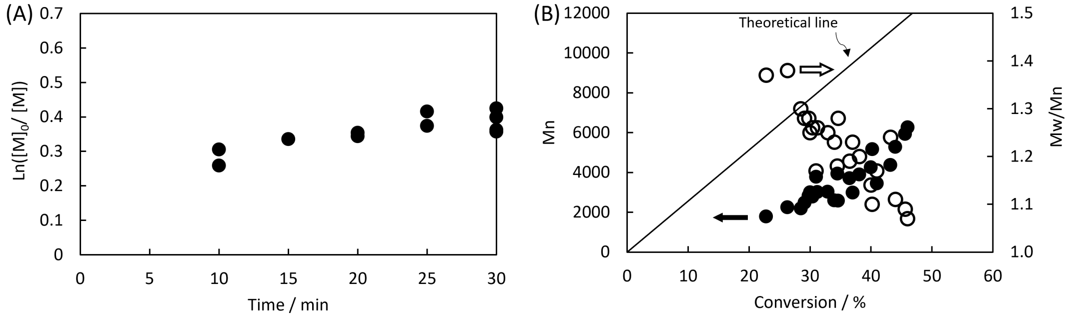

Figure 2.4: Plot of (A) ln([M]$_0$/[M]) vs time and (B) M_n, M_w/M_n vs conversion of ATRP of *t*BA at 90 °C. [EBIB]/[*t*BA]/[Cu(I)Br]/[PMDETA] = 1/200/1/1.

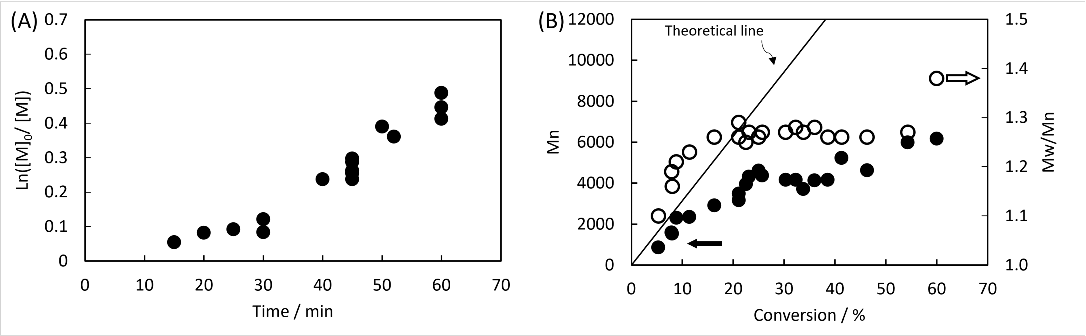

Figure 2.5: Plot of (A) ln([M]$_0$/[M]) vs time and (B) M_n, M_w/M_n vs conversion of ATRP of DMAEMA at 30 °C. [EBIB]/[DMAEMA]/[Cu(I)Br]/[Cu(II)Br]/[HMTETA] = 1/200/1.4/0.6/2.

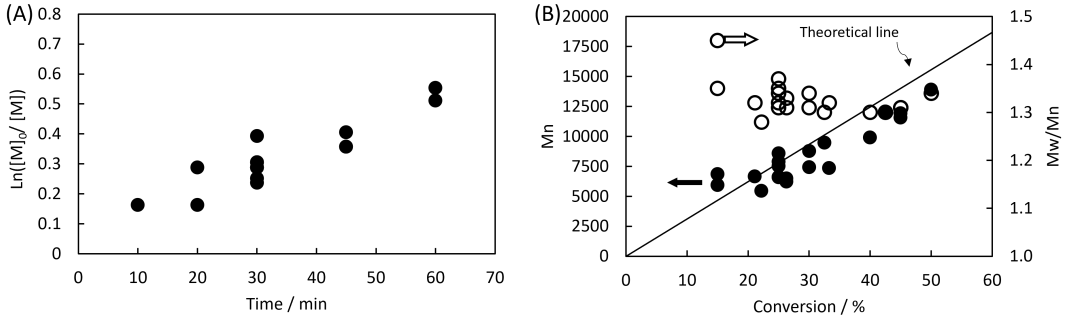

Figure 2.6: Plot of (A) ln([M]$_0$/[M]) vs time and (B) M_n, M_w/M_n vs conversion of ATRP of MTAC at 30 °C. [EBIB]/[MTAC]/[Cu(I)Br]/[bpy] = 1/150/2/4. The solid line represents the calculated values.

Based on the results of ATRP, four charged polymers were grafted onto CNF by SI-ATRP. The results are summarized in Table 2.2 The table displays the M_n and PDI of the free polymer. It is known that free polymer is a good indicator for M_n and PDI of grafted polymer.

Therefore, we cut out the graft polymer from CNF via alkaline hydrolysis and confirmed the molecular weight by GPC measurement. Figure 2.7 shows the GPC traces. The side chains of PMATC and PDEMAMA are also cleaved by hydrolysis, as shown in Figure 2.7, so the molecular weight changes. Therefore, the free polymers were also hydrolyzed, and GPC measurement was performed. For each type of polymer, the results were almost the same for the grafted polymer and its free polymer, which means that the graft chain and the free chain grew in the same activation and inactivation frequencies, therefor the free polymer value could be used for the indicator of the grafted polymer. [23] The graft amounts of SSNa, PMTAC, and PDMAEMA were determined by elemental analysis. The graft amount of tBA was calculated from FT-IR measurements since there is no specific element that can be used for calculation. σ was determined from the graft amount, $M_{n,theo}$, and surface area as show in Equation (2.1). The effective graft density of the outermost surface of the CNF-CPB is estimated from the core-shell model as in Equation (2.2), based on the fact that for CPB the grafted polymer is highly stretched to show more than 80% of the full length. [10] Dimensionless graft density (σ^*) on the surface of CNF-CPBs was estimated base on σ_{eff} and the cross-sectional area as show in Equation (2.3). According to the definition of CPB graft density ($\sigma^* > 0.1$), each brush can be categorized into CPB. [10] The results are in accordance with the previous report. [15]

Table 2.2: Characteristic of CNF-CPBs.

CNF-CPBs	E.A.					M_n (g/mol)	$M_{n,the}$[a]	M_w/M_n	DP[b]	σ (chain/nm^2)	σ_{eff}[e] (chain/nm^2)	σ*[f]
	C%	H%	Br%	S%	N%							
CNF-PSSNa	40.95	4.37	<0.1	11.33	0.39	1.0×10^4	1.1×10^4	1.2	55.3	1.2[c]	0.55	0.72
CNF-P*t*BA	-	-	-	-	-	4.2×10^3	8.0×10^3	1.3	62.4	0.67[d]	0.37	0.22
CNF-PDMAEMA	55.51	8.67	1.47	-	6.75	4.3×10^3	9.3×10^3	1.3	59.2	1.5[c]	0.88	0.63
CNF-PMTAC	45.27	8.38	0.91	-	5.52	6.5×10^3	1.3×10^4	1.3	62.6	1.6[c]	0.91	0.88

[a]Theoretical molecular weight calculated by the equation, $M_{n,the}$= [monomer]$_0$/([free indicator]$_0$ + [CNF-Br]$_0$) × conversion × molecular weight of monomer. [b]Degree of polymerization. [c]Grafting density of CNF-CPBs were estimated by elemental analysis (EA). [d]Grafting density of CNF-CPBs estimated by FT-IR measurement. [e]effective graft density (σ_{eff}). [f]Dimensionless graft density (σ*).

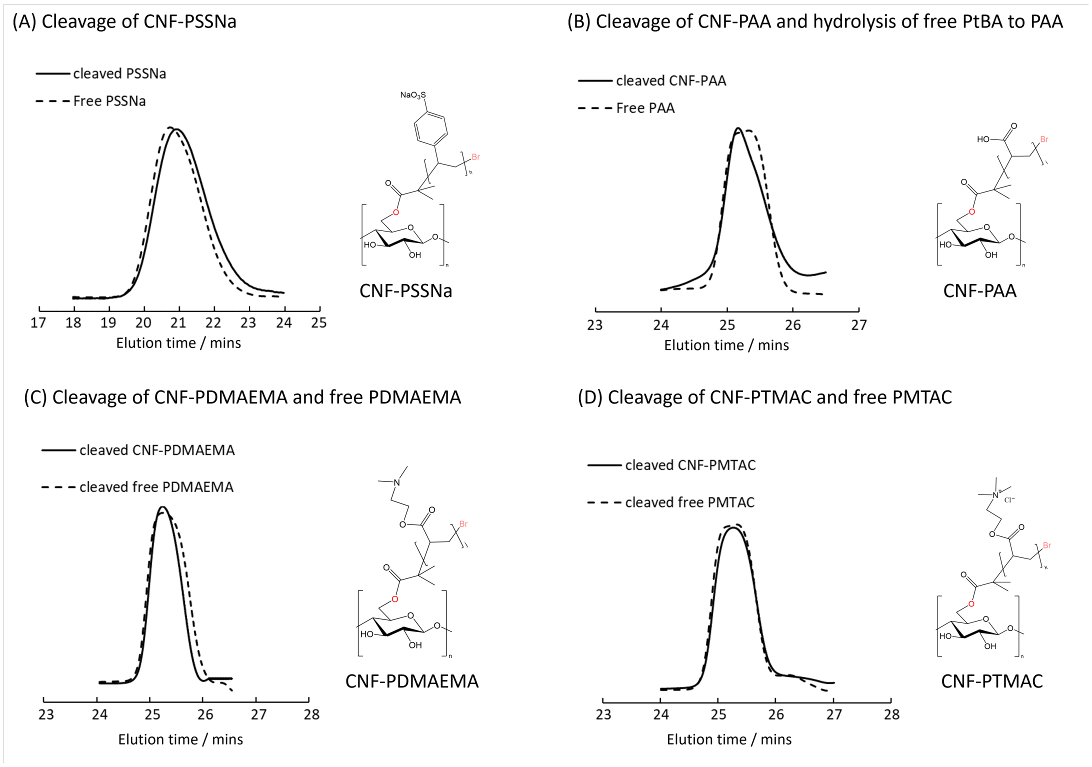

Figure 2.7: GPC charts of free and cleaved polymer (A) CNF-PSSNa, (B) CNF-PAA, (C) CNF-PMTAC and (D) CNF-PDMAEMA. The solid red lines in chemical structures represent the cleaved site.

To obtain CNF-PAA, CNF-P*t*BA was hydrolyzed. The FT-IR chart of CNF-Br, CNF-P*t*BA and CNF-PAA was shown in Figure 2.8. The peak at 1580 cm^{-1} (as indicated by the arrow) which derived from the *tert*-butyl group was significantly reduced after hydrolyzed reaction. It should be noted that FT-IR results didn't provide a quantitative indication of hydrolytic conversions.

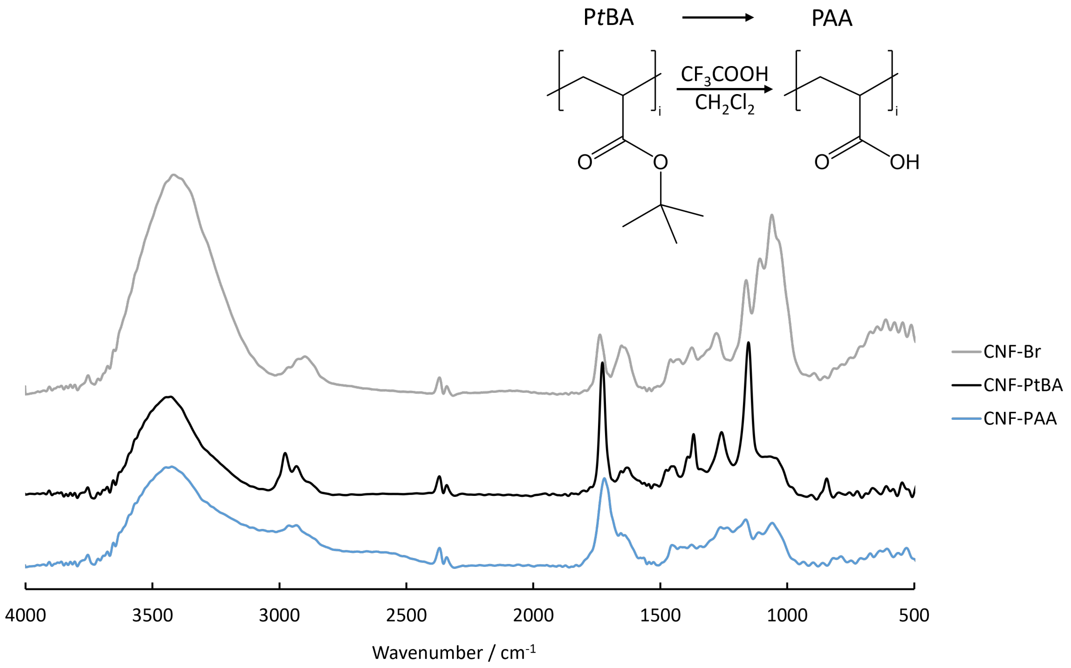

Figure 2.8: FT-IR spectra of CNF-Br, CNF-P*t*BA and CNF-PAA.

2.3.2 Protein adsorption

Cell attachment usually starts with the adsorption of non-specific proteins. [24] Therefore, protein adsorption determination of the material is essential. Protein adsorption of CNF-CPBs was determined using fetal bovine serum (FBS) as the protein source, as it is usually added to the cell culture medium.

The Figure 2.9 shows that CNF-PSSNa and CNF-PMTAC, possessed significant protein adsorption capacity. In contrast, PDMAEMA and PAA had almost no protein adsorption. In general, it is known that electrostatic forces are the primary driver of protein adsorption, especially for proteins with opposite charges. [25] Therefore, the reason of difference in protein adsorption may be caused by the fact that CNF-CPBs have different electrical charges may be attributed to different charges.

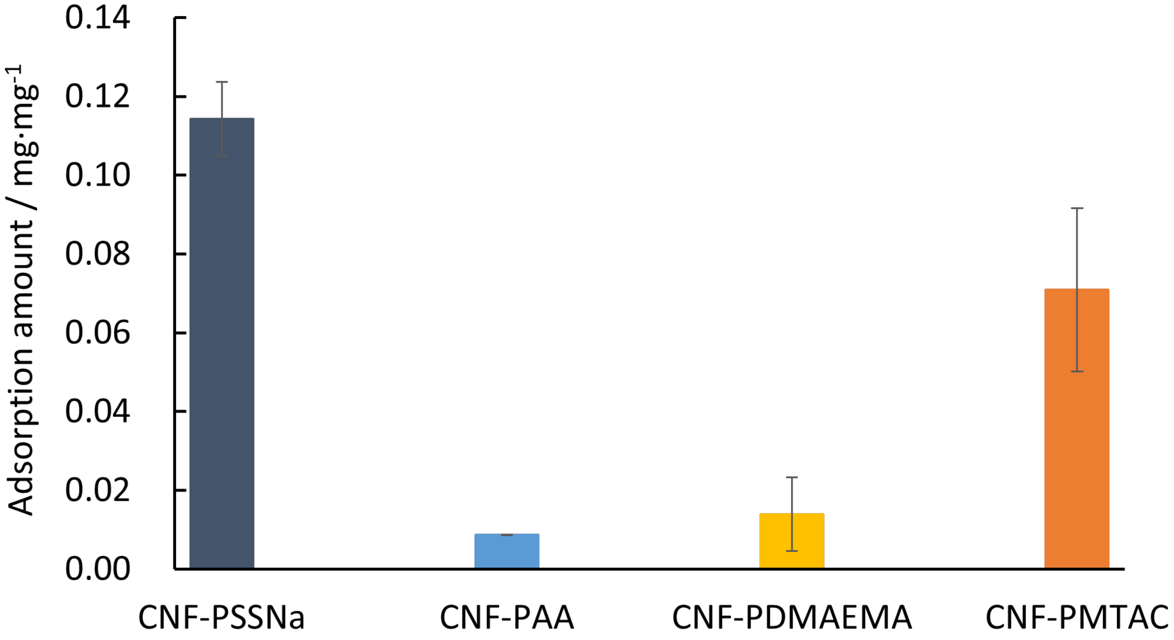

Figure 2.9: Protein adsorption on CNF-CPBs.

2.3.3 Zeta potential

Zeta potential measurements were taken to characterize the surface charging of CNF-CPBs in PBS buffer and summarized in Table 2.3. For pristine CNF-CPBs, the CNF-PSSNa and CNF-PAA surfaces are negatively charged, while CNF-PDMAEMA and CNF-PMTAC are positively charged.

For anionic CNF-CPBs, CNF-PSSNa has a higher surface potential and higher protein absorption amount. This trend was similar in cationic CNF-CPBs, where CNF-PMTAC with higher surface potential also adsorbed more protein relative to CNF-PDMAEMA. The results are consistent with our previous observations that electrostatic forces can drive protein adsorption and that protein adsorption increases when the charge increases. [25] Afterwards, CNF-CPBs were subjected to zeta-potential measurements after protein adsorption. Interestingly, the anionic CNF-CPBs remained negatively charged after protein adsorption. Among them, the CNF-PSSNa potential decreased substantially, while the CNF-PAA remained almost unchanged. The cationic CNF-CPBs remained positively charged. Among them, the potential of CNF-PMTAC is substantially reduced, while CNF-PDMAEMA is only slightly reduced.

The change in surface charge (decrease in zeta potential) of the anionic and cationic CNF-PSSNa and CNF-PMTAC after protein adsorption is evident from the charged properties of the attracted proteins. It has to be mentioned that the mechanism of protein adsorption is still a complex issue. In addition to electrostatic gravitational forces, space forces, hydrogen bonding and protein structure should be considered, all of which lead to the adsorption of electrically repulsive proteins on the surface. [26] This explains the fact that CNF-PMTAC adsorbs more proteins than CNF-PDMAEMA, but with little change in surface charge. Nevertheless, experiments demonstrate that electrostatic gravity still dominates the adsorption kinetics.

Table 2.3: The Zeta-potential of CNF-CPBs with and without protein adsorption in PBS.

CNF-CPBs type	Zeta potential in PBS (mV)			
	Non-adsorption	SD	FBS adsorption	SD
CNF-PSSNa	-22.98	1.22	-6.64	1.64
CNF-PAA	-18.92	0.39	-19.85	1.14
CNF-PDMAEMA	11.08	0.77	3.84	2.64
CNF-PMTAC	17.13	0.63	12.13	1.64
PBS	-1.49			0.56

2.3.4 Flocculation of HepG2 cells with CNF-CPBs

HepG2 cells were cultured with CNF-CPBs to verify the effect of different surface charges on the cellar flocculation phenomenon. HepG2 cells without CNF-CPBs were used as controls. Furthermore, to observe the effect of different concentrations, three different concentrations of 0.1%, 0.05%, and 0.005% of CNF-CPBs were used for this study. After incubation, the results are shown in Fgiure 2.10, the phase-contrast micrographs of different CNF-CPBs cultured with cells for 1, 4, 7 and 14 days. Cell flocculation (floc) can be observed in most samples from the fourth day of culture onwards. While no floc was observed in the control group and samples in 0.005% of CNF-PDMAEMA and CNF-PMTAC. In order to further discuss the relationship between the charge of CNF-CPBs and cell flocculation, the floc sizes were measured.

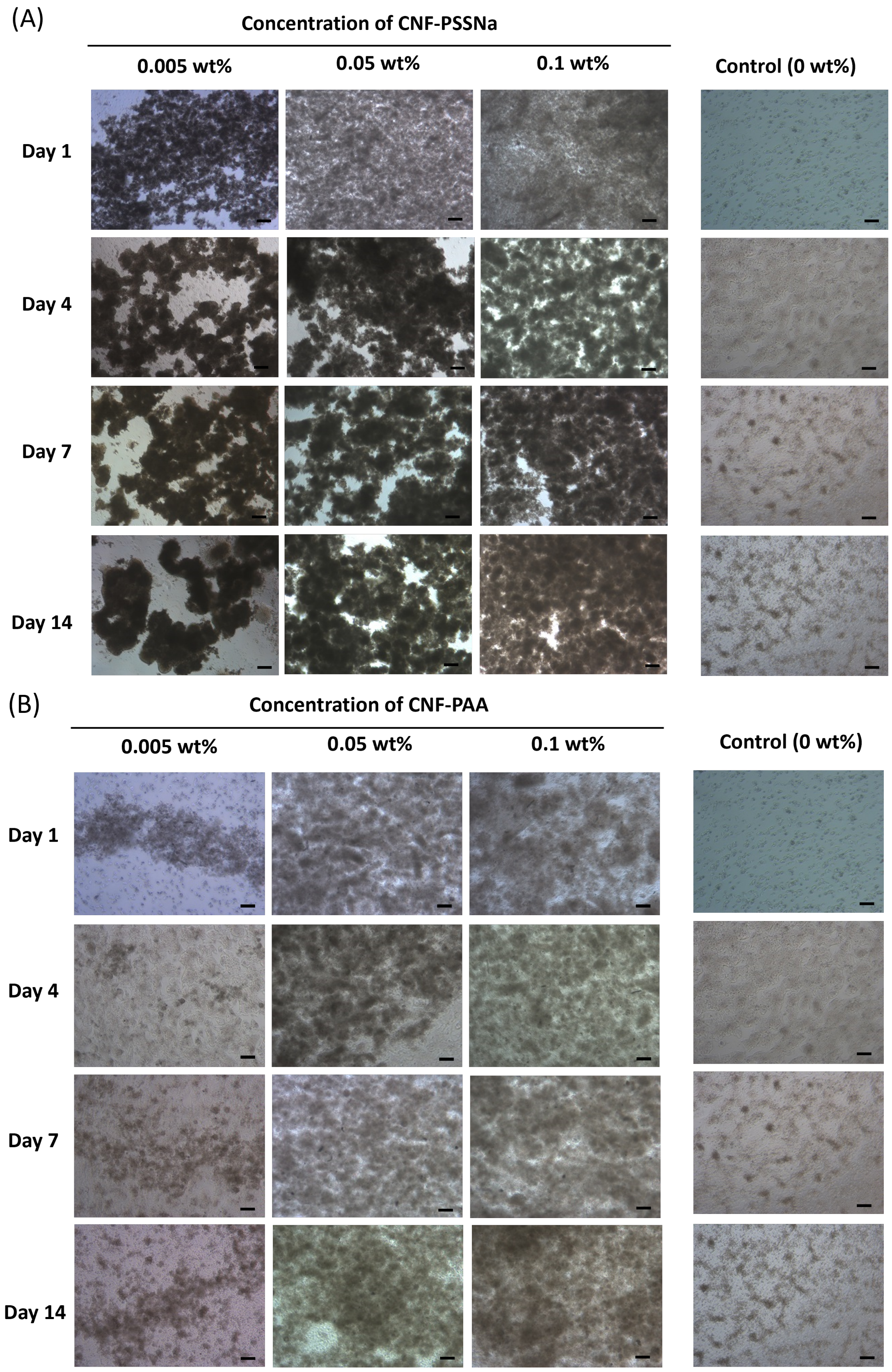
(A)
Concentration of CNF-PSSNa
0.005 wt%
0.05 wt%
0.1 wt%
Control (0 wt%)
Day 1
Day 4
Day 7
Day 14
(B)
Concentration of CNF-PAA
0.005 wt%
0.05 wt%
0.1 wt%
Control (0 wt%)
Day 1
Day 4
Day 7
Day 14

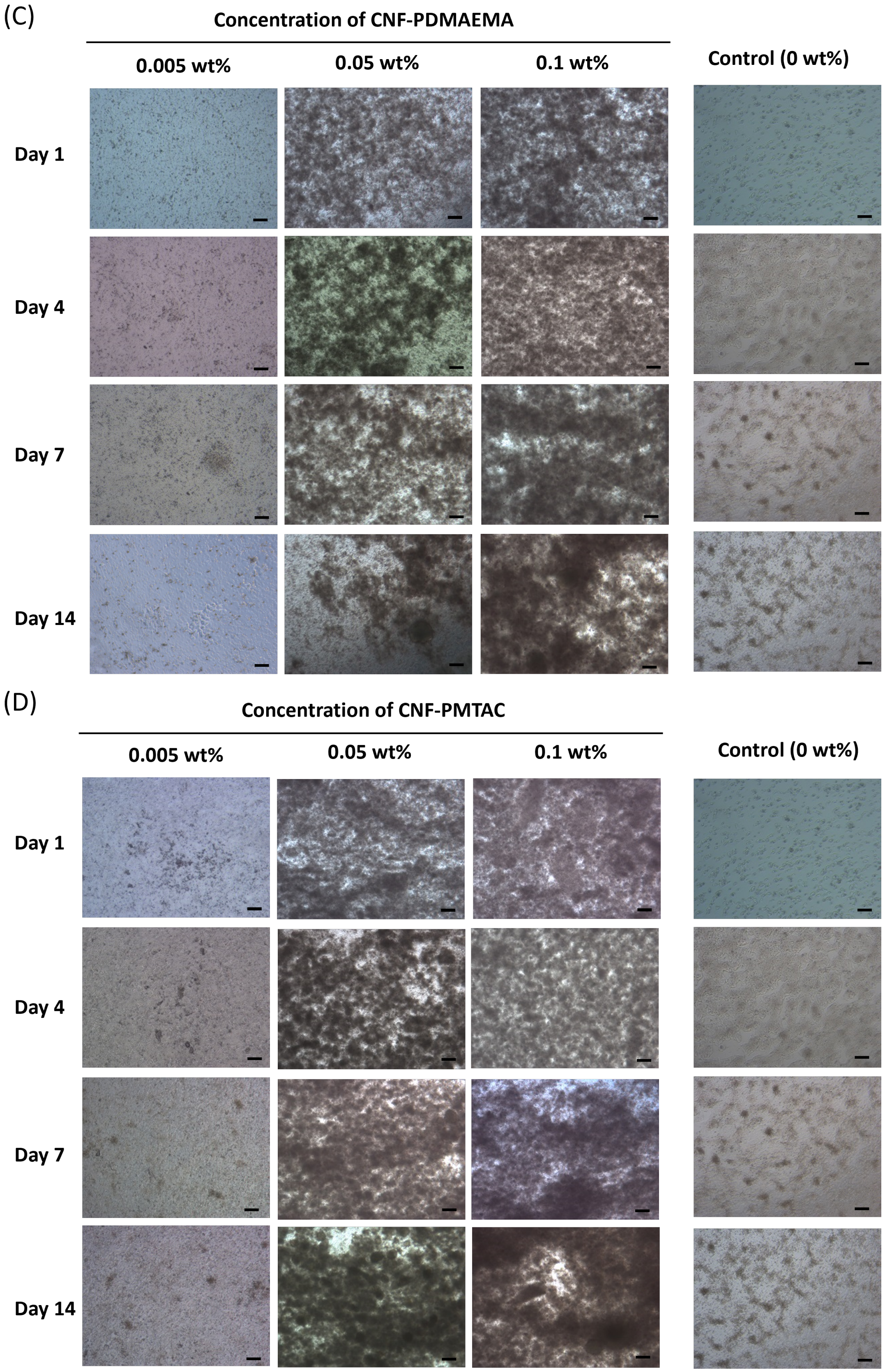

Figure 2.10: Phase-contrast micrograms of the flocs of HepG2 and CNF-CPBs cultured for 1, 4, 7 and 14 days. $[\text{HepG2}]_0 = 5 \times 10^5$ and CNF-CPBs = 0.005, 0.05 and 0.1 wt%. Scale bar = 200 μm. (A) CNF-PSSNa, (B) CNF-PAA, (C) CNF-PDMAEMA and (D) CNF-MTAC.

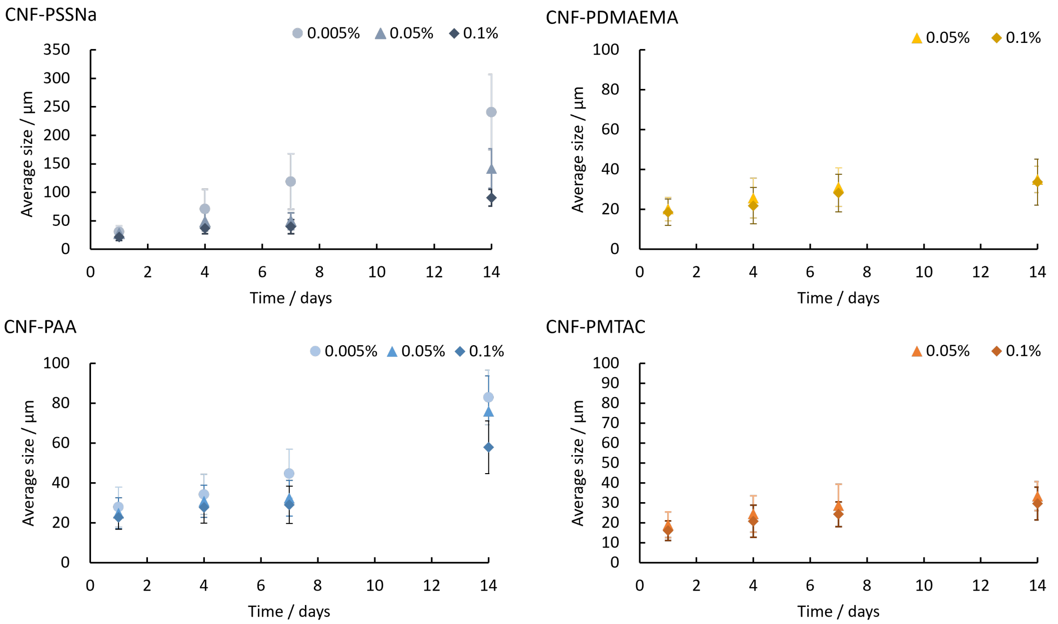

Figure 2.11: Floc size of cells after co-culturing with CNF-CPBs as a function of cultured time.

The size of flocs obtained with increasing incubation time were shown in Figure 2.11. For cationic CNF-CPBs, the cells formed smaller flocs than with the anionic polymers. And, at a low concentration of 0.005%, the cells did not flocculate. In addition to this, cationic polymers do not increase the size of flocs, rather become constant. The cells may die in the floc. Hence live/dead staining is used to verify whether the cells are alive or dead.

Therefore, Live/dead assay was used to analyze 0.1% and 0.05% samples of CNF-PDMAEMA and CNF-PMTAC. A commonly used Live/dead assay method was used in which live cells were stained by calcein-AM to green fluorescence, and dead cells were stained by ethidium homodimer-1 to red fluorescence. As shown in Figure 2.12, almost no green fluorescence was observed for all control samples (CNF-PDMAEMA and CNF-PMTAC). The results confirmed that, as we suspected, the survival of the cells is meager due to the cytotoxicity of the poly-positive macromolecules. [27]

For anionic CNF-CPBs, the flocs formed with cell flocculation all increase with incubation time. However, the flocs of CNF-PAA were significantly smaller. Apparently, it is necessary to optimize the surface charge in order to create large flocs. Herein we focused on the flocculation phenomenon of CNF-PSSNa and CNF-PAA, attempting to explain the flocculation of CNF-CPBs with cells using the DLVO theory. Admittedly, the adsorption of cells is a complex phenomenon, and therefore it is incredibly challenging to provide a complete theoretical explanation. However, the DLVO theory has been used to explain the adsorption of bacteria and was first reported in 1971. [28] According to this theory, we treat the cell as a colloidal particle, and its flocculation behavior with adsorbent polymers can be explained by the balance between van der Waals (vdW) and electrostatic forces. The adsorbent polymers, in this case, are CNF-PSSNa and CNF-PAA.

For the same CNF-CPBs, more CNF-CPBs were wrapped around the cells in the higher concentration samples, and electrostatic repulsion between the CNF-CPBs resulted in smaller flocs. This is consistent with the above experimental results that the floc size in the presence of high concentrations of CNF-CPBs is smaller than that of low concentrations. Furthermore, when we compared CNF-PSSNa and CNF-PAA, CNF-PAA had a higher surface charge and higher electrostatic repulsion relative to CNF-PSSNa. These electrostatic repulsions make it more difficult to form larger flocs due to the greater distance between CNF-PAA coated cells. The results also confirmed that the flocs formed under the same conditions were larger than CNF-PAA in the presence of CNF-PSSNa. Based on these results, we found that the DLVO theory can be used to explain the flocculation of anionic CNF-CPBs with cells. It implies that other cell lines may also exhibit the same flocculation phenomenon as CNF-CPBs.

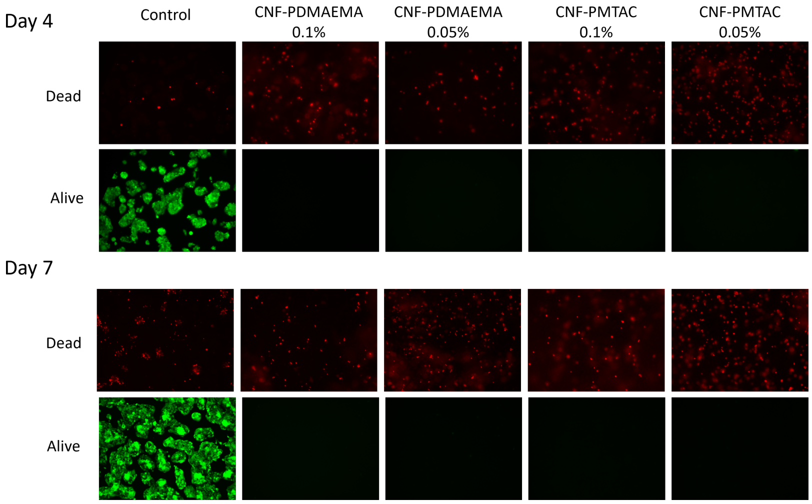

Figure 2.12: Live/dead assay of HepG2 cells co-cultured with CNF-PDMAEMA and CNF-PMTAC for 7 days in concentration of 0.1% and 0.05%, Green fluorescence indicates calceinAM stain in the live cells and red fluorescence indicates the ethidium homodimer-1 stain in the dead cells.HepG2 = 1.0×10^5 cells/mL.

2.3.5 Confocal laser microscopy observation

Although flocs of different sizes were obtained, the distribution of cells in the flocs still needs to be verified. Three-dimensional confocal imaging was used to determine the location of the floc cells.

Figure 2.13 shows the results after 7 days of culture, For PSSNa and PAA, the cells are present in a uniformly dispersed manner within the flock. As for the cationic polymers, the cells were present in the flock, however, the number was much smaller than the anionic CNF-CPBs. This is due to the fact that the cells were dead.

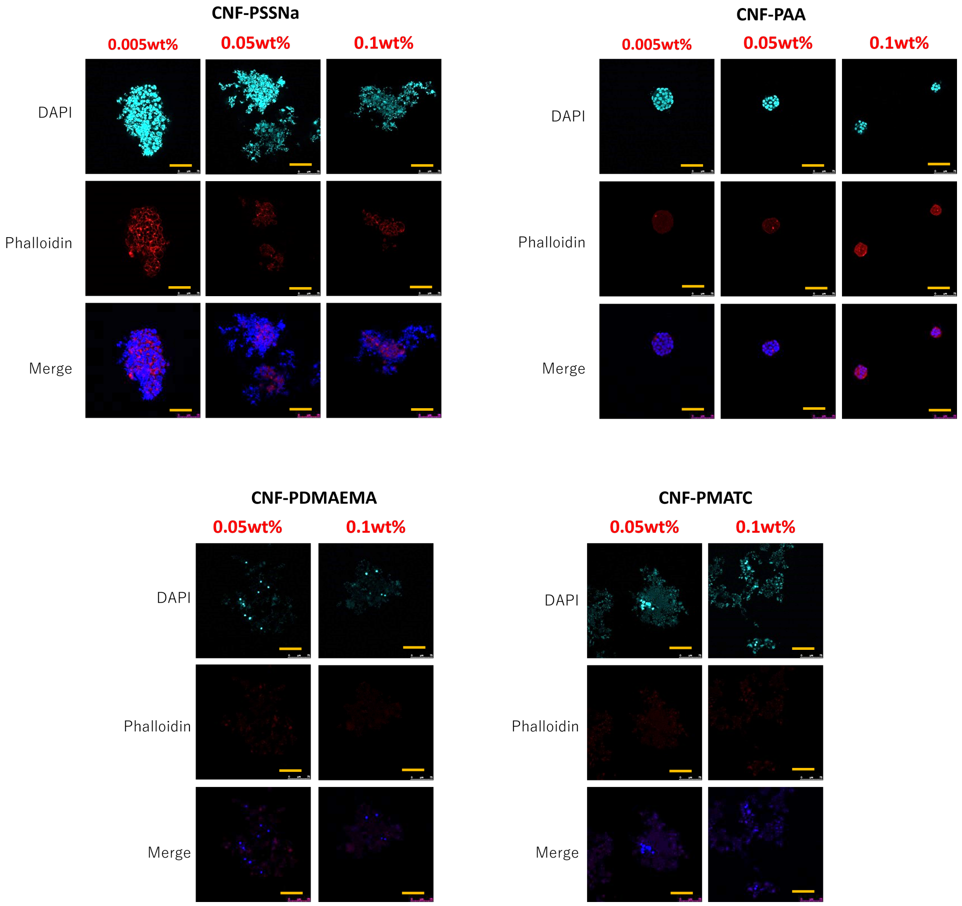

Figure 2.13: Confocal laser microscopy images of the HepG2 cells and positively charged CNF-CPBs (in 0.1%, 0.05% and 0.005%) flocs cultured for 7 days. Nuclei were counterstained with DAPI (blue), and F-actin was stained with phalloidin (red). HepG2 = 1.0 × 10^5 cells/mL; Scale bar=75 μm.

2.3.6 RT-qPCR

In order to further evaluate the effect of the CNF-CPBs culture system on cell function, RT-PCR analysis was performed on HepG2 after co-culture with CNF-CPBs. Two liver specific genes were selected for characterization because HepG2 is a liver-derived cell: albumin (ALB), which is commonly used to evaluate the protein-secreting function of the liver, and hepatocyte nuclear factor 4α (HNF4A), which has a broad impact on the regulation of liver-specific genes. [29, 30]

PCR was not performed on the floc of the cationic CNF-CPBs group because the RNA was rapidly broken back down within a few hours after cell death. [31] The gene expression of ALB and HNF4A in HepG2 after co-cultured with CNF-PSSNa and CNF-PAA for 7 day is shown in Figure 2.14. An interesting phenomenon was observed for anionic CNF-CPBs. For CNF-PSSNa, gene expression and floc size increased at decreasing concentrations, which is reasonable because in the 3D cell culture system, gene expression generally increase when the spheres size increase. [32] CNF-PAA, on the other hand, demonstrates the opposite result. Floc size increases at lower concentrations, however gene expression decreases. This may be due to other factors such as surface microstructure. Furthermore, for both genes, the experimental group (HepG2 cells co-cultured with CNF-CPBs with an anionic surface) did not grow significantly relative to the control group. Appropriate extension of the culture time may allow for more pronounced gene expression differences relative to the control (2D culture). [33]

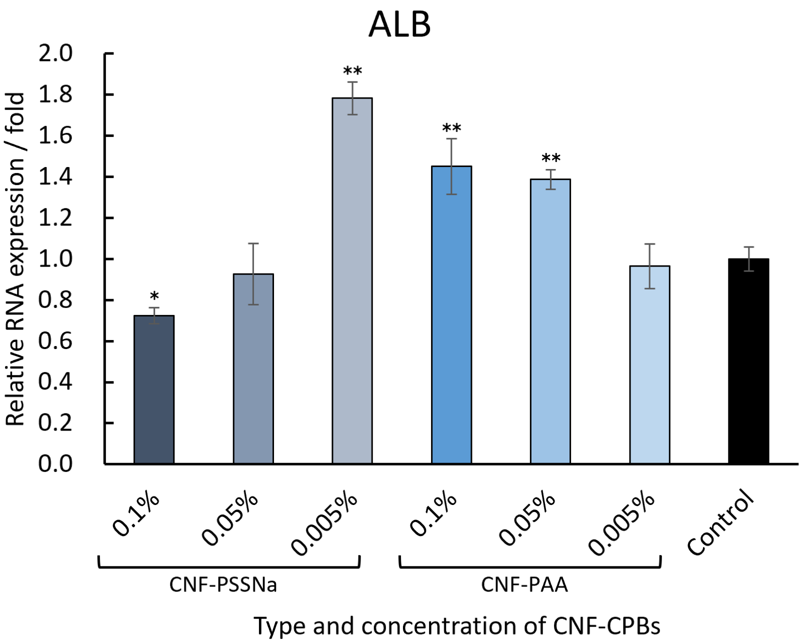

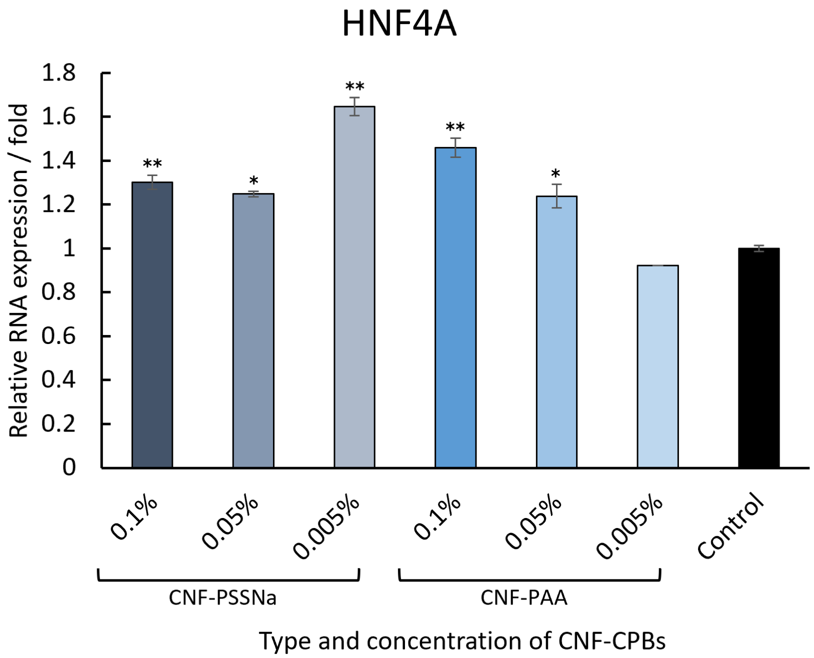

Figure 2.14: Relative RNA expression of HepG2 cells co-cultured with CNF-CPBs for 7 days, normalized with control. The significances, calculated against the control, are marked as *: $p < 0.05$, **: $p < 0.01$. HepG2 = 1.0×10^5 cells/mL.

Based on the above studies, the results of HepG2 cells co-cultured with CNF-CPBs for 7 days are summarized in Table 2.4. All cells of the cationicCNF-CPBs died due to cytotoxicity and no gene expression was observed. In CNF-PSSNa and CNF-PAA, CNF-PSSNa had a greater range of floc sizes, reaching a maximum at 7 days of culture. Likewise, the maximal values of specific gene expression were higher. In order to improve floc size and cell function, it is important to have an appropriate surface charge according to DLVO theory. Therefore CNF-PSSNa is even more valuable for further research.

Table 2.4: Summary of CNF-CPBs properties.

CNF-CPBs type	Protein adsorption[a]	Floc size[b] (μm)	Gene expression[c]	
			ALB	HNF4A
CNF-PSSNa	++++	39.7 - 118.1	0.72 – 1.8	1.2 – 1.6
CNF-PAA	+	29.1 – 44.8	1.0 – 1.5	0.9 – 1.5
CNF-PDMAEMA	++	28.2 – 31.2	Cells were dead	
CNF-PMTAC	+++	24.3 – 28.7		

[a] The number of " + " presents the protein absorption capacity, while " ++++ " means strongest the protein adsorption capacity. [b] The floc size range of cells and CNF-CPBs for different concentration cultured for 7 days. [c] Relative RNA expression range for different concentration after 7 days culture(normalized with control).

2.4 Conclusions

In this chapter, four CNF-CPBs with different anionic or cationic polymers on their surfaces respectively were used in culture with cells, and they exhibited different cell flocculation phenomena explained by the DLVO theory.

The zeta potential shown a decisive influence on protein adsorption and subsequent cell flocculation. When comparing different charges, the cationic CNF-CPBs proved to be cytotoxic, leading to cell death. In anionic CNF-CPBs, the size of flocculation is influenced by the concentration of CNF-CPBs as well as the zeta potential. When the concentration of CNF-CPBs is decreased, the size of flocs increased. On the other hand, CNF-PSSNa with a lower value of zeta potential after adsorption of proteins induces larger flocs. Also, anionic CNF-CPBs formed flocs with cells that increased the expression of liver-specific genes and were most highly expressed when forming larger flocs with CNF-PSSNa. In conclusion, the comparison between the anionic strong electrolyte PSSNa and the weak electrolyte PAA is an essential issue in this chapter, and the significant differences in size and function of the flocs obtained prove that the surface potential is highly influential, which is consistent with the description of the DLVO theory. This is highly beneficial for the future exploration of CNF-CPBs based tissue engineering and drug development.

Reference

[1] Todorka G Vladkova. Surface engineered polymeric biomaterials with improved biocontact properties. *International Journal of polymer science*, 2010, 2010.

[2] M. Vinci, S. Gowan, F. Boxall, L. Patterson, M. Zimmermann, W. Court, C. Lomas, M. Mendiola, D. Hardisson, and S. A. Eccles. Advances in establishment and analysis of three-dimensional tumor spheroid-based functional assays for target validation and drug evaluation. *BMC biology*, 10(1):1–21, 2012.

[3] W. Yang and F. Zhou. Polymer brushes for antibiofouling and lubrication. *Biosurface and Biotribology*, 3(3):97–114, 2017.

[4] L. Moroni, M. K. Gunnewiek, and E. M. Benetti. Polymer brush coatings regulating cell behavior: Passive interfaces turn into active. *Acta biomaterialia*, 10(6):2367–2378, 2014.

[5] M. K. Gunnewiek, A. Di Luca, H. Z. Bollemaat, C. A. van Blitterswijk, G. J. Vancso, L. Moroni, and E. M. Benetti. Creeping proteins in microporous structures: Polymer brush-assisted fabrication of 3d gradients for tissue engineering. *Advanced healthcare materials*, 4(8):1169–1174, 2015.

[6] T. A. Petrie, J. E. Raynor, D. W. Dumbauld, T. T. Lee, S. Jagtap, K. L. Templeman, D. M. Collard, and A. J. García. Multivalent integrin-specific ligands enhance tissue healing and biomaterial integration. *Science translational medicine*, 2(45):45ra60–45ra60, 2010.

[7] B. Zhao and W. J. Brittain. Polymer brushes: surface-immobilized macromolecules. *Progress in Polymer Science*, 25(5):677–710, 2000.

[8] Y. Tsujii, K. Ohno, S. Yamamoto, A. Goto, and T. Fukuda. Structure and properties of high-density polymer brushes prepared by surface-initiated living radical polymerization. *Surface-initiated polymerization I*, pages 1–45, 2006.

[9] S. Yamamoto, M. Ejaz, Y. Tsujii, M. Matsumoto, and T. Fukuda. Surface interaction forces of well-defined, high-density polymer brushes studied by atomic force microscopy. 1. effect of chain length. *macromolecules*, 33(15):5602–5607, 2000.

[10] S. Yamamoto, M. Ejaz, Y. Tsujii, and T. Fukuda. Surface interaction forces of well-defined, high-density polymer brushes studied by atomic force microscopy. 2. effect of graft density. *Macromolecules*, 33(15):5608–5612, 2000.

[11] C. Yoshikawa, A. Goto, Y. Tsujii, T. Fukuda, K. Yamamoto, and A. Kishida. Fabrication of high-density polymer brush on polymer substrate by surface-initiated living radical polymerization. *Macromolecules*, 38(11):4604–4610, 2005.

[12] A. Nomura, K. Okayasu, K. Ohno, T. Fukuda, and Y. Tsujii. Lubrication mechanism of concentrated polymer brushes in solvents: effect of solvent quality and thereby swelling state. *Macromolecules*, 44(12):5013–5019, 2011.

[13] D. Parisi, Y. Ruan, G. Ochbaum, K. S. Silmore, L. L. Cullari, C. Y. Liu, R. Bitton, O. Regev, J. W. Swan, B. Loppinet, and D. Vlassopoulos. Short and soft: Multidomain organization, tunable dynamics, and jamming in suspensions of grafted colloidal cylinders with a small aspect ratio. *Langmuir*, 35(52):17103–17113, 2019.

[14] C. Yoshikawa, A. Goto, N. Ishizuka, K. Nakanishi, A. Kishida, Y. Tsujii, and T. Fukuda. Size-exclusion effect and protein repellency of concentrated polymer brushes prepared by surface-initiated living radical polymerization. In *Macromolecular symposia*, volume 248, pages 189–198. Wiley Online Library, 2007.

[15] C. Yoshikawa, T. Hoshiba, K. Sakakibara, and Y. Tsujii. Flocculation of cells by cellulose nanofibers modified with concentrated polymer brushes. *ACS Applied Nano Materials*, 1(4):1450–1455, 2018.

[16] T. Ndikubwimana, X. Zeng, N. He, Z. Xiao, Y. Xie, J. S. Chang, L. Lin, and Y. Lu. Microalgae biomass harvesting by bioflocculation-interpretation by classical dlvo theory. *Biochemical Engineering Journal*, 101:160–167, 2015.

[17] M. Rahmati, E. A. Silva, J. E. Reseland, C. A. Heyward, and H. J. Haugen. Biological responses to physicochemical properties of biomaterial surface. *Chemical Society Reviews*, 49(15):5178–5224, 2020.

[18] T. Wu, P. Gong, I. Szleifer, P. Vlcˇek, V. Šubr, and J. Genzer. Behavior of surface-anchored poly (acrylic acid) brushes with grafting density gradients on solid substrates: 1. experiment. *Macromolecules*, 40(24):8756–8764, 2007.

[19] E. Koufakis, T. Manouras, S. H. Anastasiadis, and M. Vamvakaki. Film properties and antimicrobial efficacy of quaternized pdmaema brushes: Short vs long alkyl chain length. *Langmuir*, 36(13):3482–3493, 2020.

[20] K. Kim, W. C. Chen, Y. Heo, and Y. Wang. Polycations and their biomedical applications. *Progress in Polymer Science*, 60, 2016.

[21] K. Ohno, T. Morinaga, S. Takeno, Y. Tsujii, and T. Fukuda. Suspensions of silica particles grafted with concentrated polymer brush: Effects of graft chain length on brush layer thickness and colloidal crystallization. *Macromolecules*, 40(25):9143–9150, 2007.

[22] S. B. Lee, A. J. Russell, and K. Matyjaszewski. Atrp synthesis of amphiphilic random, gradient, and block copolymers of 2-(dimethylamino) ethyl methacrylate and n-butyl methacrylate in aqueous media. *Biomacromolecules*, 4(5):1386–1393, 2003.

[23] S. Y. Hsu, Y. Kayama, K. Ohno, K. Sakakibara, T. Fukuda, and Y Tsujii. Controlled synthesis of concentrated polymer brushes with ultralarge thickness by surface-initiated atom transfer radical polymerization under high pressure. *Macromolecules*, 53(1):132–137, 2019.

[24] N. Nath, J. Hyun, H. Ma, and A. Chilkoti. Surface engineering strategies for control of protein and cell interactions. *Surface science*, 570(1-2):98–110, 2004.

[25] T. Hoshiba, C. Yoshikawa, and K. Sakakibara. Characterization of initial cell adhesion on charged polymer substrates in serum-containing and serum-free media. *Langmuir*, 34(13):4043–4051, 2018.

[26] J. Lin, H. Chang, W. Kao, K. Lin, H. Liao, Y. You, Y. Kuo, D. Kuo, K. Chu, Y. Chu, and J. Shyue. Effect of surface potential on extracellular matrix protein adsorption. *Langmuir*, 30(34):10328–10335, 2014.

[27] D. Fischer, Y. Li, B. Ahlemeyer, J. Krieglstein, and T. Kissel. In vitro cytotoxicity testing of polycations: influence of polymer structure on cell viability and hemolysis. *Biomaterials*, 24(7):1121–1131, 2003.

[28] K. C. Marshall, R. STOUT, and R. Mitchell. Mechanism of the initial events in the sorption of marine bacteria to surfaces. *Microbiology*, 68(3):337–348, 1971.

[29] K. M. Kulig and J. P. Vacanti. Hepatic tissue engineering. *Transplant Immunology*, 12(3-4):303–310, 2004.

[30] C. A. Wiwi and D. J. Waxman. Mini reviewrole of hepatocyte nuclear factors in growth hormone-regulated, sexually dimorphic expression of liver cytochromes p450. *Growth factors*, 22(2):79–88, 2004.

[31] I. Noguchi, H. Arai, and R. Iizuka. A study on postmortem stability of vasopressin messenger rna in rat brain compared with those in total rna and ribosomal rna. *Journal of Neural Transmission/General Section JNT*, 83(3):171–178, 1991.

[32] S. C. Ramaiahgari, M. W. Den Braver, B. Herpers, V. Terpstra, J. N. M. Commandeur, B. van de Water, and L. S. Price. A 3d in vitro model of differentiated hepg2 cell spheroids with improved liver-like properties for repeated dose high-throughput toxicity studies. *Archives of toxicology*, 88(5):1083–1095, 2014.

[33] H. Jeon, K. Kang, S. A. Park, W. D. Kim, S. S. Paik, J. Lee, S.and Jeong, and D. Choi. Generation of multilayered 3d structures of hepg2 cells using a bio-printing technique. *Gut and liver*, 11(1):121, 2017.

Chapter 3

Cellular flocculation using concentrated polymer brush-modified cellulose nanofibers with different fiber lengths

3.1 Chapter Introduction

Two-dimensional (2D) cell culture is widely used in medical and biological research as a powerful platform optimized for cell adsorption and growth. [1] It is a simple, fast, and cost-effective method. [2] However, in native tissues, extracellular matrix (ECM) and neighboring cells influence cell performance, and due to planar growth, limited biochemical information is provided by 2D cell cultures. [3] Recently, three-dimensional (3D) cell culture has attracted immense interest due to its similarity to tissue environment. [4] Differences between 3D and 2D cell culture have been observed in protein expression, enzyme activity, cell activity, proliferation, and toxicity. [5] Reports indicate that 3D cell culture is more conducive to drug development (Parkinson's drugs, anti-cancer drugs, etc.) and bioengineering (regenerative medicine), than 2D cell culture. [6–9]

3D cell culture is of two types depending on the physical support: scaffold-free, based on overhanging and low-attachment plates; and scaffold-dependent, based on natural and artificial synthetic scaffolds. [10] Despite extensive research, most of these technologies have limitations. Scaffold-free methods require complex operating procedures and technical optimization, while scaffold-dependent outcomes depend on material sources and processes. Previous studies report that cell proliferation, differentiation, and growth can be limited by pore size and interconnectivity. [11] With the development of drug screening and tissue engineering, more advanced 3D culture techniques need to be developed. [12–15]

The preparation of CNFs was first reported as a suspension of cellulose whiskers by sulfuric acid hydrolysis. [16] Thereafter, mechanical and/or chemical disintegration of vegetation afforded CNFs with 3–50 nm diameter and more than 500 nm length. Cellulose is one of the most abundant natural polymers on earth. [17] In recent years, owing to their biocompatibility, high surface area, and mechanical properties, plant-derived CNFs have been investigated for use in biomedical research. [18] Unlike bacterial cellulose, which is widely used in biomaterials, plant-derived CNF length can be controlled by source variation. [19, 20] This provides greater flexibility for CNF-based biomaterial development. Additionally, plant-derived CNFs have a size and structure similar to natural ECM, enabling support of cell growth. [21] ECM not only allows cell adsorption, but also provides the cells physical support, [22] triggering cell function-determining reactions, making the biomaterial nanostructure extremely important. [23] Oxidized CNF is degradable via in-vivo reactions with amino acids, indicating its potential as a degradable scaffold. [24] Therefore, plant-derived CNF could be a good 3D cell culture material.

A novel 3D cell culture scaffold using CNF surfaces modified with concentrated polymer brushes (CNF-CPBs) has been developed. [25] Previous reports indicate that surface-initiated living radical polymerization (LRP) on various materials can form well-defined concentrated polymer brushes (CPBs). [26–28] Compared to traditional semi-dilute polymer brushes (SDPBs), CPBs have high graft density, causing unique properties, such as compression resistance, enhanced lubrication, and size-exclusion effect. [29–31] As reported in an earlier publication, grafting charged CPBs onto CNF improves its dispersibility, and flocculation is driven by electrostatic interactions. [25] Floc size depends on the CNF-CPBs concentration, and the process similar to colloidal phenomena. [32]

Previous experiments have shown that cells co-cultured with CNF-CPBs form flocs. The classic Derjaguin-Landau-Verwey-Overbeek (DLVO) theory could provide a theoretical explanation for this flocculation. According to this theory, colloidal flocculation depends on the molecular weight (fiber length) of the flocculant. [33] Using this theory, flocculation of cells and CNF-CPBs should be dependent on the CNF-CPBs length, and independent of the cell type. In this study, cell type and CNF length were systematically changed to investigate the validity of the DLVO theory in explaining the flocculation process. Concentrated poly(p-styrenesulfonic acid sodium salt) (PSSNa) brushes were grafted onto CNFs (CNF-PSSNa) of different length by surface-initiated atom transfer radical polymerization (SI-ATRP), followed by cell cultures with three different cell lines at different concentrations. The three cell types spontaneously flocculated with CNF-PSSNa. By comparing the floc size, cell activity, and specific gene expression, the adsorption behavior of CNF-PSSNa and cells were analyzed using colloidal flocculation. Floc size was dependent on the CNF-PSSNa length, and different cell lines showed similar flocculation. The expression of specific genes in 2D cell culture was compared to 3D cell culture systems for future applications (Figure 3.1).

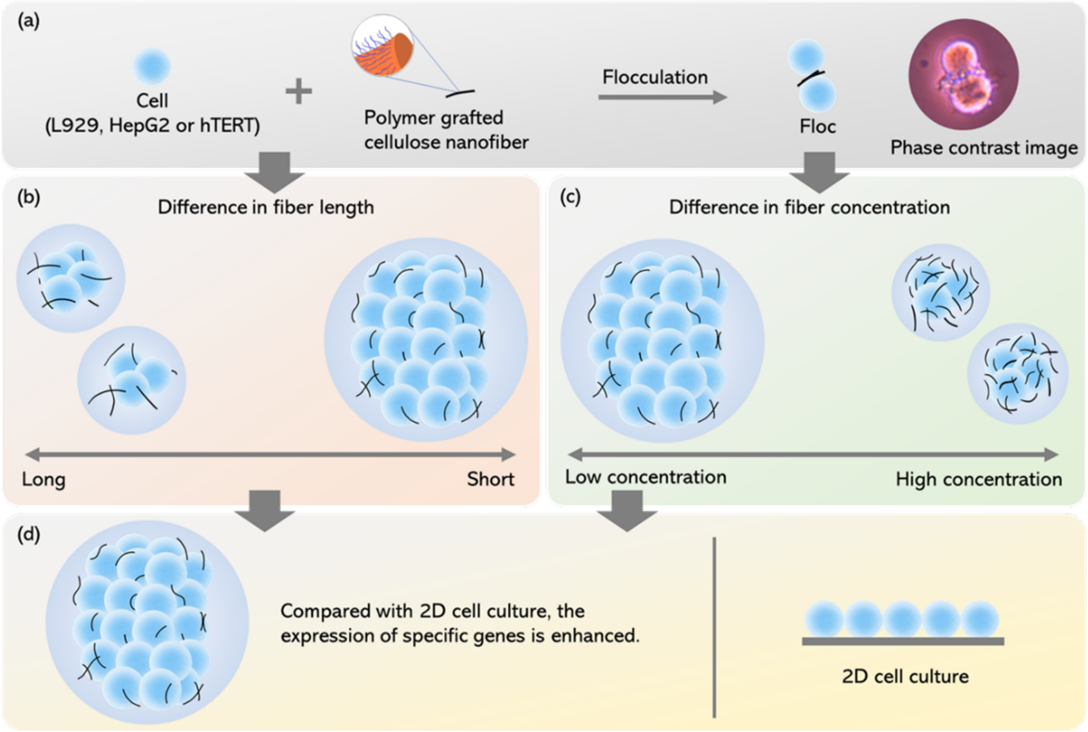

Figure 3.1: Use of CNF-PSSNa for 3D cellular flocculation. (a) Cells form floc with CNF-PSSNa. (b), (c) Floc size could be controlled via fiber length and concentration. (d) Enhancement of specific genes of cell in flocs.

3.2 Materials and methods

3.2.1 Materials

Five types of CNFs (approximately 2 wt% in aqueous slurry) with different fiber lengths were purchased from Sugino Machine, Ltd., Toyama, Japan. 2-Bromoisobutyryl bromide (BiBB 97%) was purchased from Alfa Aesar Co., Inc., Ward Hill, United States. Anhydrous pyridine, *N*-methylpyrrolidone (NMP), toluene, CuBr (99.99%), $CuBr_2$ (99.99%), sodium dodecyl sulfate (SDS), and bovine serum albumin (BSA) were obtained from FUJIFILM Wako Pure Chemical Co., Ltd., Osaka, Japan. *p*-Styrenesulfonic acid sodium salt (SSNa, 99.9%), poly(ethylene glycol) methyl ether 2-bromoisobutyrate (PEGBr), and paraformaldehyde were purchased from Sigma-Aldrich Co. LLC, St. Louis, United States. 2,2'-Bipyridine (bpy, 99.9%), *t*-butyl alcohol, and Triton X-100 were purchased from Nacalai Tesque, Inc., Kyoto, Japan. Alexa Fluor 555 phalloidin and ProLong Gold antifade reagent with 4',6-diamidino-2-phenylindole (DAPI) were obtained from Thermo Fisher Scientific, Inc., Waltham, MA, USA. All the chemicals were used directly without further purification.

3.2.2 Synthesis of CNF-Br

CNF-Br with different lengths were prepared according to a previous study. [25] Synthesis results are shown in Table 3.2.

3.2.3 SI-ATRP of SSNa from CNF-Br

SI-ATRP of SSNa from CNF-Br was carried out using the method reported in a previous publication. [25] After polymerization, the CNF-PSSNa was washed with water. The number-averaged molecular weight (M_n) and polydispersity index of the free polymer were determined by gel permeation chromatography (GPC; Shodex GPC-101, Tokyo, Japan) equipped with columns (LF804 (300 × 80 mm; bead size = 6 μm; pore size = 20–3000 Å), Shodex, Tokyo, Japan) using water and acetonitrile (6:4) with 10 mM LiCl as an eluent at a 0.8 mL/min flow rate. The number-average molecular weight (M_n) and the polydispersity index (PDI) of the free PSSNa were estimated by the calibration data of PSSNa standards (Sigma Aldrich). The graft density of PSSNa was determined by elemental analysis (EA), according to previous report. [25] Results are summarized in Table 3.2.

3.2.4 Atomic force microscopy (AFM) measurement

Fiber length was analyzed using the MFP-3D Origin (Oxford Instruments, Abingdon, United Kingdom). For measurement, different lengths of 0.01 wt% CNF-PSSNa were spin-coated (3000 rpm x 1 min, MIKASA MS-A100) on a poly(ethylene imine)-adsorbed silicon substrate. An AFM instrument equipped with an OMCL-AC160TS-R3 cantilever (Olympus, Tokyo, Japan) was used in tapping mode, with 10×10 μm^2 scanning area and 1.5 Hz scanning rate. The results of AFM are processed with open-source software Gwyddion, and images including AFM and subsequent images analyzed by ImageJ.

3.2.5 Zeta potential measurement

Zeta potential measurements were carried out on a Zetasizer Nano ZS (Malvern Instruments, Ltd., Malvern, United Kingdom) for 0.1 wt% CNF-PSSNa suspensions in Milli-Q water and phosphate buffer saline (PBS). All measurements were performed in triplicate.

3.2.6 Protein adsorption test

CNF-PSSNa (0.5 wt%) were suspended in 1 ml of low glucose-Dulbecco's modified Eagle's medium (DMEM, Thermo Fisher Scientific, Inc., Massachusetts, United States), containing 10% fetal bovine serum (FBS, Thermo Fisher Scientific, Inc.). After incubation at 37 °C for 1 h, FBS was removed, and the CNF-PSSNa was washed with 10 mL PBS five times to remove unbound proteins, placed in 1 ml SDS (5%), vortexed, and sonicated several times to recover the adsorbed proteins. Supernatants were collected for protein concentration determination by a bicinchoninic acid (BCA) assay kit, using an albumin BSA standard curve, according to the manufacturer's instructions (Thermo Fisher Scientific, Inc.). The absorbance of the BCA solutions wase measured at 562 nm using a microplate reader (Infinite M Nano+, Tecan, Ltd., Männedorf, Switzerland). Adsorption tests were performed in triplicate.

3.2.7 Cell cultures

HepG2, L929 (American Type Culture Collection, Manassas, United States), and hTERT (immortalized human chondrocytes, Applied Biological Materials, Inc., Richmond, Canada) cells were used. Cells were cultivated in DMEM with 10% (v/v) FBS and 1% (v/v) penicillin/streptomycin (Nacalai Tesque, Inc.) at 37 °C in a 5% CO_2 incubator. After three or four passages, the cells were harvested by trypsin/EDTA treatment, and subsequently used for the evaluation of CNF-PSSNa.

3.2.8 Cell culture with CNF-PSSNa

The cells were mixed with CNF-PSSNa solutions of different lengths with different concentration (0.005, 0.05, and 0.1 wt%), at 5×10^5 cells/mL density for hTERT, and 1×10^5 cells/mL density for HepG2 and L929 cells. The mixtures were cultured for up to 3 weeks, changing the medium every 2 days. Phase-contrast micrographs of cells with CNF-PSSNa were acquired using a fluorescence microscope (BZ-X800, Keyence Co., Ltd., Osaka, Japan).

3.2.9 Confocal laser microscope observation

The cells with CNF-PSSNa were washed with PBS, fixed with 4% paraformaldehyde, washed with PBS, treated with 0.1% Triton X-100 for permeabilization (15 min), washed with PBS, and incubated with 1 wt% BSA (30 min). For visualized F-actin, the samples were incubated with Alexa Fluor 555 phalloidin (1 h in the dark), mounted on glass slides embedded in DAPI. For staining of cadherin, sample was incubated with primary antibody E-Cadherin ((4A2) Mouse mAb #14472, Cell Signaling Technology, MA, US) over night after block by BSA. Followed by washed with PBS and then cultured for 2 hours in the dark with presence of secondary antibody Goat Anti-Mouse IgG H&L (ab150116, Abcam, Cambridgeshire, United Kingdom). The sample was then embedded in DAPI. Obversion was performed with a confocal laser microscope, FV1000D (Olympus, Tokyo, Japan).

3.2.10 Terminal deoxynucleotidyl transferase dUTP nick end labeling (TUNEL) assay

After 3 weeks, cells cultured with CNF-PSSNa were washed with PBS and fixed with 4% PFA. Cell viability was determined by the TUNEL assay according to the manufacturer's instructions (MK500, Takara Bio, Inc., Shiga, Japan). Cryo-sections (3 μm thickness) were washed with Milli-Q water and PBS, 100 μL permeabilization buffer was applied and kept on ice for 2–5 min. After PBS-washing the slides, 50 μL labeling reaction mixture (consisting of 5 μL Terminal deoxynucleotidyl transferase (TdT) Enzyme and 45 μL Labeling Safe Buffer) was applied. Samples were incubated at 37 °C (60–90 mins). The reaction was terminated by PBS-washing the slides (5 mins) thrice. The nuclei were stained with DAPI (30 mins at 25 °C), washed with PBS, treated with SlowFade Dimond Antifade Mountant (Thermo Fisher Scientific, Inc.), and observed under a fluorescent microscope.

3.2.11 Quantitative real-time polymerase chain reaction (qRT-PCR)

Two genes, ALB and NH4a, were selected for analysis. Gene expression profiles of cells cultured in 2D and 3D, for up to 14 days, were determined using qRT-PCR. After culturing, the cells were collected using a pipette and PBS-washed thrice. Cell lysis was performed using a grinder (FastPrep-24 5G, MP-Biomedicals, Santa Ana, United States) and RNA extraction was performed using the RNeasy Mini kit (QIAGEN, Venlo, Netherlands), following the manufacturer's protocol. RNA concentration was measured by spectrophotometry (NanoDrop, Thermo Fisher Scientific, Inc.). Reverse transcription of cDNA was carried out using the PrimerScript RT reagent kit (Takara Bio, Inc., Shiga, Japan) and qRT-PCR was carried out on a LightCycler 480 system (Roche, Basel, Switzerland). The glyceraldehyde-3-phosphate dehydrogenase (GAPDH) gene was selected as an endogenous control. Primers used in this study are listed in Table 3.1.

Table 3.1: Primers used in qRT-PCR.

Primers	Nucleotide sequence
HNF4A_forward	5'-TGTCCGACAGATCACCTC-3'
HNF4A_reverse	5'-CACTCAACGAGAACCAGCAG-3'
ALB_forward	5'-AAAGAATCTAATAGAGTGGTACAGC-3'
ALB_reverse	5'-AAGAAACTAGAAATCCTCTACCGA-3'
GAPDH_forward	5'-AAGGTGAAGGTCGGAGTCAAC-3'
GAPDH_reverse	5'-GGGGTCATTGATGGCAACAATA-3'

3.2.12 Statistical Analysis

All data are expressed as mean ± standard deviation (SD). To compare data among more than 3 groups, a one-way ANOVA with Tukey's test was used. Differences with less than 0.05 P values were considered statistically significant.

3.3 Results and Discussion

3.3.1 Preparation of CNF-PSSNa

CNF-PSSNa were synthesized as described in a previous publication (Figure 3.2). [25] Table 3.2 shows the characteristics of the original CNF materials used here, and the samples obtained after the two-step reaction (esterification, followed by polymer grafting using SI-ATRP). Here, commercially available CNFs of five different lengths were used, namely, ultralong, long, standard, short, and ultrashort, with degree of polymerization values of 800, 750, 650, 200, and 200, respectively, and viscosities of 7500, 7000, 3000, 2000, and 700 mP.s, respectively (measured by a B-type viscometer with 60 rpm rotation at 25 °C).

After esterification, elemental analysis (EA) was carried out to calculate the degree of substitution of 2-bromoisobutyryl moieties (DS), and the average number of hydroxyl groups substituted to 2-bromoisobutyryl per anhydroglucose unit (Table 3.2). The DS values around 0.22–0.57 were in the same order with the values reported previously, confirming the surface introduction of the SI-ATRP initiators was high enough for the subsequent polymer grafting. [25] After the SI-ATRP of SSNa on CNF-Br, free PSSNa was simultaneously obtained during the grafting, which was used as a reference for obtaining the number-average molecular weight (M_n) and the polydispersity index (PDI) of the graft chains, M_n was found to be 9000 with a PDI of around 1.2. Graft density (σ) was calculated based on the sulfur content measured by EA, where σ was 1.0 chains/nm^2. [25] On the other hand, dimensionless graft density (σ^*) was estimated by the product of σ and the cross-sectional area of per monomeric unit of PSSNa, which was calculated by assuming the polymer density as 1 g/cm^3 and the length of per monomer unit (SSNa) as 0.25 nm. According to the definition of CPB graft density ($\sigma^* > 0.1$), each brush can be categorized into CPB. [30] The σ^* was higher than the theoretical value (it is theoretically impossible to exceed 1.0), and this is because the calculations were done using by assuming the CNF surface area, density as well as the length of monomer unit. The results are in accordance with the previous report. [25] Studies confirmed that all CNFs were covered with similar CPBs.

CNF-PSSNa lengths were confirmed by AFM (Figure 3.3). Fiber lengths are summarized in Table 3.2. As expected, we can obtain the CNF-PSSNa with five different lengths.

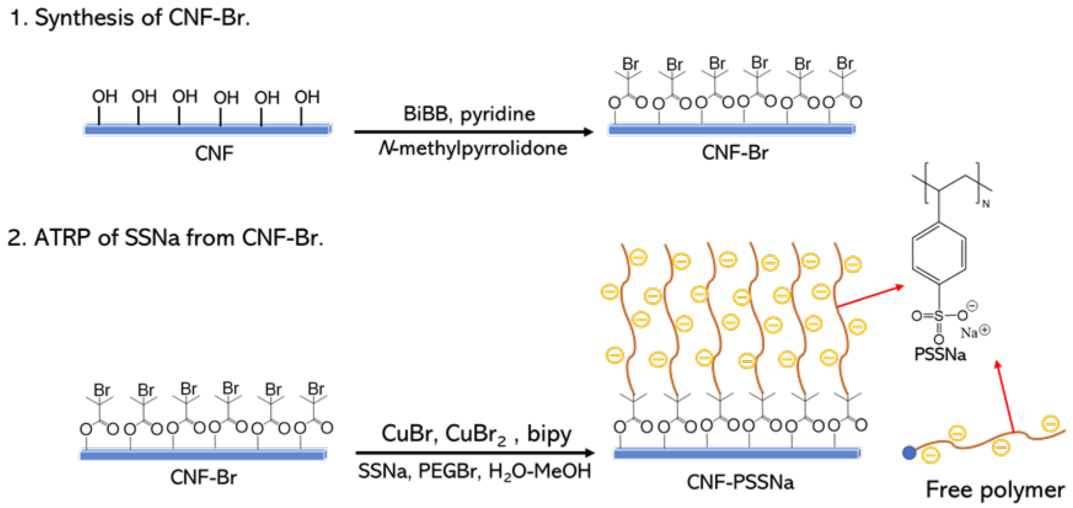

Figure 3.2: Overview of the two-step synthesis.

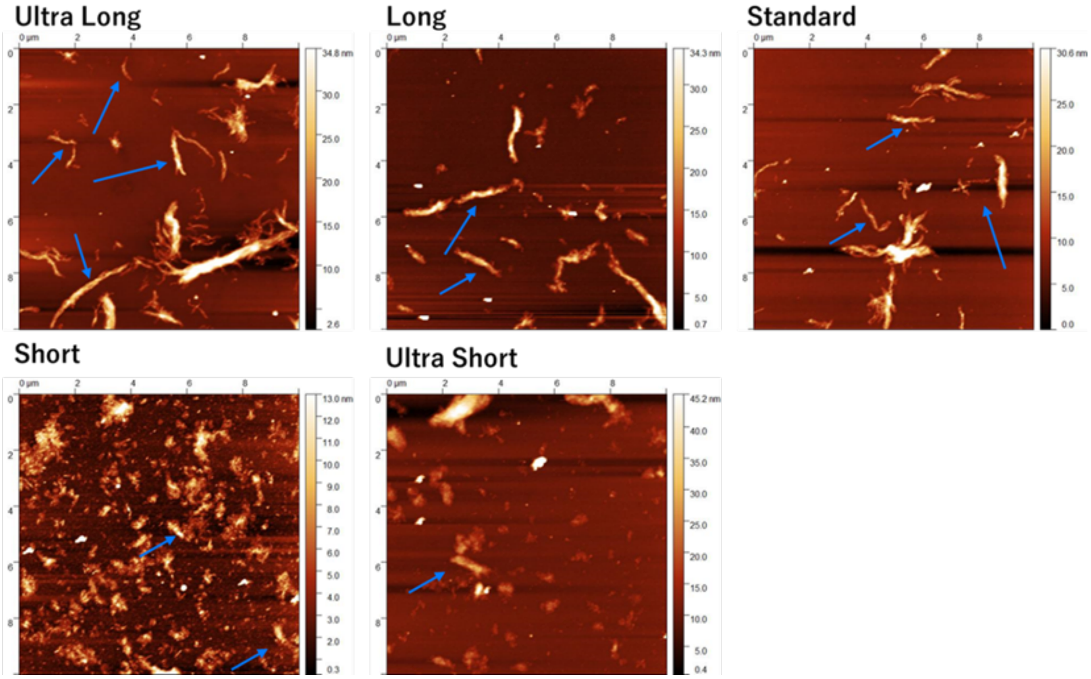

Figure 3.3: AFM images of different fiber lengths of CNF-PSSNa. The arrow indicates the isolated and dispersed fiber used for measurement.

Table 3.2: Properties of CNF-PSSNa.

Fiber parameters[a]			Esterification				Polymer grafted					Fiber length[h]
Grade	η(mPa.s)	DP[b]	%C[c]	%H[c]	%Br[c]	DS[d]	M_n	PDI	DP_n[e]	σ[f]	σ*[g]	(μm)
Ultralong	7,500	800	40.54	5.41	13.42	0.36	9.2×10^3	1.24	44.4	1.06	1.45	1.8 ± 1.1
Long	7,000	750	40.74	5.66	10.97	0.28	8.0×10^3	1.22	38.8	0.99	1.36	1.3 ± 0.74
Standard	3,000	650	39.54	5.15	18.38	0.57	8.5×10^3	1.23	41.4	0.76	1.04	1.1 ± 0.57
Short	2,000	200	40.87	5.85	9.09	0.22	8.6×10^3	1.22	41.7	1.12	1.53	0.29 ± 0.11
Ultrashort	700	200	40.87	5.76	10.87	0.28	9.0×10^3	1.22	43.7	1.11	1.52	0.16 ± 0.05

[a]Provided by the manufacturer. [b]Degree of polymerization values of CNF. [c]The content of element measured by E.A. [d]Degree of substitution. [e]Degree of polymerization values of grafted PSSNa. [f]Graft density (σ, group/nm^2). [g]Dimensionless graft density (σ*), σ* = Sσ, where S is the cross-sectional area per monomeric unit of PSSNa. [h]Fiber length of CNF-PSSNa determined by AFM.

3.3.2 Preparation of CNF-PSSNa

Zeta potentials of the CNF-PSSNa were measured in MilliQ water and PBS buffer (Table 3.3). Surface charges influence cell interactions. As shown in Table 3.3, the similar Zeta-potentials among the CNF-PSSNa samples confirmed similar CPBs coatings on the CNFs. Zeta potential depends on the dispersion medium, and showed different values in water and PBS due to polyelectrolyte charge-shielding by PBS. [34]

Table 3.3: Zeta-potentials of CNF-PSSNa in water and PBS.

CNF-PSSNa	zeta potential in PBS (mV)	zeta potential in water (mV)
CNF type		
Ultralong	-27.12 ± 1.50	-39.03 ± 0.73
Long	-30.38 ± 1.35	-41.10 ± 0.22
Standard	-29.50 ± 1.36	-44.83 ± 0.95
Short	-35.65 ± 1.49	-44.40 ± 0.73
Ultrashort	-31.22 ± 1.48	-39.47 ± 1.14

3.3.3 Protein adsorption

Protein adsorption of CNFs was investigated before and after PSSNa grafting. Protein adsorption properties of a biomaterial influence its biocompatibility and interactions. [35] Figure 3.4 shows the FBS protein adsorption by CNFs at 37 °C for 1 h. Regardless of the length of the fiber, approximately the same amount of protein was attached on each CNF-PSSNa. Unmodified CNF showed negligible protein adsorption (0–0.001 mg/mg). Surface charge of polymers affect protein adsorption, and the unchanged surface charge of CNF explained its unaltered protein adsorption.

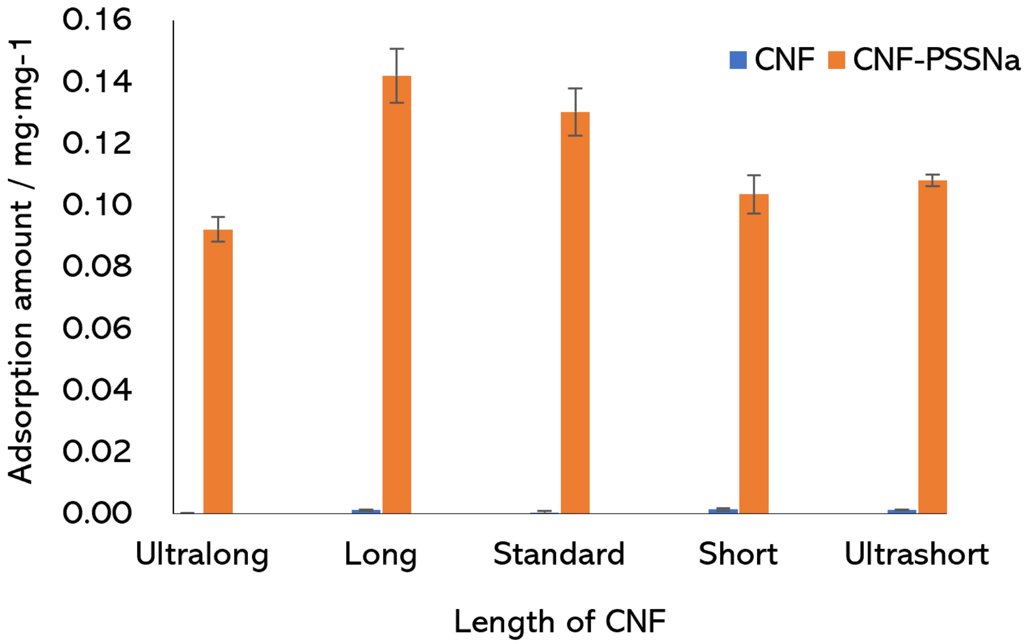

Figure 3.4: FBS adsorbed by pristine and CNF-PSSNa.

3.3.4 *In-vitro* culture

To investigate cell adhesion mechanism of the novel 3D cell culture approach used here, the influence of CNF length, CNF-PSSNa concentration, and different cell-lines (HepG2, L929, and hTERT) were investigated which originate from liver, skin, and cartilage tissues, respectively. Cells co-cultured with CNF-PSSNa of five lengths at three concentrations (0.1, 0.05, and 0.005 wt%) were used for the experiment. Figure 3.5 shows phase-contrast micrographs of HepG2 cells cultured with short-length CNF-PSSNa for up to 21 days. The results of cell culture with CNF-PSSNa are shown in the supplementary material (Figure 3.8 - 3.7). Cells spontaneously flocculated with CNF-PSSNa from the 4^{th} day of cell culture. The floc size increased with cultivation time. Floc sizes were measured using the largest inner diameter of the floc (Figure 3.9). Results are summarized in Figure 3.10.

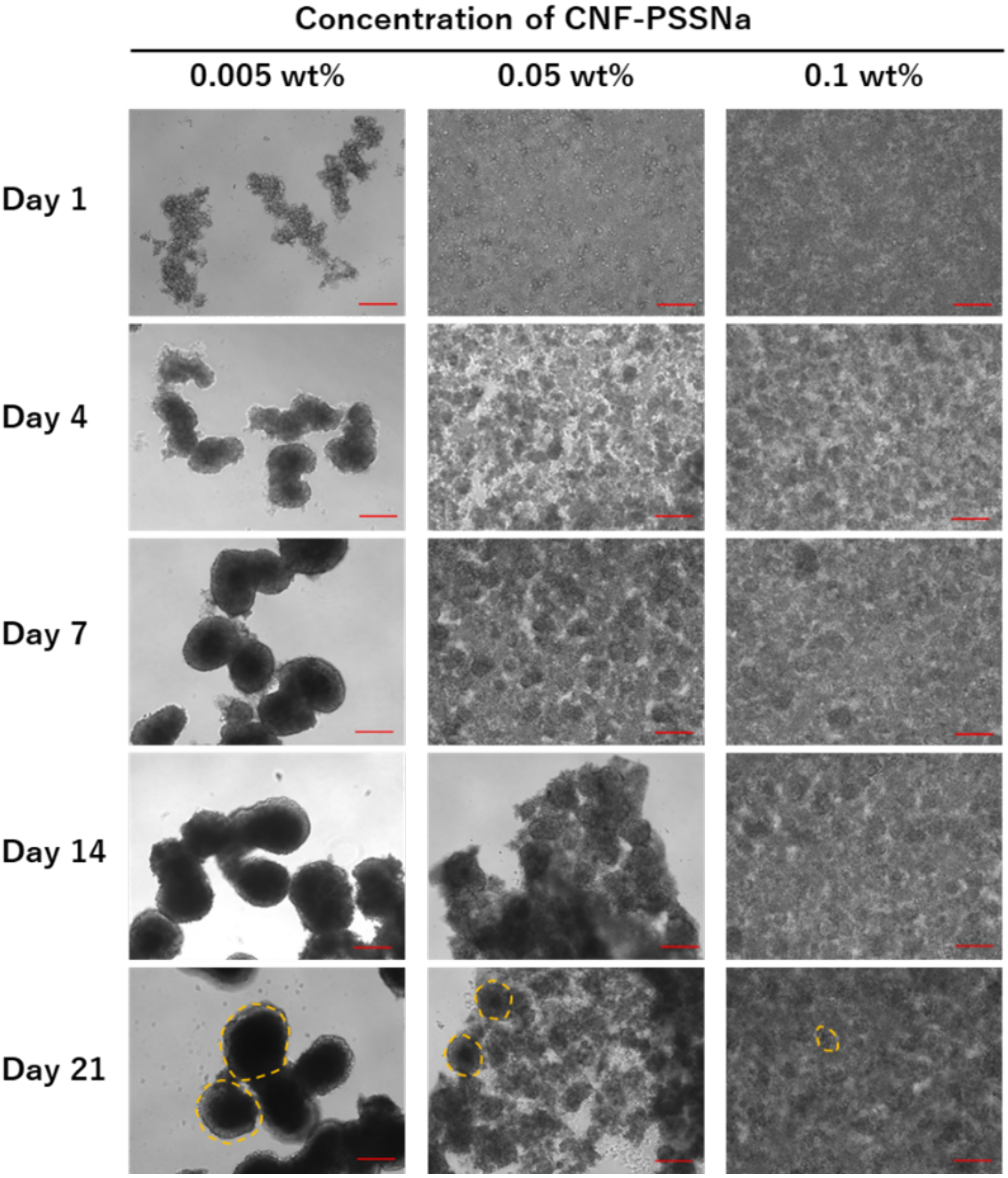

Figure 3.5: Phase-contrast micrographs of the HepG2 and short CNF-PSSNa flocs, cultured for 1, 4, 7, 14, and 21 days. $[\mathrm{HepG2}]_0 = 5 \times 10^5$ cells, CNF-PSSNa=0.005, 0.05 and 0.1 wt%. Scale bar=200 μm. Typical flocs are represented by dotted circles in the Day 21 image.

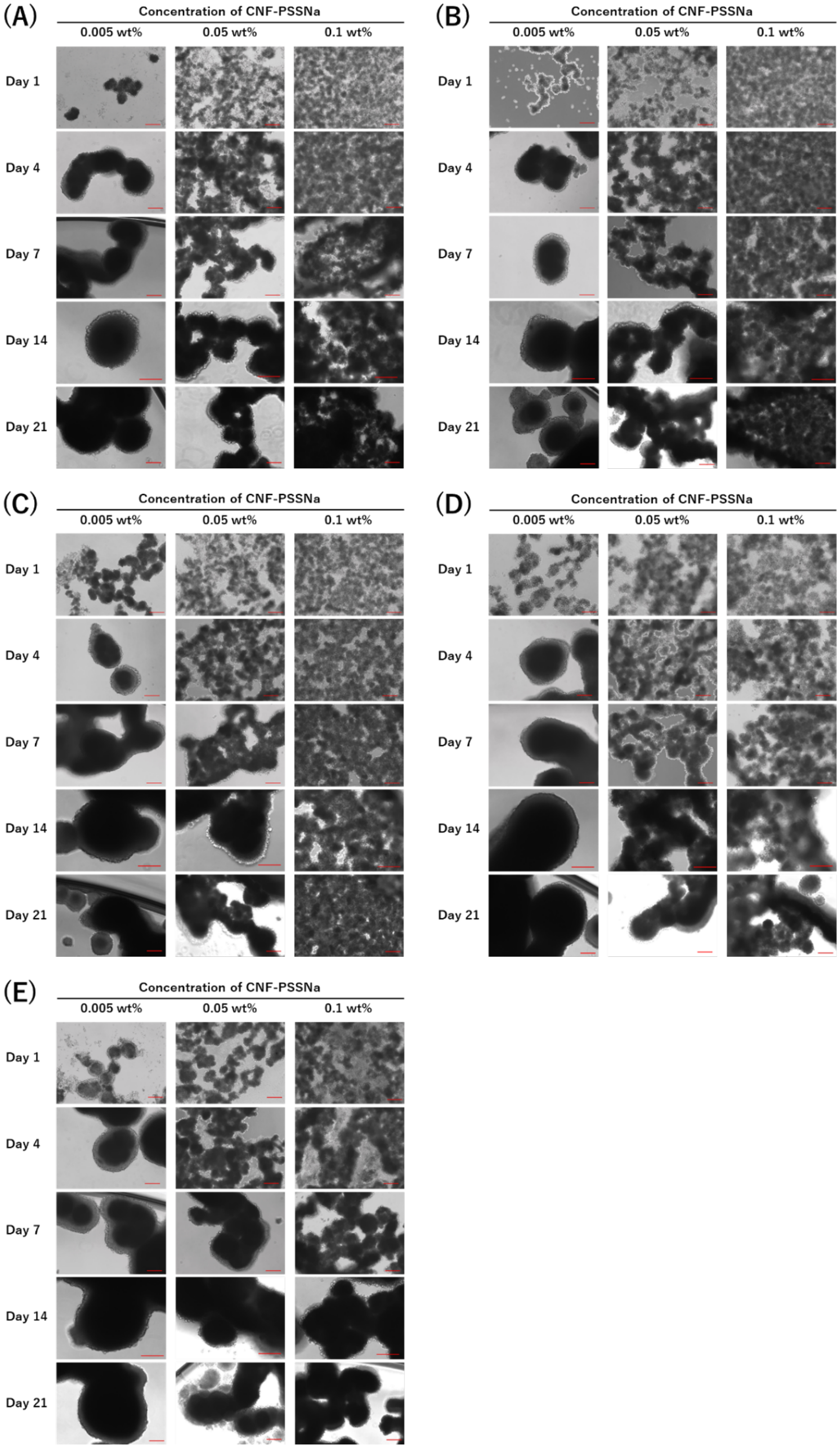

Figure 3.6: Phase-contrast micrographs of L929 and CNF-PSSNa ((A) Ultra long, (B) Long, (C) Standard, (D) Short and (E) Ultra Short) flocs cultured for up to 21 days. $[\text{L929}]_0 = 5 \times 10^5$ and CNF-PSSNa=0.005, 0.05, and 0.1 wt%. Scale bar=200 μm.

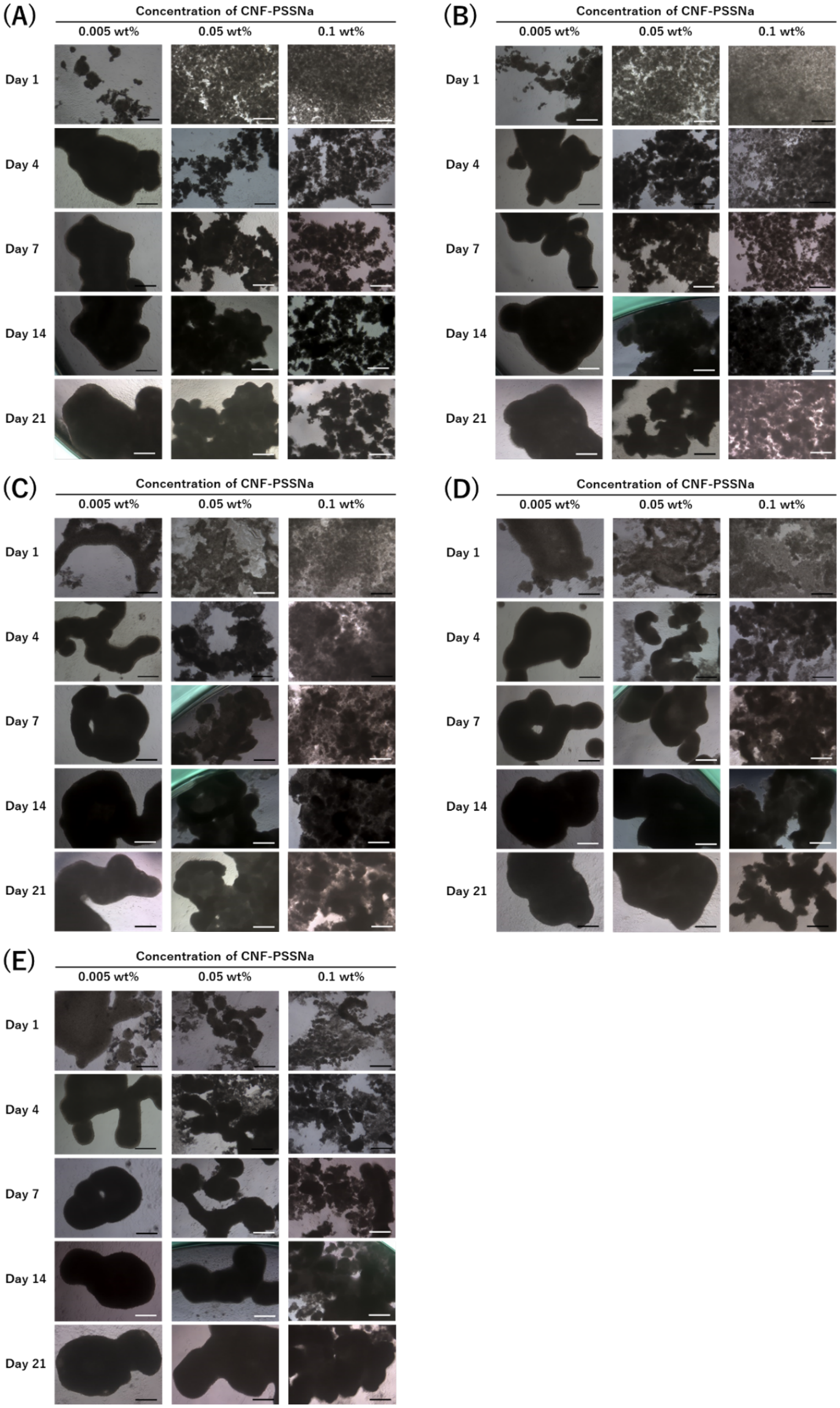

Figure 3.7: Phase-contrast micrographs of hTERT and CNF-PSSNa ((A) Ultra long, (B) Long, (C) Standard, (D) Short and (E) Ultra Short) flocs cultured for up to 21 days. $[\text{hTERT}]_0 = 5 \times 10^5$ and CNF-PSSNa=0.005, 0.05 and 0.1 wt%. Scale bar=500 μm.

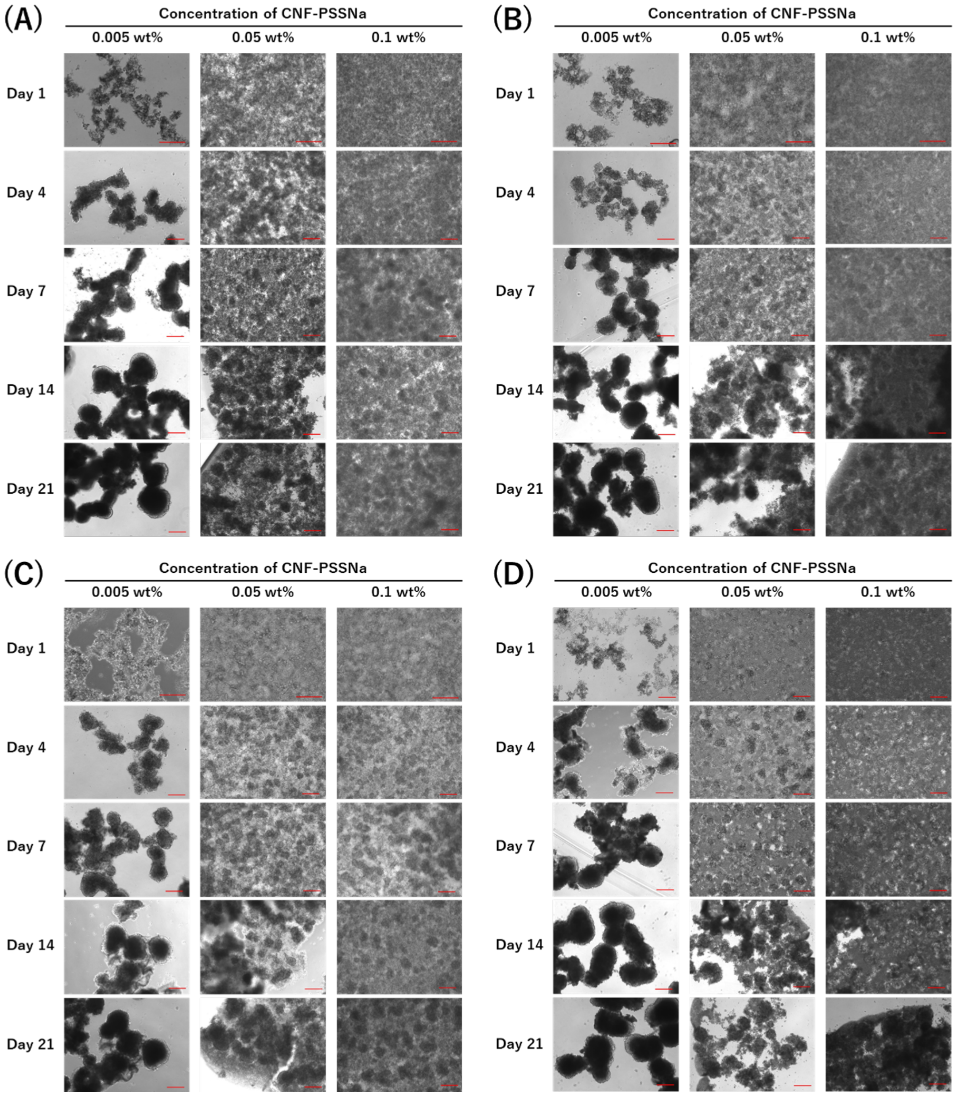

Figure 3.8: Phase-contrast micrographs of HepG2 and CNF-PSSNa ((A) Ultra long, (B) Long, (C) Standard and (D) Ultra Short) flocs cultured for up to 21 days. $[\text{HepG2}]_0$= 5×10^5 cells, and CNF-PSSNa=0.005, 0.05, and 0.1 wt%. Scale bar=200 μm.

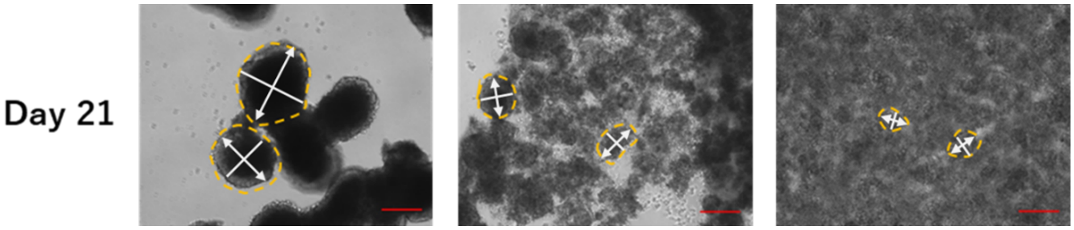

Figure 3.9: Measuring floc size using the longest inner diameter, indicated by the double arrow.

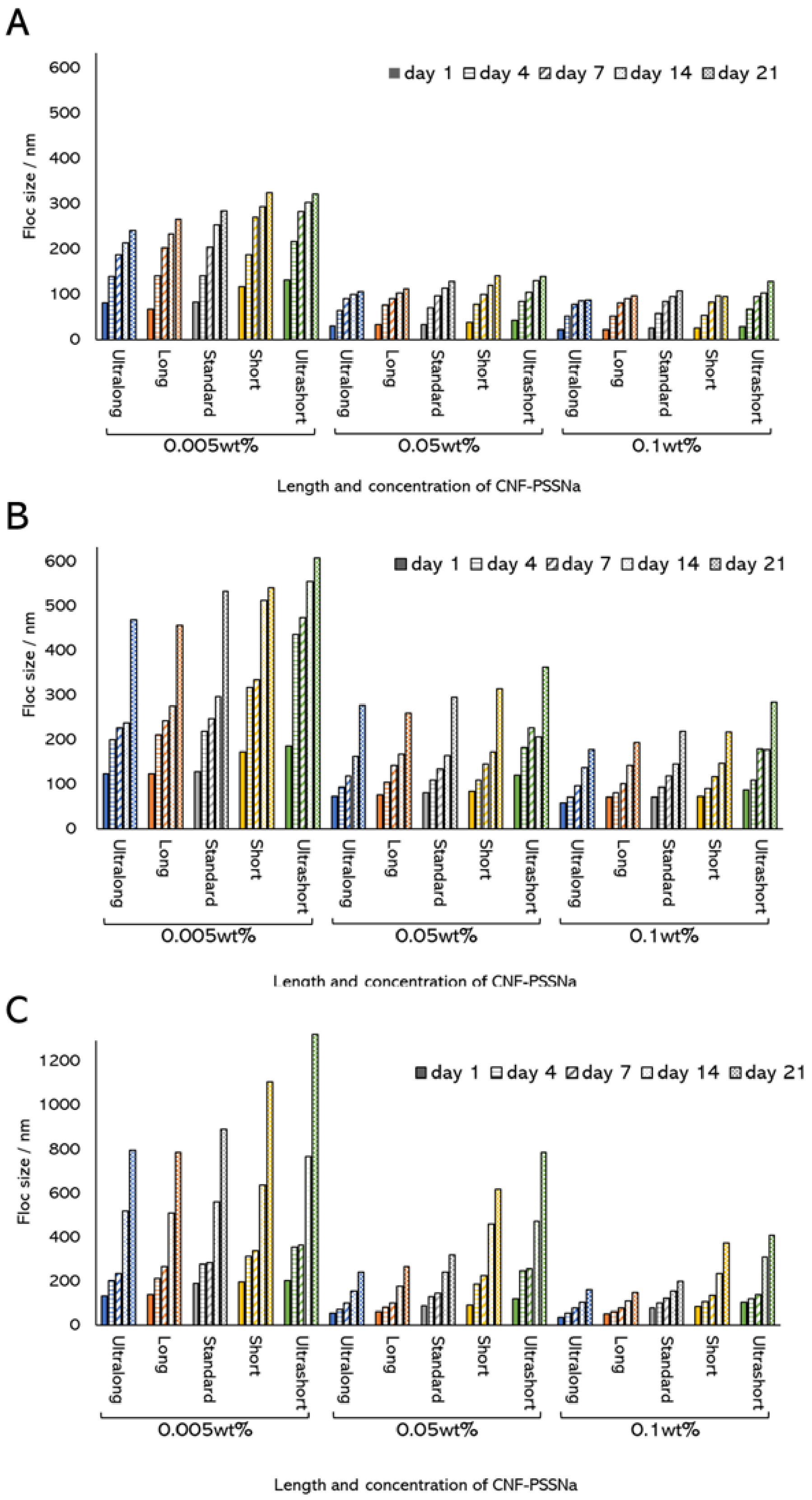

Figure 3.10: Average floc sizes after up to 21 days incubation for (A) HepG2, (B) L929 and (C) hTERT, with CNF-PSSNa.

Floc size increased with increase in cultivation time due to the addition of new cells to the floc, indicating a dynamic 3D cell culture system. Compared to the scaffold-free culture method, this method spontaneously forms size-controllable flocs, without the use of complicated equipment or operations. [10] Incorporating cells into pre-formed scaffolds is challenging due to their limited pore size and porosity, and the developed method offers significant advantages over it. [36]

Figure 3.11A shows floc sizes of cells co-cultured for 7 days with CNF-PSSNa respectively. The floc size decreased with increase in CNF-PSSNa concentration and length. and increased with increase in cultivation time (Figure 3.11B). It is challenging to explain flocculation behavior of cells and CNF-PSSNa in a complex biochemical environment. Here, the DLVO alternating stability theory, first used to explain the adsorption of bacteria in 1971, was employed. [37] According to it, adsorption in this system is based on the cells being regarded as colloidal particles, and reversible adsorption is based on the van der Waals (vdW) force-electrostatic force balance of the polymer. HepG2, L929, and hTERT cells co-cultured with CNF-PSSNa formed spherical flocs, exhibiting similar variations in floc size with change in CNF-PSSNa length and concentration. Therefore, this 3D cell culture system formed flocs of controllable sizes with different cell types.

Though the classic DLVO theory is based on the vdW and electrostatic interaction, here, we considered the additional contribution of the steric interaction arising from the CNF-PSSNa wrapped around the cells on the cellular flocculation. On increasing the fiber concentration, cells wrapped with negatively charged CNF-PSSNa were more dispersed, owing to electrostatic and steric repulsion from both of the CPBs and CNF, resulting in the smaller floc sizes as the CNF-PSSNa concentration increased. [38] This is also supported by the fact that, as shown in Figure 3.12, very high (1 wt%) CNF-PSSNa concentration did not form any flocs with cells, but stably dispersed individual cells in the culture medium. A longer fiber adsorbed on the cell surface generates larger steric repulsion based on its rigidity. Therefore, longer fibers form smaller flocs, and vice-versa. We reasonably concluded that the cellular flocculation conducted by the CNF-PSSNa was systematically explained by the CNF length and concentration. HepG2, L929, and hTERT cells co-cultured with CNF-PSSNa formed spherical flocs, exhibiting similar variations in floc size with change in CNF-PSSNa length and concentration. Therefore, this 3D cell culture system formed flocs of controllable sizes with different cell types.

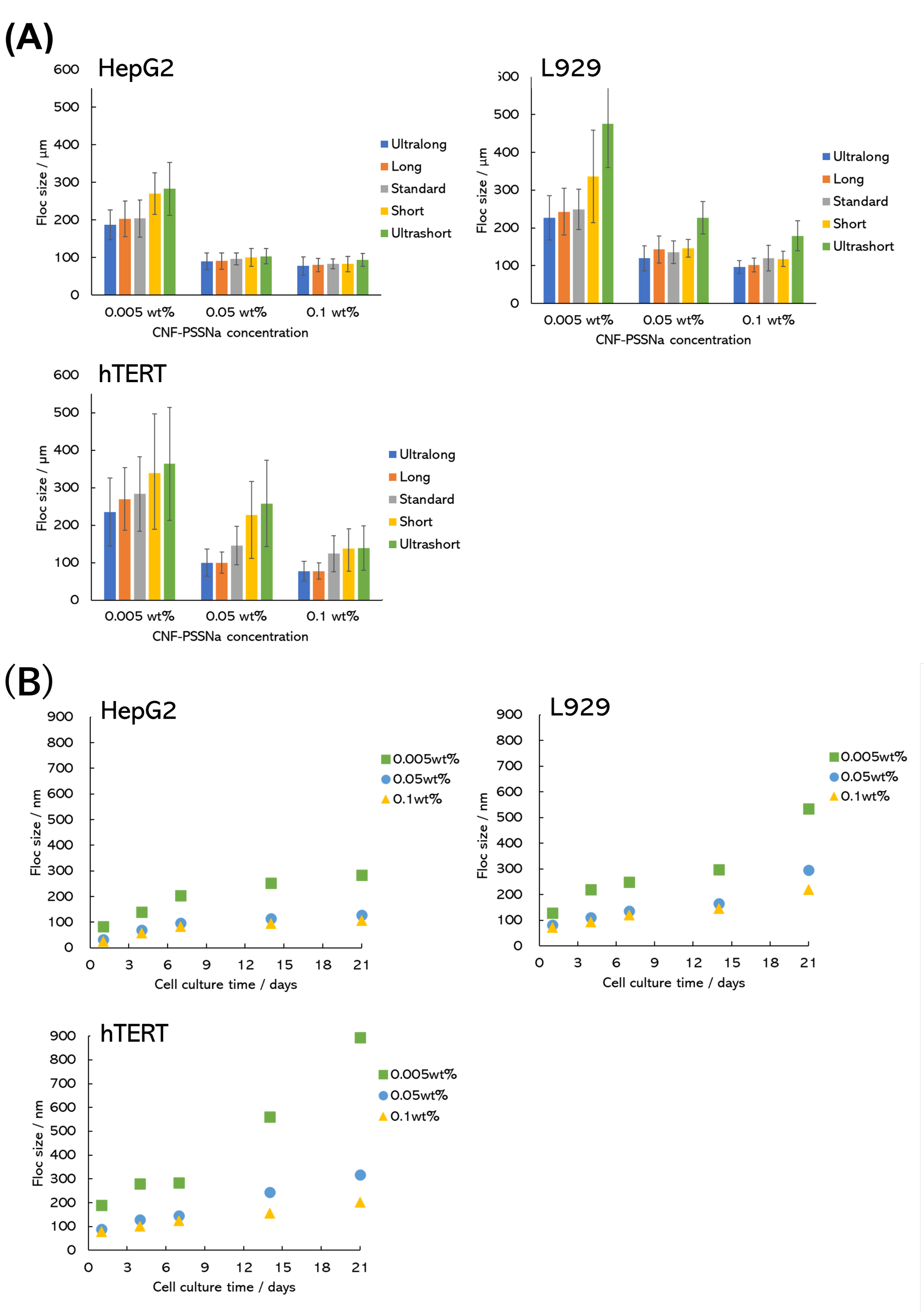

Figure 3.11: Floc size of cells after co-culturing with CNF-PSSNa (A) For 7 days, (B) As a function of culture time.

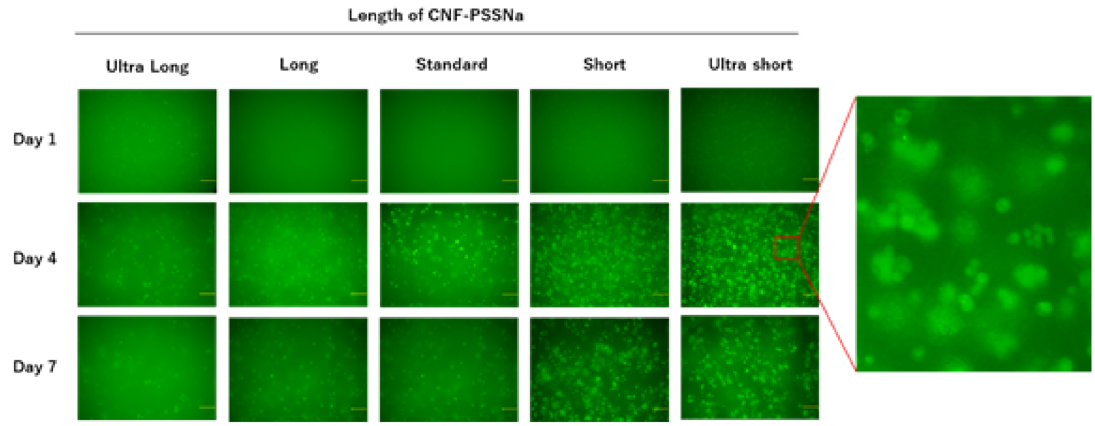

Figure 3.12: Fluorescence micrographs of HepG2 and CNF-PSSNa flocs cultured for up to 7 days stained with calcein-AM where the live cells appear as green fluorescence. $[\text{HepG2}]_0 = 5 \times 10^5$ and CNF-PSSNa=1 wt%. Scale bar=200 μm.

3.3.5 Cell floc morphology by confocal laser microscopy

Immunostaining and 3D confocal imaging were used to determine floc cell locations. Phase separation causes floc cells in the same layer to have inconsistent growth environments, making in-vitro culture analysis difficult. As shown in Figure 3.13 and Figure 3.14, after 21 days of cell culture in different concentrations of CNF-PSSNa, HepG2 and L929 cells were evenly distributed in the floc. CNF-PSSNa concentrations of 0.05 and 0.005 wt% formed independent large flocs. At high concentrations (0.1 wt%), small flocs were observed to bind together. This was consistent with the phase contrast micrographs. Similar variations were observed on culturing hTERT cells with 0.1 and 0.005 wt% CNF-PSSNa with different lengths, as shown in Figure 3.15. The three cell types were evenly accumulated in the flocs formed by different concentrations of CNF-PSSNa. On the other hand, the presence of E-cadherin was observed in the flocs (Figure 3.16), proving the cell-cell contact in the flocs. With increase in culture time, new cells were dispersed in the flocs, without phase separation and formed stable flocs.

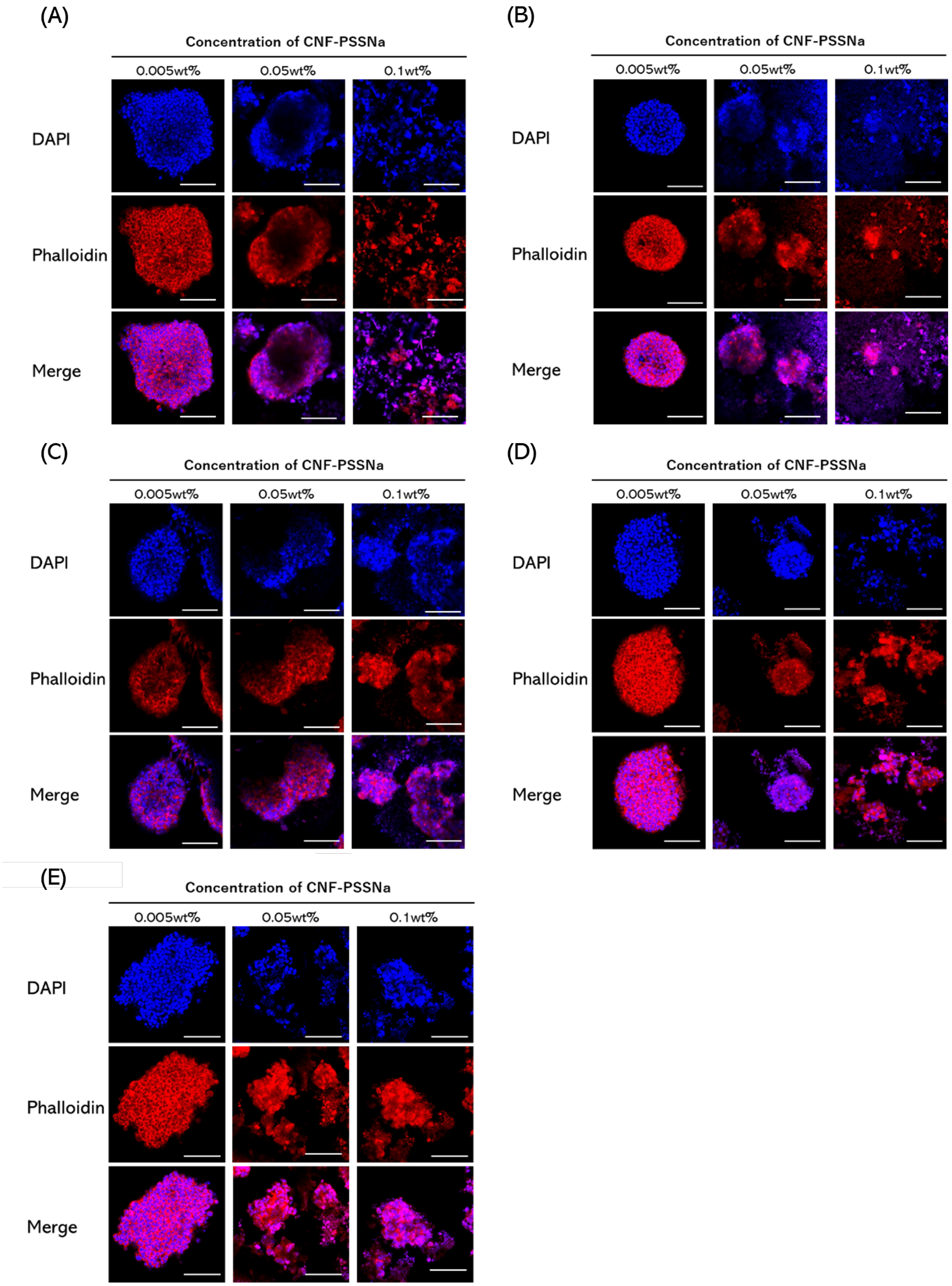

Figure 3.13: Confocal laser microscopy images of the HepG2 cell and CNF-PSSNa ((A) Ultra long, (B) Long, (C) Standard, (D) Short and (E) Ultra Short) flocs cultured for 21 days. Nuclei were counterstained with DAPI (blue), and F-actin was stained with phalloidin (red). Scale bar=100 μm.

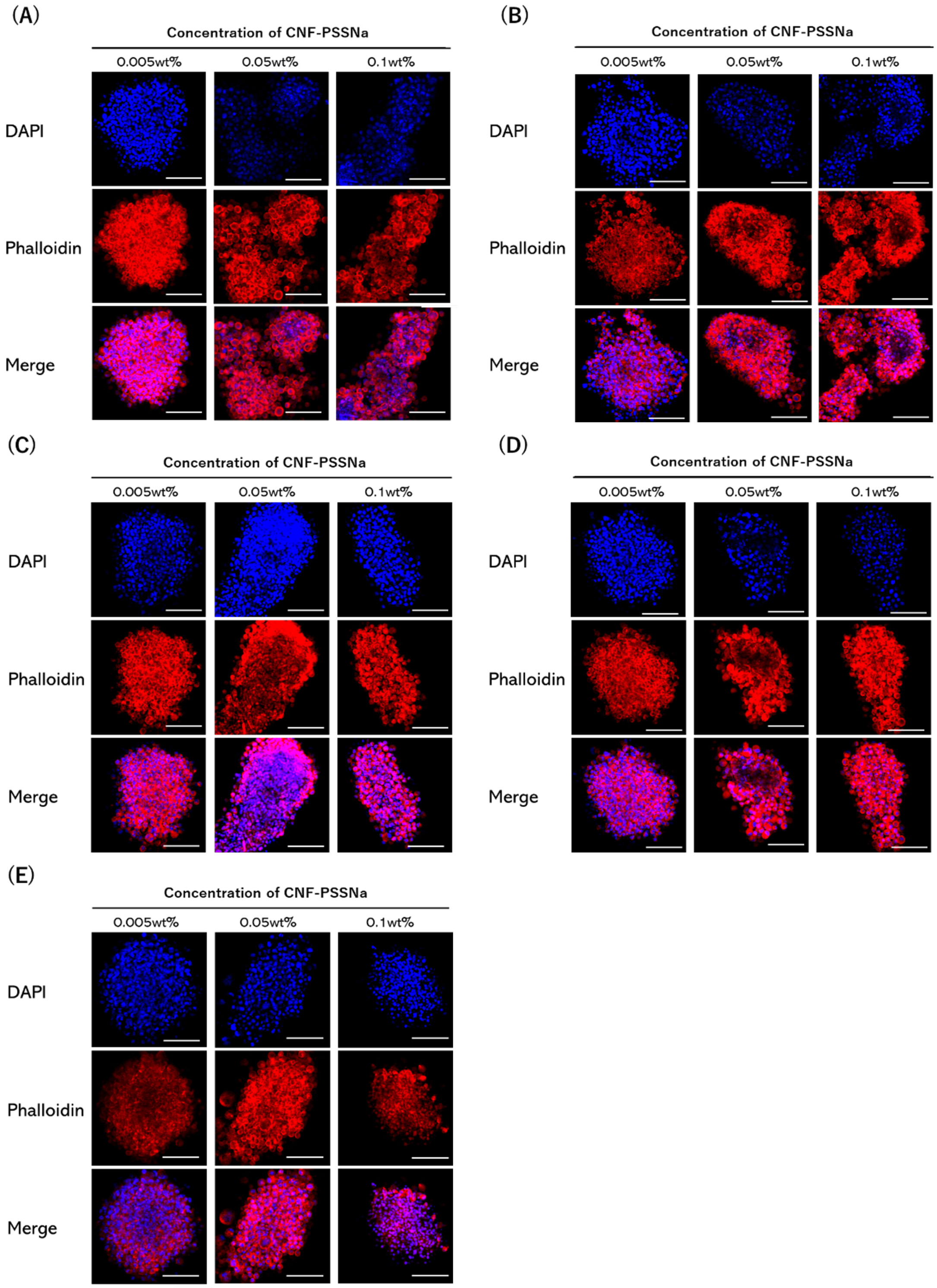

Figure 3.14: Confocal laser microscopy images of the L929 cell and CNF-PSSNa ((A) Ultra long, (B) Long, (C) Standard, (D) Short and (E) Ultra Short) flocs cultured for 21 days. Nuclei were counterstained with DAPI (blue), and F-actin was stained with phalloidin (red). Scale bar=100 μm.

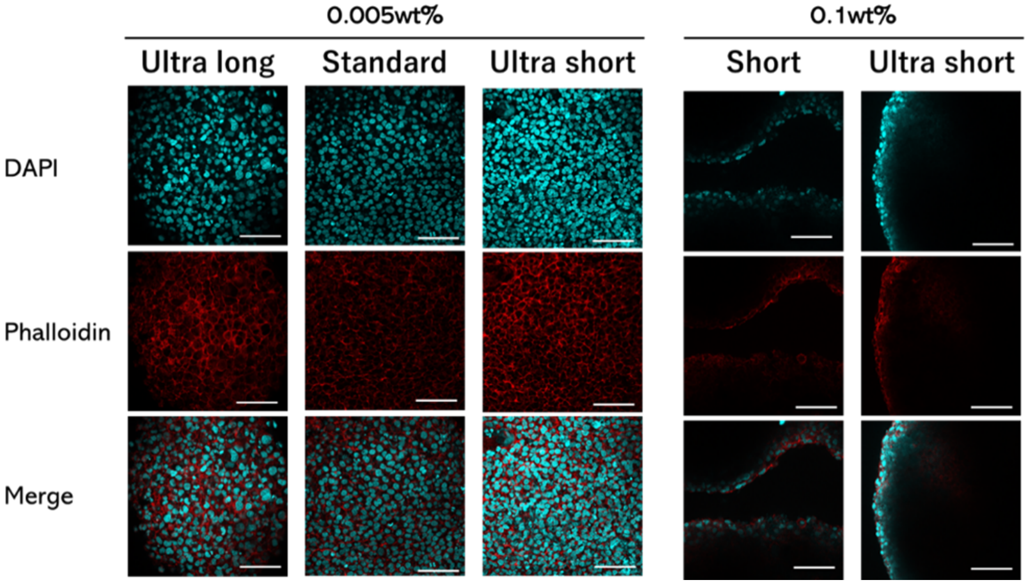

Figure 3.15: Confocal laser microscopy images of the hTERT cell and CNF-PSSNa flocs cultured for 21 days. Nuclei were counterstained with DAPI (blue), and F-actin was stained with phalloidin (red). Scale bar=100 μm.

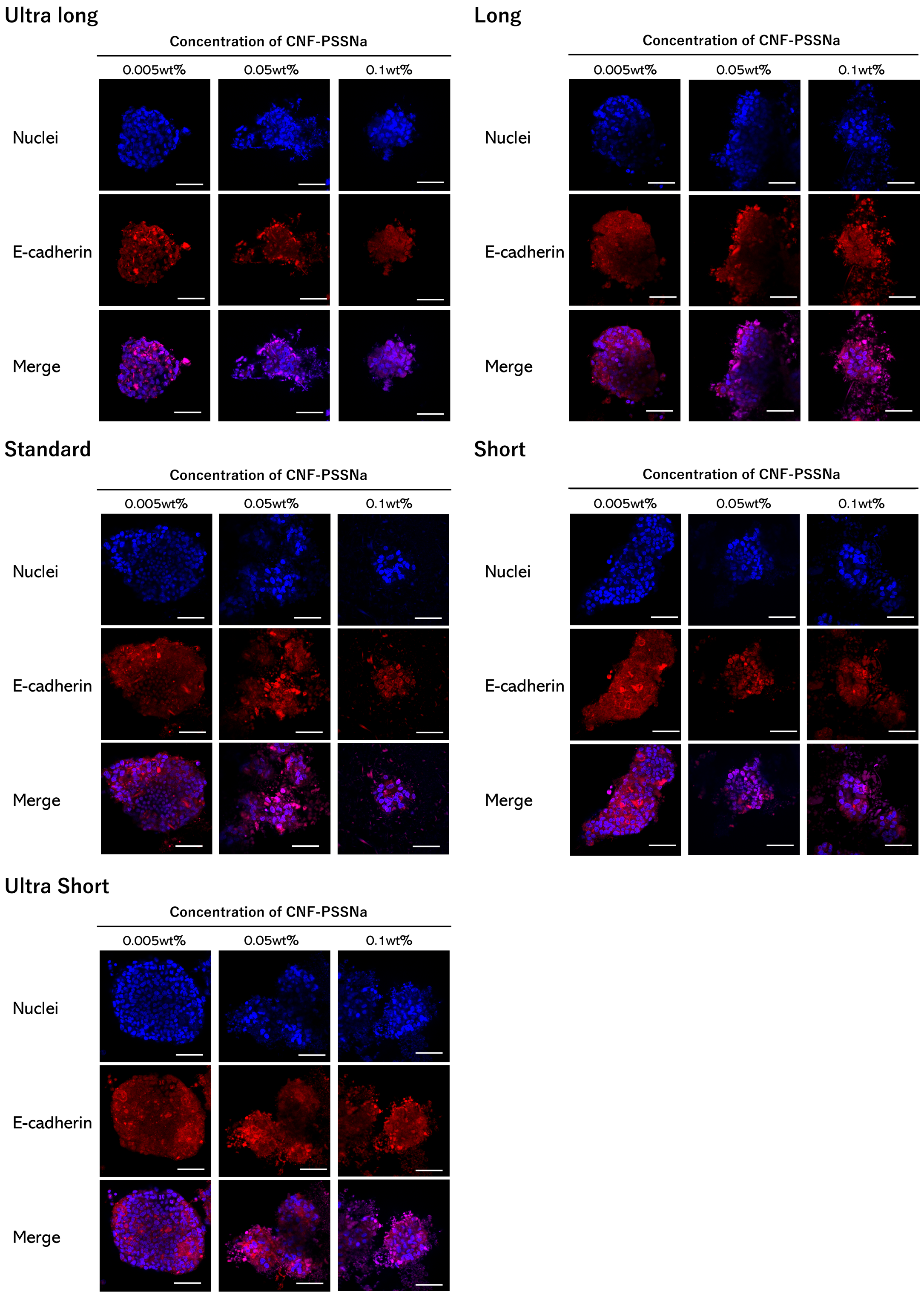

Figure 3.16: Confocal laser microscopy images of the HepG2 and CNF-PSSNa flocs cultured for 7 days, showing nuclei (blue) and E-cadherin (red). Scale bar=50 μm.

3.3.6 TUNEL assay

In spherical 3D cell culture, internal cells cannot obtain sufficient nutrients during spheroid growth, leading to cell apoptosis. [39] To determine internal cell viability, a TUNEL assay was performed on floc sections after 21 days of cell culture, for different CNF-PSSNa lengths (Figure 3.17). The TUNEL assay is a method to quantify apoptotic cells by labeling the free 3-hydroxyl termini of DNA fragmentation, utilizing exogenous TdT. [40] Cells were stained with DAPI and TUNEL (apoptotic cells). The proportion of apoptotic cells is the integrated density of TUNEL fluorescence/DAPI fluorescence (background fluorescence has been removed). Cell viability results are shown in Figure 3.18.

Cells co-cultured with 0.1 wt% CNF-PSSNa displayed high survival rates and negligible TUNEL fluorescence. CNF-PSSNa provide a nutrient channel for the floc cells, improving their viability. Using 0.005 wt% CNF-PSSNa, both HepG2 and L929 cells exhibited low cell viability. Samples co-cultured with ultrashort CNF-PSSNa showed the lowest survival rates due to the accumulation of metabolic waste and insufficient diffusion of oxygen and nutrients to the center of larger flocs. [41]

Differences in cell viability of the different cell types were observed. At 0.005 wt% CNF-PSSNa concentration, unlike HepG2 and L929 cells, the hTERT cells exhibited a high survival rate. This discrepancy could be attributed to the fact that the hTERT cells are cartilage cells having strong adaptability to hypoxic conditions. [42]

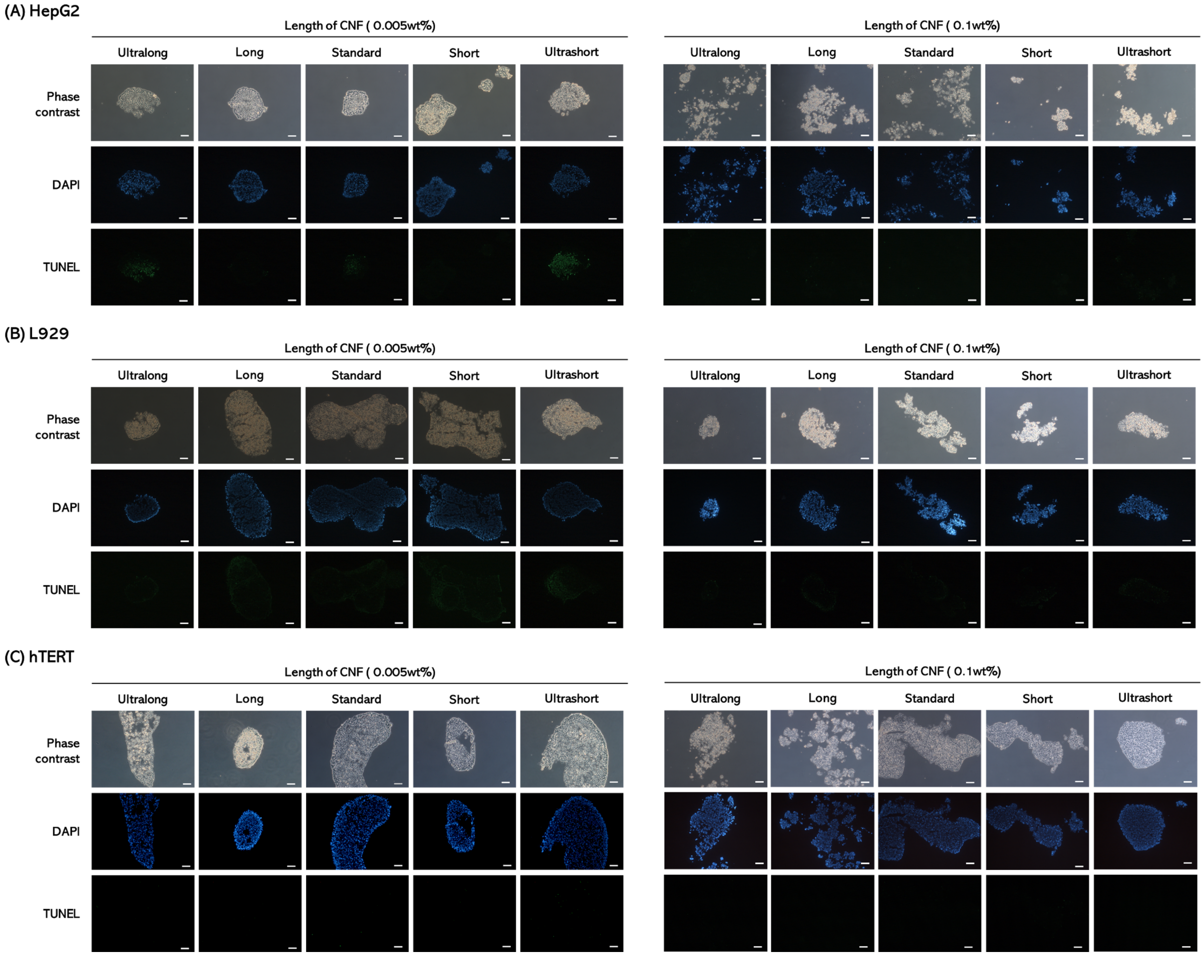

Figure 3.17: Fluorescence micrographs for floc cross-sections using grafted CNF with (A) HepG2, (B) L929 and (C) hTERT cultured for 21 days, showing nuclei (blue) and apoptotic/necrotic cells (green). Scale bar=100 μm.

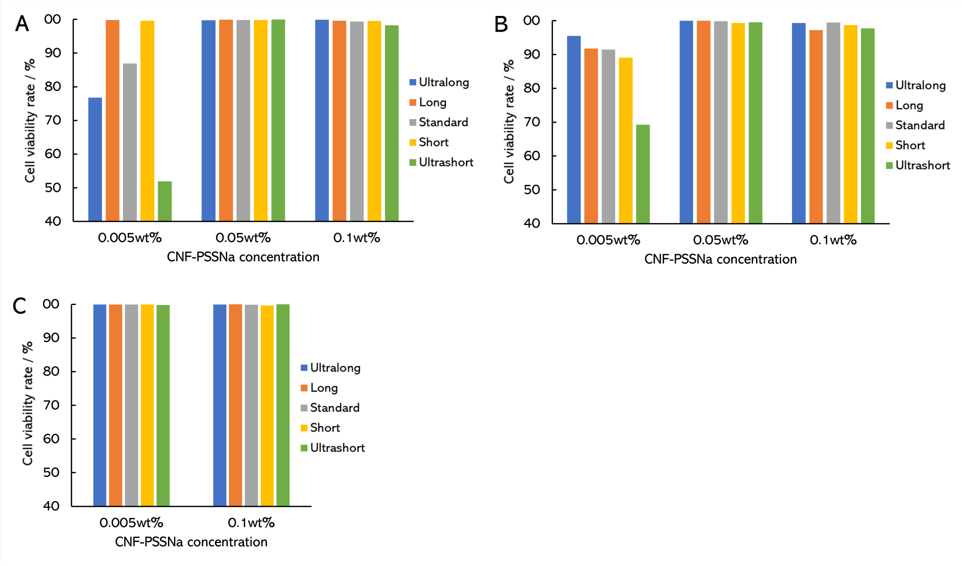

Figure 3.18: Integrated density ratio of DAPI fluorescence in TUNEL assay for the following cell types: (A) HepG2, (B) L929, and (C) hTERT.

3.3.7 RT-PCR

RT-PCR was performed on HepG2 cells co-cultured with CNF-PSSNa to determine hepatocyte-specific functions. The albumin (ALB) levels and hepatocyte nuclear factor, 4α (HNF4A), were measured. One of the vital functions of the liver is the secretion of proteins such as ALB. [43] HNF4A is a nuclear receptor having a wide range of effects on the regulation of liver-specific genes. [44]

As shown in Figure 3.19, ALB and HNF4A gene expressions exhibited differences with an increase in cultivation time. A significant difference was observed with the control group (2D cultured cells) after 14 days of cell culture. Figure 3.20 shows the normalized RNA amounts of CNF-PSSNa samples having different lengths, after 14 days of cell culture. Expression of HNF4A in the experimental group increased significantly compared to the control group. With floc size increase, the expression of HNF4A decreased. ALB gene expression increased after 14 days culture and on decreasing CNF-PSSNa length and concentration. In particular, Short and Ultrashort CNF-PSSNa samples at 0.05 and 0.1 wt% showed expression level more than three and four times higher than the 2D control, respectively. However, Short and ultra-short 0.0005 wt% CNF-PSSNa samples showed low gene expression levels. Similar to the TUNEL assay observations, the flocs of these samples had large diameters, causing inner cell necrosis, leading to a decrease in overall gene expression. Expression of both genes after 14 days culture was significantly higher than that of the control (2D cell culture). Thus, the cell culture system was confirmed to influence 3D culture, as previously reported, and promote differentiation. [45, 46]

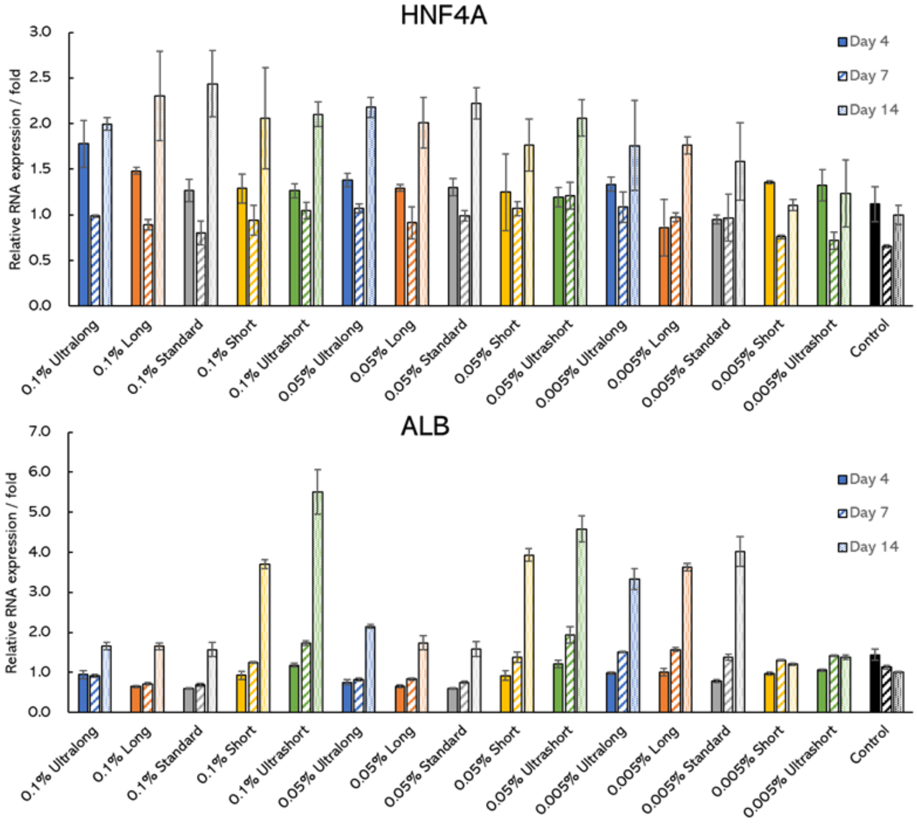

Figure 3.19: Relative RNA expression of HepG2 co-cultured with CNF-PSSNa for up to 14 days normalized with control of day 14.

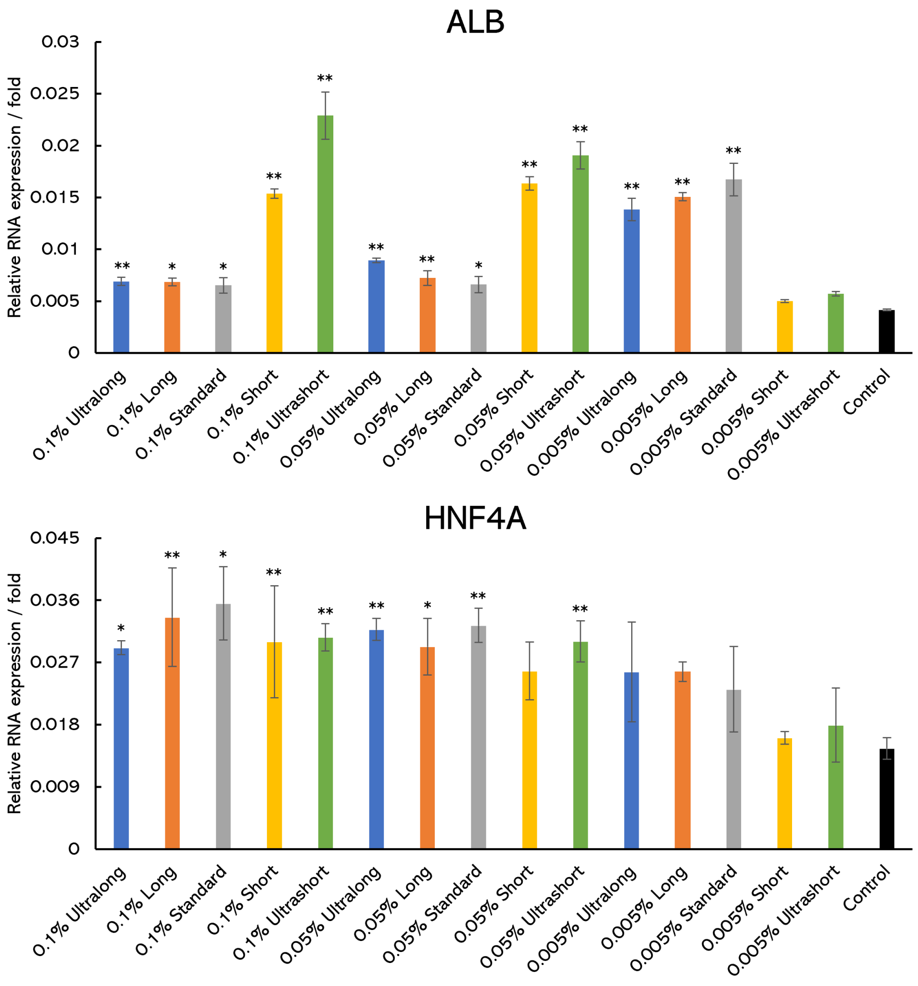

Figure 3.20: Relative RNA expression of HepG2 cells co-cultured with CNF-PSSNa for up to 14 days, normalized with control. The significances, calculated against the control, are marked as *: $p<0.05$, **: $p<0.01$.

Results of HepG2 cells cultured for 14 days are listed in Table 3.4. Decrease in CNF-PSSNa concentration increased floc size. At high CNF-PSSNa concentrations, cells could not bind to all CNF-PSSNa and flocculated on the fibers (represented by floc in the table). In contrast, at low concentrations, cells and CNF-PSSNa flocculated into independent spherical flocs (represented by spheroids in the table). A large floc volume (at 0.005 wt% CNF-PSSNa concentration) was not conducive to cell survival and specific gene expression. It was found that it is necessary to adjust the fiber length and concentration of CNF-PSSNa in order to use it as a new 3D culture field that provides high cell viability and improves of cellular functions.

Table 3.4: Summary of HepG2 cells culture results for 14 days[a].

Fiber length	Concentration (%)	Floc size (μm)	Morphology[b]	ALB[c]	HNF4A[c]	TUNEL assay (Cell viability, %)
Ultralong	0.1	85.8 (±11.6)	floc	1.66 (±0.10)	2.00 (±0.07)	100
	0.05	99.5 (±28.5)	Spheroid	2.15 (±0.05)	2.18 (±0.11)	100
	0.005	215 (±37.4)	Spheroid	3.33 (±0.26)	1.76 (±0.49)	77
Long	0.1	91.1 (±18.1)	floc	1.65 (±0.09)	2.30 (±0.49)	100
	0.05	103 (±19.1)	Spheroid	1.74 (±0.17)	2.01 (±0.28)	100
	0.005	232 (±32.8)	Spheroid	3.63 (±0.09)	1.76 (±0.10)	100
Standard	0.1	95.4 (±13.5)	floc	1.57 (±0.18)	2.44 (±0.36)	99
	0.05	114 (±15.6)	Spheroid	1.59 (±0.19)	2.22 (±0.17)	100
	0.005	253 (±39.10)	Spheroid	4.02 (±0.38)	1.59 (±0.42)	87
Short	0.1	96.9 (±11.6)	floc	3.70 (±0.11)	2.06 (±0.56)	100
	0.05	121 (±16.5)	Spheroid	3.93 (±0.16)	1.77 (±0.29)	100
	0.005	294 (±46.9)	Spheroid	1.20 (±0.03)	1.11 (±0.06)	100
Ultrashort	0.1	103 (±21.5)	Spheroid	5.51 (±0.55)	2.10 (±0.14)	98
	0.05	128 (±26.8)	Spheroid	4.58 (±0.32)	2.06 (±0.20)	100
	0.005	304 (±51.0)	Spheroid	1.38 (±0.05)	1.23 (±0.37)	52

[a] Distinct good results are highlighted in grey. [b] Describes if small flocs are suspended in CNF-PSSNa (floc) or form independent granular bodies (spheroids). [c] Relative RNA expression (normalized with control).

3.4 Conclusions

In this chapter, cell flocculation by CNF-CPBs was explained using DLVO theory, which conclusively established that the cell flocculation of CNF-PSSNa depends on the length of CNF. Moreover, different types of cells adhere to the surface of CNF and spontaneously form flocs. The size of the flocs is greatly affected by the concentration and length of CNF-PSSNa. By optimizing the fiber length and concentration of CNF-PSSNa, flocs with a controllable size can be obtained with a high survival rate and enhanced cellular functions. Additionally, the enhancement of liver-specific gene expression by 3D cellular flocculation was confirmed. The method used is very easy to implement and can greatly benefit drug development and in vitro tissue research. Therefore, the technology described in this study can be used as a new 3D culture method for drug discovery and regenerative medicine.

Reference

[1] T. A. Thorpe. History of plant tissue culture. *Molecular biotechnology*, 37(2):169–180, 2007.

[2] S. A. Hudu, A. S. Alshrari, A. Syahida, and Z. Sekawi. Cell culture, technology: enhancing the culture of diagnosing human diseases. *Journal of clinical and diagnostic research: JCDR*, 10(3):DE01, 2016.

[3] B. M. Baker and C. S. Chen. Deconstructing the third dimension–how 3d culture microenvironments alter cellular cues. *Journal of cell science*, 125(13):3015–3024, 2012.

[4] Y. Imamura, T. Mukohara, Y. Shimono, Y. Funakoshi, N. Chayahara, M. Toyoda, N. Kiyota, S. Takao, S. Kono, T. Nakatsura, and H. Minami. Comparison of 2d- and 3d-culture models as drug-testing platforms in breast cancer. *Oncology reports*, 33(4):1837–1843, 2015.

[5] D. Diekjürgen and D. W. Grainger. Polysaccharide matrices used in 3d in vitro cell culture systems. *Biomaterials*, 141:96–115, 2017.

[6] X. Yang, Z. Lu, H. Wu, W. Li, L. Zheng, and J. Zhao. Collagen-alginate as bioink for three-dimensional (3d) cell printing based cartilage tissue engineering. *Materials Science and Engineering: C*, 83:195–201, 2018.

[7] S. Melissaridou, E. Wiechec, M. Magan, M. V. Jain, M. K. Chung, L. Farnebo, and K. Roberg. The effect of 2d and 3d cell cultures on treatment response, emt profile and stem cell features in head and neck cancer. *Cancer cell international*, 19(1):1–10, 2019.

[8] K. Calar, S. Plesselova, S. Bhattacharya, M. Jorgensen, and P. de la Puente. Human plasma-derived 3d cultures model breast cancer treatment responses and predict clinically effective drug treatment concentrations. *Cancers*, 12(7):1722, 2020.

[9] S. Bolognin, M. Fossépré, X. Qing, J. Jarazo, J. Ščančar, E. L. Moreno, S. L. Nickels, K. Wasner, N. Ouzren, J. Walter, et al. 3d cultures of parkinson's disease-specific

dopaminergic neurons for high content phenotyping and drug testing. *Advanced Science*, 6(1):1800927, 2019.

[10] S. A. Langhans. Three-dimensional in vitro cell culture models in drug discovery and drug repositioning. *Frontiers in pharmacology*, 9:6, 2018.

[11] C. Jensen and Y. Teng. Is it time to start transitioning from 2d to 3d cell culture? *Frontiers in Molecular Biosciences*, 7:33, 2020.

[12] K. Matsumura and R. Rajan. Oxidized polysaccharides as green and sustainable biomaterials. *Current Organic Chemistry*, 25(13):1483–1496, 2021.

[13] N. R. E. Putri, X. Wang, Y. Chen, X. Li, N. Kawazoe, and G. Chen. Preparation of plga-collagen hybrid scaffolds with controlled pore structures for cartilage tissue engineering. *Progress in Natural Science: Materials International*, 30(5):642–650, 2020.

[14] W. Shi, M. Sun, X. Hu, B. Ren, J. Cheng, C. Li, X. Duan, X. Fu, J. Zhang, H. Chen, and Y. Ao. Structurally and functionally optimized silk-fibroin–gelatin scaffold using 3d printing to repair cartilage injury in vitro and in vivo. *Advanced materials*, 29(29):1701089, 2017.

[15] S. Tiwari, R. Patil, and P. Bahadur. Polysaccharide based scaffolds for soft tissue engineering applications. *Polymers*, 11(1):1, 2019.

[16] H. Zhu, W. Luo, P. N. Ciesielski, Z. Fang, J. Y. Zhu, G. Henriksson, M. E. Himmel, and L. Hu. Wood-derived materials for green electronics, biological devices, and energy applications. *Chemical reviews*, 116(16):9305–9374, 2016.

[17] Y. Habibi, L. A. Lucia, and O. J. Rojas. Cellulose nanocrystals: chemistry, self-assembly, and applications. *Chemical reviews*, 110(6):3479–3500, 2010.

[18] M. Jorfi and E. J. Foster. Recent advances in nanocellulose for biomedical applications. *Journal of Applied Polymer Science*, 132(14), 2015.

[19] D. A. Gregory, L. Tripathi, A. T. R. Fricker, E. Asare, I. Orlando, V. Raghavendran, and I. Roy. Bacterial cellulose: A smart biomaterial with diverse applications. *Materials Science and Engineering: R: Reports*, 145:100623, 2021.

[20] M. Jonoobi, R. Oladi, Y. Davoudpour, K. Oksman, A. Dufresne, Y. Hamzeh, and R. Davoodi. Different preparation methods and properties of nanostructured cellulose from various natural resources and residues: a review. *Cellulose*, 22(2):935–969, 2015.

[21] M. Bhattacharya, M. M. Malinen, P. Lauren, Y. Lou, S. W. Kuisma, L. Kanninen, M. Lille, A. Corlu, C. GuGuen-Guillouzo, O. Ikkala, et al. Nanofibrillar cellulose hydrogel promotes three-dimensional liver cell culture. *Journal of controlled release*, 164(3):291–298, 2012.

[22] S. A. Wickstroem and C. M. Niessen. Cell adhesion and mechanics as drivers of tissue organization and differentiation: local cues for large scale organization. *Current opinion in cell biology*, 54:89–97, 2018.

[23] R. J. Hickey and A. E. Pelling. Cellulose biomaterials for tissue engineering. *Frontiers in bioengineering and biotechnology*, 7:45, 2019.

[24] W. Chimpibul, T. Nakaji-Hirabayashi, X. Yuan, and K. Matsumura. Controlling the degradation of cellulose scaffolds with malaprade oxidation for tissue engineering. *Journal of Materials Chemistry B*, 8(35):7904–7913, 2020.

[25] C. Yoshikawa, T. Hoshiba, K. Sakakibara, and Y. Tsujii. Flocculation of cells by cellulose nanofibers modified with concentrated polymer brushes. *ACS Applied Nano Materials*, 1(4):1450–1455, 2018.

[26] C. Yoshikawa, J. Qiu, C. Huang, Y. Shimizu, J. Suzuki, and E. van den Bosch. Non-biofouling property of well-defined concentrated polymer brushes. *Colloids and Surfaces B: Biointerfaces*, 127:213–220, 2015.

[27] K. C. Bentz and D. A. Savin. Chain dispersity effects on brush properties of surface-grafted polycaprolactone-modified silica nanoparticles: Unique scaling behavior in the concentrated polymer brush regime. *Macromolecules*, 50(14):5565–5573, 2017.

[28] C. Yoshikawa, K. Sakakibara, P. Nonsuwan, T. Yamazaki, and Y. Tsujii. Nonbiofouling coatings using bottlebrushes with concentrated polymer brush architecture. *Biomacromolecules*, 22(6):2505–2514, 2021.

[29] S. Watanabe, E. Kodama, K. Sakakibara, S. Sasaki, and Y. Tsujii. Effect of surface texturing on the durability of concentrated polymer brushes. *Tribology International*, 155:106668, 2021.

[30] Y. Tsujii, K. Ohno, S. Yamamoto, A. Goto, and T. Fukuda. Structure and properties of high-density polymer brushes prepared by surface-initiated living radical polymerization. *Surface-initiated polymerization I*, pages 1–45, 2006.

[31] T. Morinaga, K. Ohno, Y. Tsujii, and T. Fukuda. Two-dimensional ordered arrays of monodisperse silica particles grafted with concentrated polymer brushes. *European polymer journal*, 43(1):243–248, 2007.

[32] E. Dickinson and L. Eriksson. Particle flocculation by adsorbing polymers. *Advances in Colloid and Interface Science*, 34:1–29, 1991.

[33] T. Ndikubwimana, X. Zeng, N. He, Z. Xiao, Y. Xie, J. Chang, L. Lin, and Y. Lu. Microalgae biomass harvesting by bioflocculation-interpretation by classical dlvo theory. *Biochemical Engineering Journal*, 101:160–167, 2015.

[34] P. Černoch, Z. Černochová, S. Petrova, D. Kaňková, J. Kim, V. Vasu, and A. D. Asandei. Water soluble poly (styrene sulfonate)-b-poly (vinylidene fluoride)-b-poly (styrene sulfonate) triblock copolymer nanoparticles. *RSC advances*, 6(60):55374–55381, 2016.

[35] K. M. Woo, V. J. Chen, and P. X. Ma. Nano-fibrous scaffolding architecture selectively enhances protein adsorption contributing to cell attachment. *Journal of Biomedical Materials Research Part A: An Official Journal of The Society for Biomaterials, The Japanese Society for Biomaterials, and The Australian Society for Biomaterials and the Korean Society for Biomaterials*, 67(2):531–537, 2003.

[36] C. Vila-Parrondo, C. García-Astrain, and L. M. Liz-Marzán. Colloidal systems toward 3d cell culture scaffolds. *Advances in Colloid and Interface Science*, page 102237, 2020.

[37] K. C. Marshall, R. STOUT, and R. Mitchell. Mechanism of the initial events in the sorption of marine bacteria to surfaces. *Microbiology*, 68(3):337–348, 1971.

[38] Y. Adachi. Dynamic aspects of coagulation and flocculation. *Advances in colloid and interface science*, 56:1–31, 1995.

[39] U. Shah, J. de Oliveira Mallia, N. Singh, K. E. Chapman, S. H. Doak, and G. J. S. Jenkins. A three-dimensional in vitro hepg2 cells liver spheroid model for genotoxicity studies. *Mutation Research/Genetic Toxicology and Environmental Mutagenesis*, 825:51–58, 2018.

[40] Z. Darzynkiewicz, D. Galkowski, and H. Zhao. Analysis of apoptosis by cytometry using tunel assay. *Methods*, 44(3):250–254, 2008.

[41] S. Nath and G. R. Devi. Three-dimensional culture systems in cancer research: Focus on tumor spheroid model. *Pharmacology & therapeutics*, 163:94–108, 2016.

[42] K. Schrobback, T. J. Klein, R. Crawford, Z. Upton, J. Malda, and D. I. Leavesley. Effects of oxygen and culture system on in vitro propagation and redifferentiation of osteoarthritic human articular chondrocytes. *Cell and tissue research*, 347(3):649–663, 2012.

[43] K. M. Kulig and J. P. Vacanti. Hepatic tissue engineering. *Transplant Immunology*, 12(3-4):303–310, 2004.

[44] C. A. Wiwi and D. J. Waxman. Mini reviewrole of hepatocyte nuclear factors in growth hormone-regulated, sexually dimorphic expression of liver cytochromes p450. *Growth factors*, 22(2):79–88, 2004.

[45] C. Luckert, C. Schulz, N. Lehmann, M. Thomas, U. Hofmann, S. Hammad, J. G. Hengstler, A. Braeuning, A. Lampen, and S. Hessel. Comparative analysis of 3d culture methods on human hepg2 cells. *Archives of toxicology*, 91(1):393–406, 2017.

[46] K. Nakamura, N. Kato, K. Aizawa, R. Mizutani, J. Yamauchi, and A. Tanoue. Expression of albumin and cytochrome p450 enzymes in hepg2 cells cultured with a nanotechnology-based culture plate with microfabricated scaffold. *The Journal of toxicological sciences*, 36(5):625–633, 2011.

Chapter 4

Control of degradability of aldehyde-introduced oxidized cellulose

The biodegradability of biomaterials is an essential characteristic for evaluating the biocompatibility of a material, which means that the material does not need to be removed by surgery or other methods. [1] Depending on the application, such as drug delivery, implants, tissue engineering scaffolds, etc., there are different requirements for the degradability of the material. Therefore, biomaterials with controlled degradation conditions (for example, time dimension) are important to expand the application. [2–4] In addition to the degradation time, the processability of material and the cytotoxicity of the degradation products also need to be considered. [5]

Cellulose is a green material because it is the most abundant organic compound on the planet and is renewable. [6] Due to its biocompatibility, environmental degradability, and renewable properties. [7] However, cellulose has a weakness, that is, it cannot be degraded in human tissues. [8] In the previous two chapters of the study, materials based on cellulose nanofibers (CNF) were developed to flocculate with cells and have a promising future as 3D culture scaffolds, but the degradation of CNF makes broader applications challenging. Therefore, there is a significant necessity to investigate ways to improve its biodegradability.

Our laboratory investigates the use of Schiff bases to form hydrogels with amino groups (e.g., polyamines) by introducing aldehydes into polysaccharides via a Malaprade oxidation reaction. It has been found that in this system, triggering the Schiff base formation reaction causes a Maillard reaction that breaks down the sugar backbone, thus allowing the hydrogel to break down in vivo. [9] It is thought that cellulose, which has the same glucose unit as a repeating unit, can also be broken down by the above reaction. The biodegradability of polysaccharides, including cellulose, can be conferred by reactions with amino acids abundant in the organism.

The Malaprade reaction is a precise oxidation reaction. It can find adjacent hydroxyl groups to generate a ring-opening product with two aldehyde groups at the C2 and C3 positions of the glucopyranose unit. [10] The characteristic of this reaction is that it can highly retain the material's machinery and structure features. [11] Furthermore, oxidized dextran was degraded by triggering the Maillard reaction, and the resulting products were harmless to the body. [9] In addition, CNF is composed of crystalline regions and amorphous regions. [12] The composition ratio of these two regions affects the degradation control and physical properties of CNF. [13] Therefore, the oxidation and degradation sites in the above reactions also need to be investigated.

In this study, the oxidation of cellulose and CNF with periodate was carried out, and the decomposition of the oxidation products in amino acid solutions was evaluated to better understand and control the decomposition reaction by adjusting the oxidation regulation of periodate. In the future, aldehyde groups can be introduced on the surface of CNF grafted with concentrated polymer brushes to give it the ability to degrade biologically, which can facilitate cellular recycling or in vivo degradation to broaden its application.

4.1 Materials and methods

4.1.1 Materials

Cellulose powder was purchased from Sigma Aldrich, St. Louis, United States. CNF suspension was obtained from Chuetsu Pulp & Paper, Takaoka, Japan. Sodium periodate , iodine solution (0.05 mol/L), sulfuric acid (special grade), sodium hydroxide solution (1 mol/L), sodium thiosulfate solution (0.1 mol/L), soluble starch, glycine were bought from Nacalai Tesque Co., Ltd., Kyoto, Japan.

4.1.2 Fabrication of oxidized cellulose scaffold

Sodium periodate (0.5-7.5 g) and distilled water (50 g) were placed in a 100 ml beaker and stirred at 50°C until the sodium periodate was dissolved. Three g of cellulose powder was added to the solution and the mixture was stirred at 50°C for 1 hour. Then, the mixture was washed with distilled water while filtered. The cellulose oxidized with various concentrations of sodium periodate were placed in silicone rubber molds of a specific size (diameter: 1 cm, depth: 3 mm) and freeze-dried. The surface of freeze-dried oxidized cellulose was then observed using scanning electron microscopy (SEM, TM3030 plus, Hitachi, Japan). The oxidized cellulose (OC) below was referred to as OC-X, where X indicates the concentration of sodium periodate.

4.1.3 Fabrication of CNF hydrogel

CNF suspension (10 g) was placed in a beaker with the surface as flat as possible. Forty g of 5 mol/L sodium hydroxide solution was slowly and carefully added to the beaker to avoid distorting the CNF suspension. The beaker was allowed to stand at room temperature for 12 hours. The weakly gelatinized sample, which had lost its mobility, was then neutralized by immersion in a 4% dilute acetic acid solution for 6 hours and then washed under running water for 12 hours to prepare the CNF hydrogel.

4.1.4 Fabrication of CNF sheet

The 20 g CNF suspension is diluted to a solution concentration of 0.2% and stirred, then filtered by extraction using a membrane filter. After filtration, the non-absorbent side of the concentrate sheet (not the surface of the filter membrane) is pressed onto a PTFE sheet, and the other side is made by stacking three sheets of filter paper on top of the filter membrane. The CNF sheet is made by sandwiching it between brass molds, hot pressing it for 3 to 4 hours (60°C, 10 to 15 MPa), keeping it sandwiched with the molds, and putting it in a dryer machine to dry completely.

4.1.5 Oxidization of CNF sheet and hydrogel

The CNF sheets and hydrogels were cut into 1 cm diameter circles, added to five concentration gradients of 1%-15% sodium periodate solution, and oxidized at 50 °C for 60 minutes. For the CNF sheets, additional experiments were carried out with various times (5-240 minutes) and temperature (70 °C and 90 °C) in a 1% sodium periodate solution, respectively. The oxidized CNF (OCNF) elow was referred to as OCNF-X, where X indicates the concentration of sodium periodate. The water content of the OCNF hydrogel was calculated as the weight of the dried OCNF hydrogel compared to the weight of the OCNF hydrogel after drying the surface water.

4.1.6 Aldehyde introduce rate determination

The prepared OC, oxidized CNF (OCNF) sheets, and OCNF hydrogels were thoroughly dried in oven, and 0.05 g of each sample was placed in a 100 ml beaker with 10 ml of distilled water. As a control, 10 mL of distilled water was added to 100 mL beaker. The aldehyde introduced rate of the prepared samples was assessed by the iodometric method. Briefly,20 mL of a 0.05 mol/L I_2 solution and 20 mL of a 1 mol/L NaOH solution were added to the sample beaker and stirred for 15 minutes. After that, 15 mL of H_2SO_4 (6.25 v/v%) was added, followed by stirring for 1 minute at room temperature. Then 0.1

mol/L $Na_2S_2O_3$ solution was used for titration. Additionally, starch solution was added as an indicator. The calculation of the Aldehyde group introduced rate was given on the chemical equation shown in Figure 4.1, where 1 mol of aldehyde group reacts with 1 mol of I_2 under basic conditions, and 1 mol of I_2 reacts with 2 mol of ${S_2O_3}^{2-}$.

$$I_2 + 3NaOH + R\text{-}CHO = R\text{-}COONa + 2NaI + 2H_2O \qquad (1)$$

$$I_2 + 2Na_2S_2O_3 = Na_2S_4O_6 + 2NaI \qquad (2)$$

Figure 4.1: Reaction equation in iodometry, (1) reaction of aldehyde group with I_2 under basic conditions, (2) Reaction of excess I_2 with $Na_2S_2O_3$.

4.1.7 Degradability of OC and OCNF sheet in glycine

For OC, 0.2g of dry sample was immersed in 1-15% glycine solution, and the reaction was allowed to proceed at room temperature. After reacting for a specified time, OC was filtered with Whatman 42 paper and washed with distilled water 3 times, and dried in a 50 °C oven. The weight of OC before and after the degradation reaction was recorded. In order to simulate the degradation in the biological environment, 0.2 g of OC-10 was soaked in low glucose Dulbecco's modified Eagle's medium (DMEM, Thermo Fisher Scientific, Inc, Massachusetts, United States) containing 10% (v/v) fetal bovine serum (FBS), incubated at 37 °C, and the weight loss was also recorded.

For OCNF sheet, 0.2g of dry sample was soaked in 1-15% glycine solution. The reaction was allowed to proceed at room temperature and reflected the prescribed time. The sample was then filtered with filter paper and dried.

4.1.8 Other measurements

FT-IR measurement was performed on CNF sheet samples oxidized with different concentrations of sodium periodate at 50 °C for 1 hour.

Wide-angle X-ray diffraction (WAXD) analysis was obtained by an automatic multipurpose X-ray diffractometer (XRD) (Smart lab, Rigaku, Tokyo, Japan) over a range of $2\theta = 5$–$30°$. In order to verify the crystallinity index (CI) changes of cellulose and CNF sheet before and after oxidation and degradation reactions, various samples were thoroughly dried in a desiccator and ground into a powder with a mortar, followed by performing WAXD analysis.

The molecular weight change of CNF before and after oxidation reaction and degradation reaction was measured by viscosity method using the ISO 5351/1-1981 standard. Briefly, the CNF sample was added to 0.5M cupri-ethylenediamine (CED) solution and stirred for 30 minutes to prepare cellulose samples with a concentration of 0.005%. Measure the viscosity of different samples with a capillary viscometer. The falling time is counted with a stopwatch, where the falling time of the sample is t, and the falling time of the CED solution is t0. As a calculation, Specific viscosity is defined as

$$\eta_{sp} = t/t_0 - 1 \tag{4.1}$$

The limiting viscosity is defined as

$$\eta = \eta_{sp}/(c(1 + 0.28 \times \eta_{sp})) \tag{4.2}$$

Where c is the number of viscometer.

4.2 Results and Discussion

4.2.1 Oxidized cellulose characterization

Cellulose powder was molded by freeze-dried after an oxidation process. In the case of untreated cellulose and oxidized cellulose with a low oxidant concentration, the powder remains in powder form even after freeze-drying; the higher the concentration of oxidant, the more the freeze-dried oxidized cellulose tends to retain its shape. It is well known that cellulose is held together by intramolecular and intermolecular hydrogen bonding, and therefore dried cellulose powders do not easily fuse by redispersing in water and freeze dried. [14] The fusion of cellulose oxidized with high concentrations of oxidizing agents may occur due to the partial dissolution of the surface due to the oxidation treatment and allows the oxidized cellulose to be placed in specific molds to control the shape as the freeze-dried OC-15 shown in Figure 4.2.

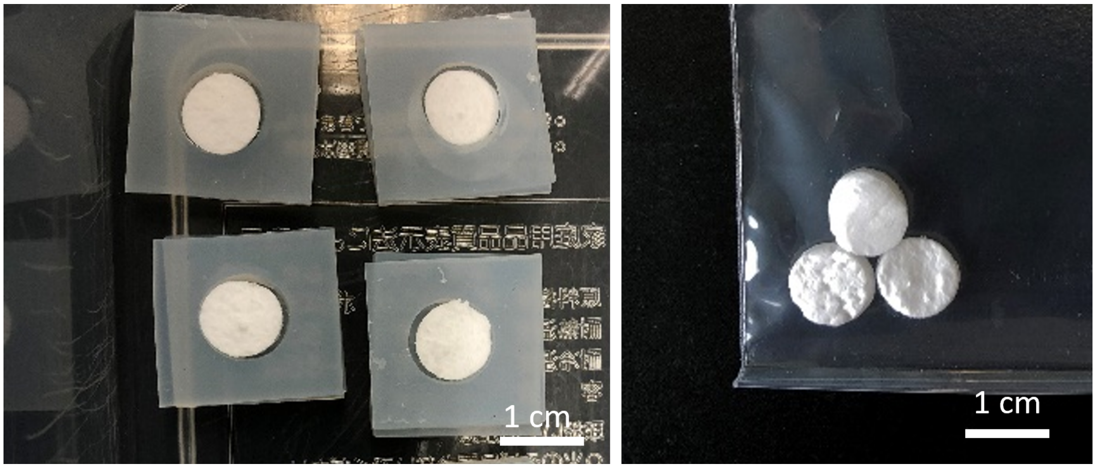

Figure 4.2: Freeze-dried oxidized cellulose powder (OC-15).

The spongy OC was observed using SEM (Figure 4.3). In OC-10 there were pores on the surface, but they were unevenly distributed near the surface. Samples with higher aldehyde introduction rates had larger surface pore sizes compared to OC-10. The required pore size of the scaffold material depends on the application and cell type. Although there is no standard range, materials with pore sizes of 20-1500 μm are commonly used in bone tissue processes, and with a pore size of approximately 2μm have been reported. [15, 16] Thus, the porous properties of OC-10, OC-12, and OC-15 may allow cells to access the interior for growth.

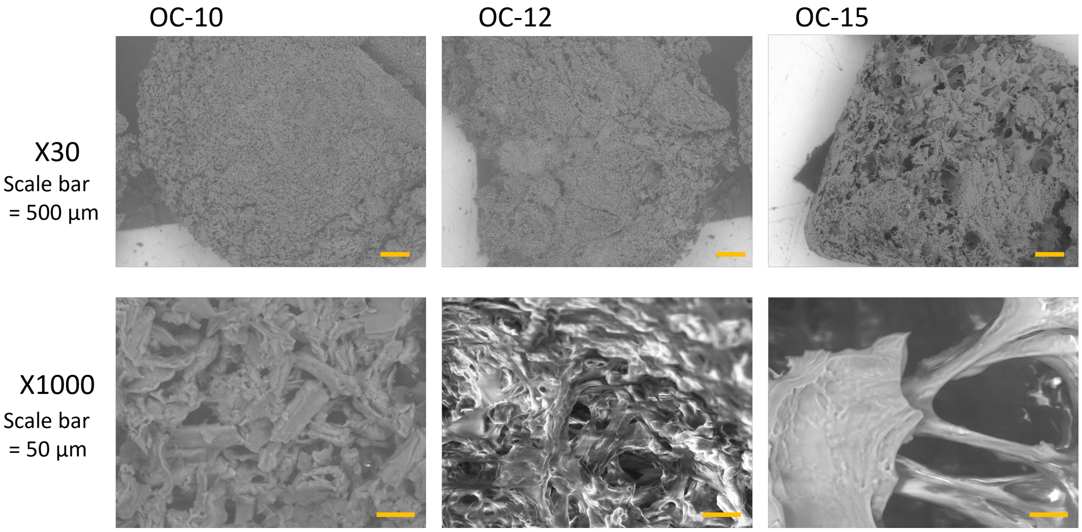

Figure 4.3: SEM images of OC oxidized with different concentrations of $NaIO_4$ in various magnification.

4.2.2 Aldehyde introduction rate of oxidized cellulose

The sodium periodate oxidation breaks the bond at the C2-C3 position of the glucose unit of the cellulose repeating unit and introduces the aldehyde group. The rate of introduction of the aldehyde group was determined by iodine titration. Figure 4.4 shows the aldehyde group introduction rates of OC at different concentrations of the oxidizing agent. The rate of aldehyde introduction increases with increasing concentrations of sodium periodate. The rate of aldehyde introduction was lowest at 10.95% when oxidized with 1% periodate and increased to 81.57% when the oxidant concentration was 15%. This suggests that the rate of aldehyde introduction can be controlled by the concentration of the oxidant.

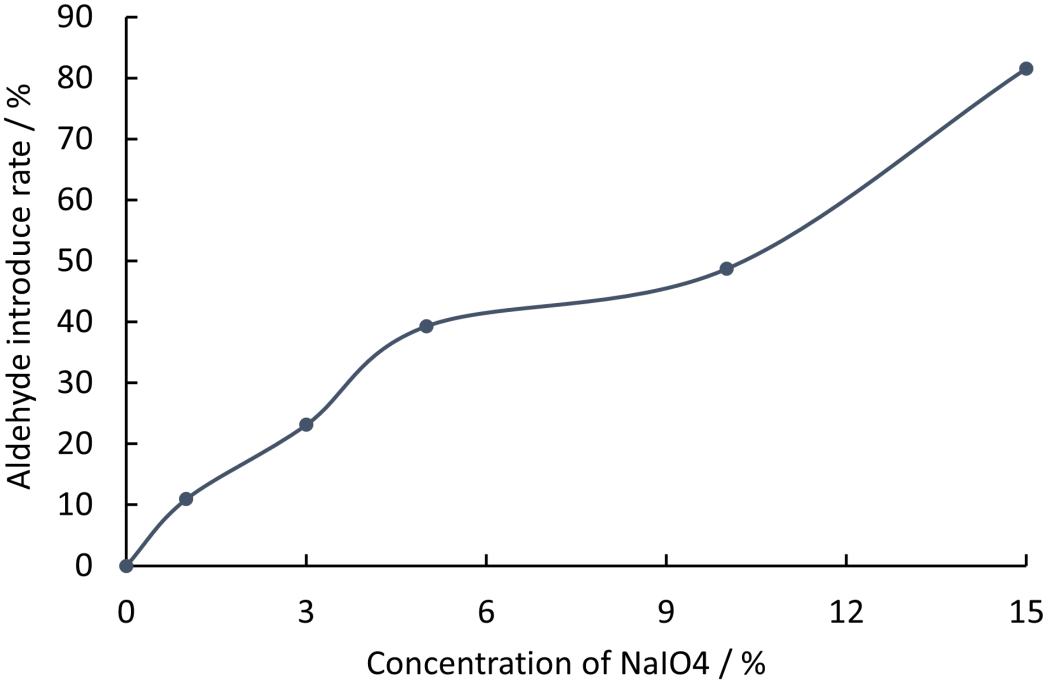

Figure 4.4: The aldehyde introduction rate varies of cellulose with the concentration of $NaIO_4$.

4.2.3 Degradation of oxidized cellulose

To verify the effect of the aldehyde introduction rate on the degradation of OC in glycine. The weight loss of OCs with different aldehyde introduction rates in the 5% of glycine solution with degradation time is shown in Figure 4.5. It can be seen that, overall, the degradation does not continue over 4 days, but rather the weight plateaus after a relatively rapid reaction (about 24 hours), which indicates that the degradation reaction will be concentrated on the first day. On the other hand, as the aldehyde introduction rate increased, more weight was lost. At an aldehyde introduction rate of 81.57%, OC was dissolved entirely in the 5% glycine solution. In contrast, at an aldehyde introduction rate of 10.95%, the weight loss was just under 10%. Furthermore, it was observed that the 81.57% sample with a higher aldehyde introduction rate reached the top of the curve before the 48.7% sample, which may be since the high aldehyde introduction rate led to a reduction in hydrogen bonding in the OC, which allowed the amino acids to penetrate easily into the OC and therefore the reaction rate was higher. This confirms that the rate of aldehyde group introduction can control the weight loss of OC in amino acids.

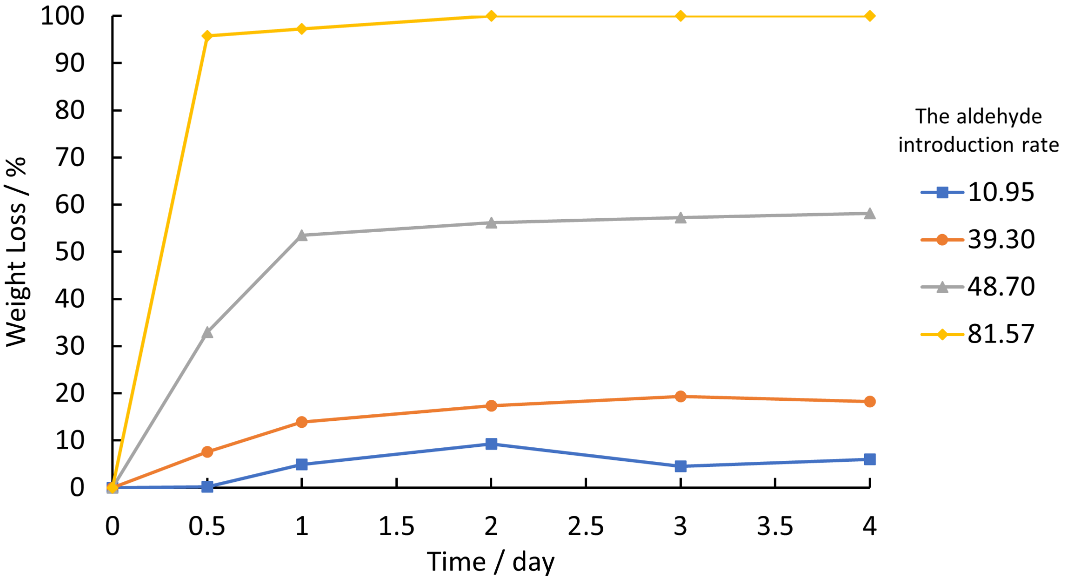

Figure 4.5: Weight loss of oxidized cellulose with various aldehyde introduction rates in 5% glycine solution in different culture time.

To verify the effect of aldehyde group introduction rate and glycine concentration on the solubility of oxidized cellulose in glycine as amino acid, different OC were placed into different concentrations of glycine solution to observe the decomposition status. The Figure shows the visual results of the solubility state of OC-15 (81.57% aldehyde introduction rate) after 24 hours of immersion in glycine solutions at 0-15% concentration. OC-15 was dissolved entirely in the 1-15% glycine solution within 24 hours. In distilled water (0%), the cellulose oxide retains its shape. The higher the concentration of the glycine solution, the darker the color of the solution in which the cellulose oxides are dissolved. The color reaction is most likely a colored substance resulting from the Maillard reaction during the breakdown of cellulose, which is evidence that the decomposition process involves a Maillard reaction.

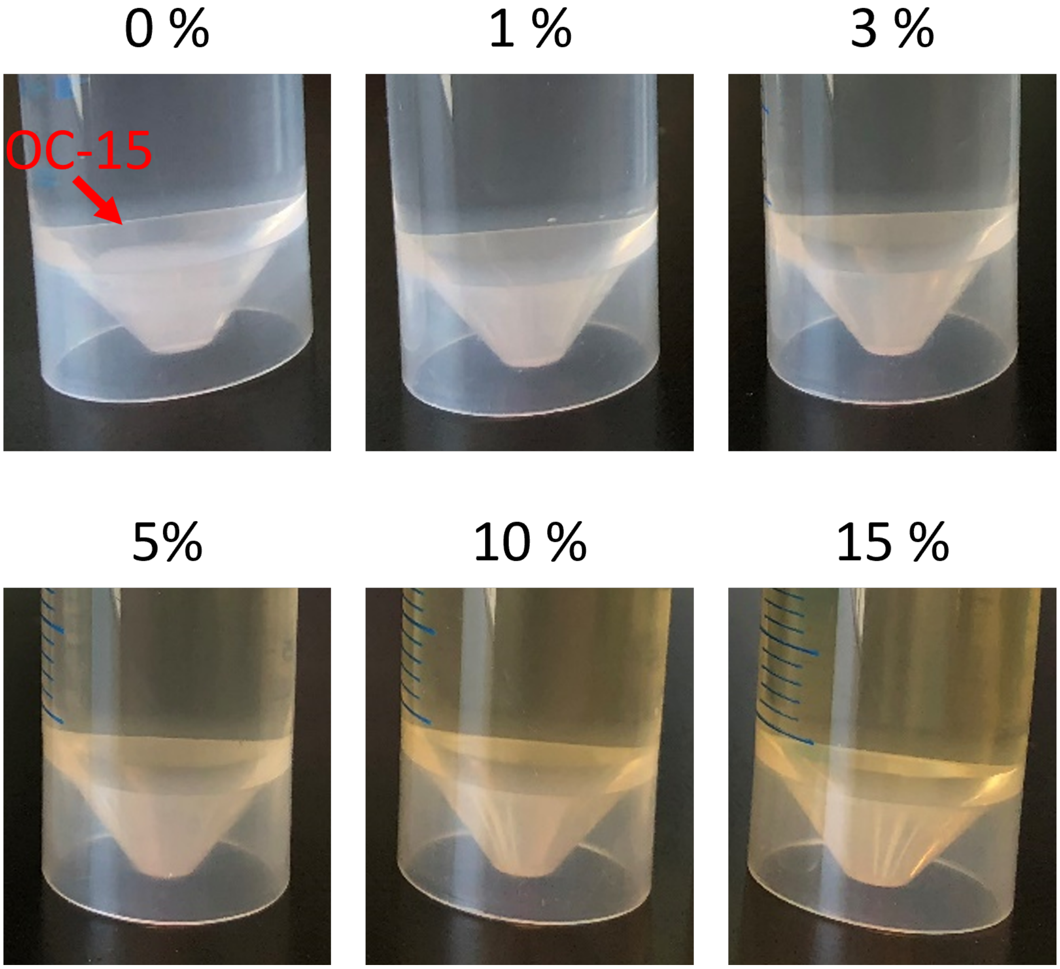

Figure 4.6: Images of OC-15 in different concentration of glycine after depredated 24 hours.

Figure 4.7 shows the weight loss of OC-15 at different glycine concentrations as a function of degradation time. It can be seen that OC-15 wasessentially completely degraded within 120 minutes in both 10% and 15% glycine solutions. Conversely, the rate of degradation of OC-15 decreased with decreasing amino acid concentrations. In the 1% glycine solution, OC-15 reached 100% weight loss after approximately 25 hours. The results demonstrate that amino acid concentration can also OC degradation rate. The higher the amino acid concentration, the faster the OC degradation.

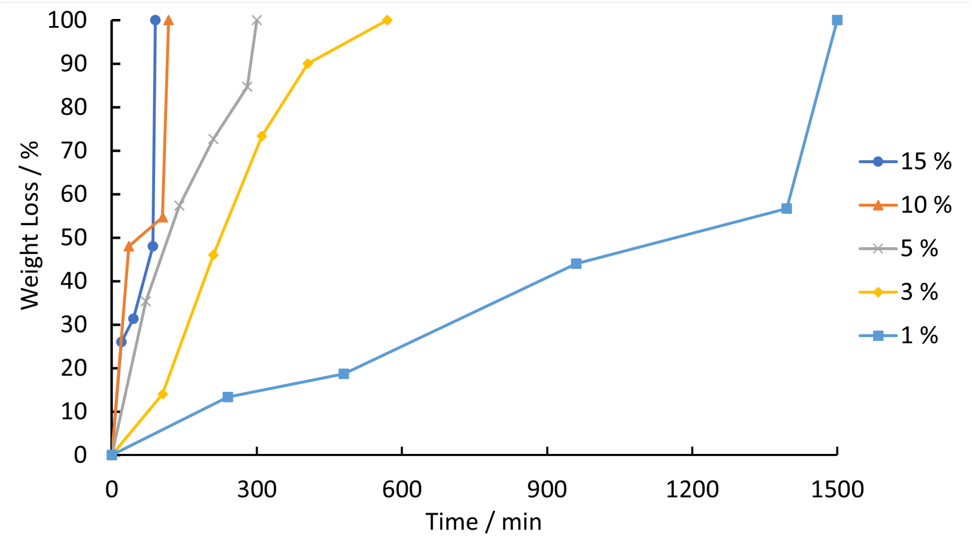

Figure 4.7: Weight loss of OC-15 at room temperature in different concentrations of glycine.

To verify the degradation of OC in the in vitro culture environment, OC-10 was immersed in cell culture medium, containing 10% FBS. Figure 4.8 show the undissolved fraction as a result of drying. The change of the sample from white to brown is also evidence of a Maillard reaction. The weight loss over time is shown in Figure 4.9. Similar to in the glycine solution, the reaction peaked and remained constant in weight loss within 1 day, and the maximum weight loss of OC-10 in DMEM was similar to that in 5% glycine, both around 60%.

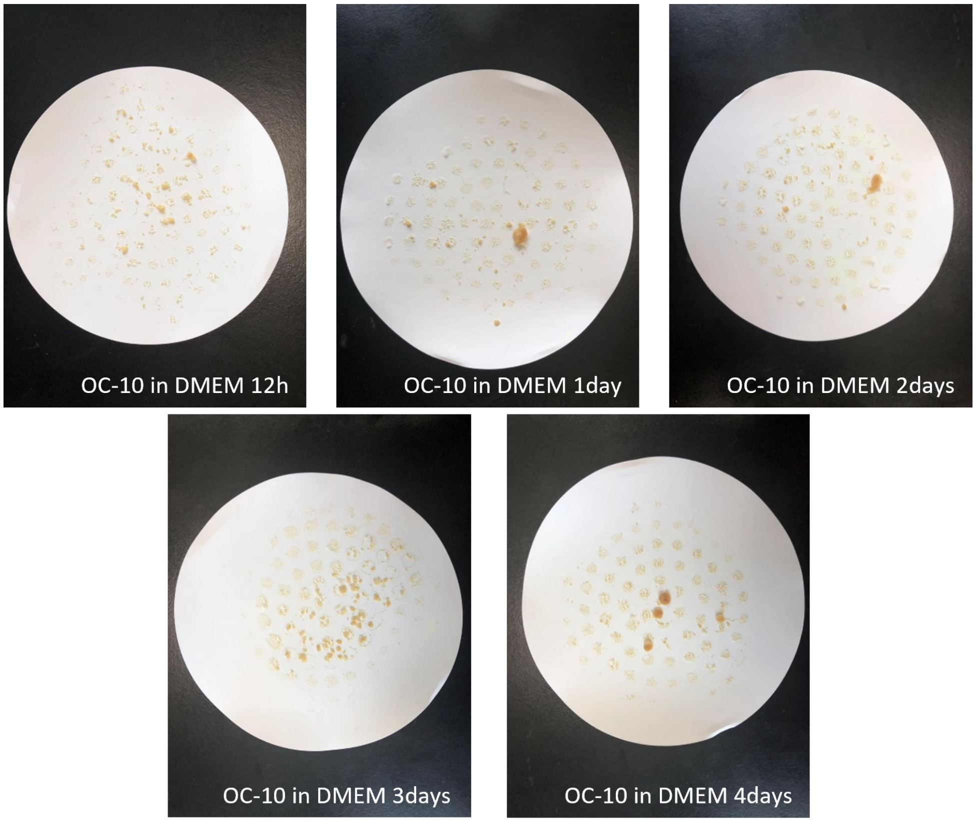

Figure 4.8: Images of OC-10 degraded in DMEM with different time.

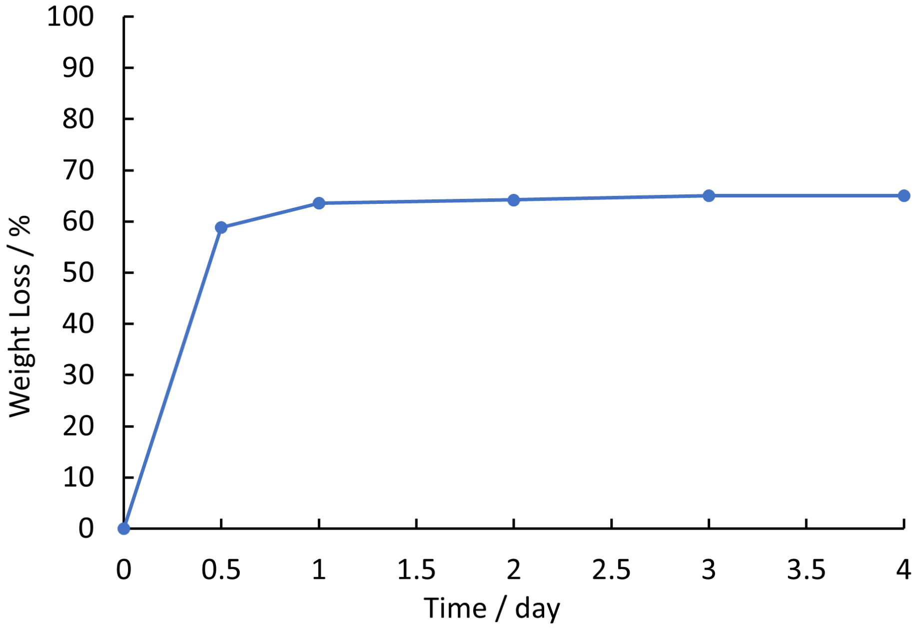

Figure 4.9: Weight loss of OC-10 in DMEM with different time.

4.2.4 Characterization of OCNF hydrogel

It has been confirmed that oxidized cellulose can be degraded in glycine and cell culture media and can be adjusted by the introduction rate of aldehyde groups. The subsequent research is mainly based on sheets and hydrogel made by CNF. Focus on confirming the changes in the molecular weight and crystallinity of cellulose during the entire reaction. For OCNF hydrogel, As shown in Figure 4.10, the introduction rate of aldehyde groups increased as the concentration of sodium peroxide increased. When the sodium peroxide concentration is 15%, the aldehyde group introduction rate of CNF hydrogel is about 80%. The size change and water content of CNF hydrogel after oxidation reaction are shown in Figure 4.11. As the degree of oxidation increases, the size and water content of CNF hydrogels decrease. This may be because the hemiacetal formed by the combination of aldehyde groups shortened the distance between CNF chains.

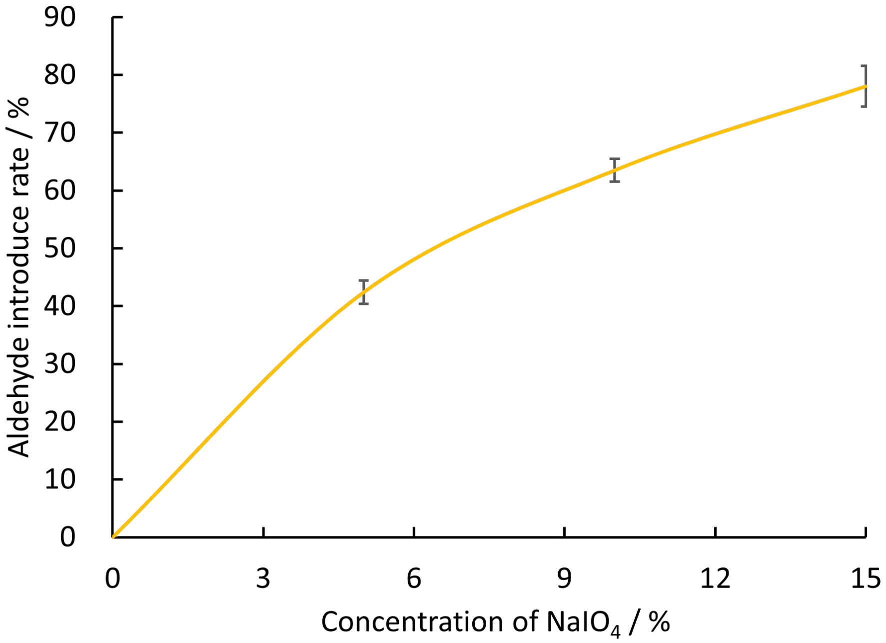

Figure 4.10: The aldehyde introduction rate varies of CNF hydrogel with the concentration of NaIO$_4$.

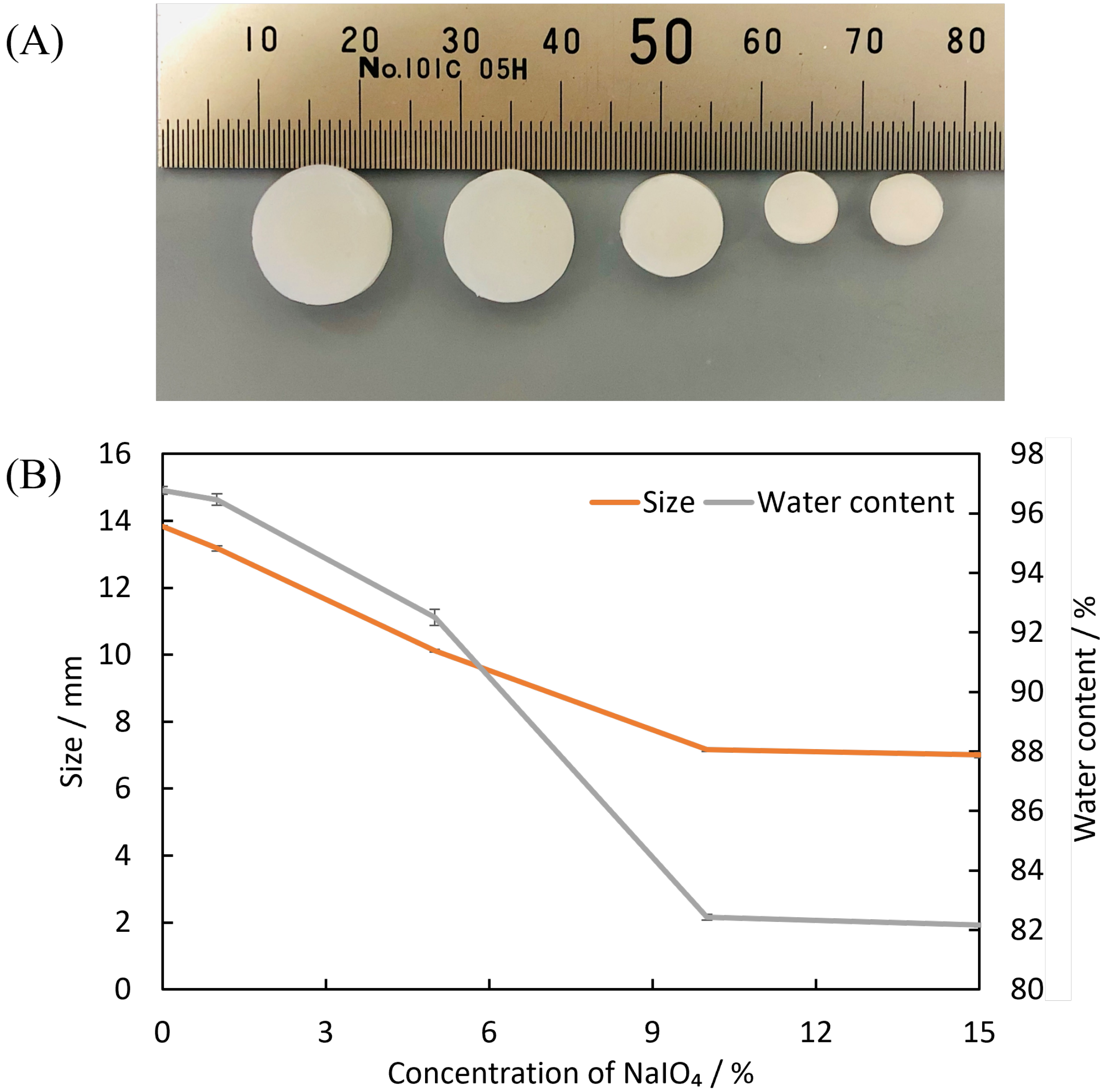

Figure 4.11: (A)Image of OCNF hydrogel, (B) size and water content of OCNF hydrogel in different concentration of $NaIO_4$.

4.2.5 Characterization of oxidized CNF sheet

A CNF sheet with a thickness of 2μm has been made. After the oxidation reaction, the aldehyde group introduction rate of the OCNF sheet is shown in Figure 4.12. The aldehyde introduction rate of the OCNF sheet oxidized under the same conditions is 52% relative to the maximum 80% aldehyde group introduction rate of the OCNF hydrogel. This may be due to the fact that the sheet is obtained by pressing. Compared with the small specific surface area of the hydrogel, sodium periodate is more challenging to penetrate and contact the CNF inside the sheet.

The FTIR results of OCNF sheets with different aldehyde introduction rates are shown in Figure 4.13. As the degree of oxidation increases, two characteristic peaks appear at 1740 and 880 cm^{-1}. The peak near 1740 cm^{-1} is attributed to the carbonyl, group. [17] and the peak around 880 cm^{-1} has some shift with the increase of oxidation degree. This peak should be attributed to the formation of hemiacetal bonds between aldehyde groups and adjacent hydroxyl. groups. [18] The two characteristic peaks increased with the increase of oxidation degree, which proves the results of the aldehyde group introduction rate.

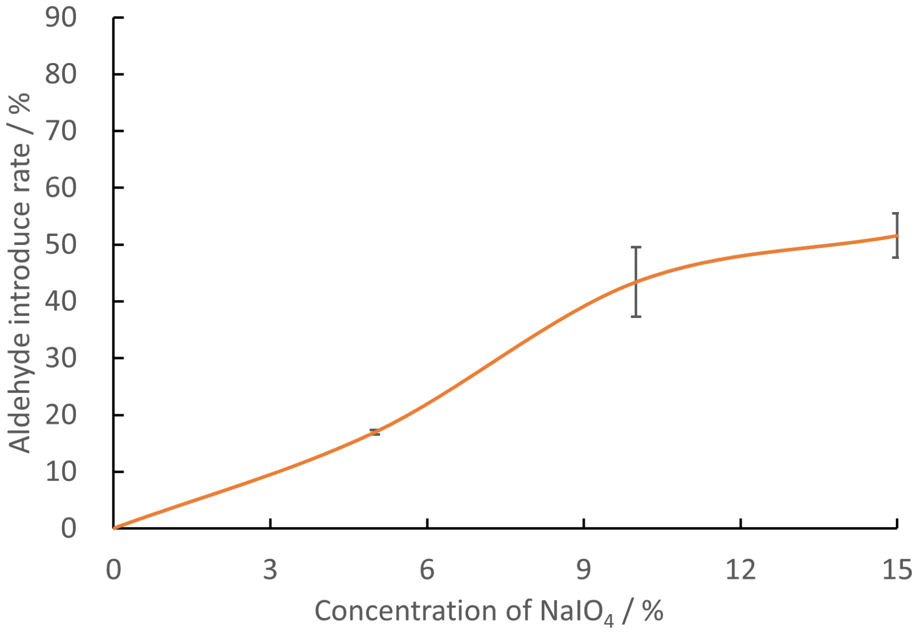

Figure 4.12: The aldehyde introduction rate varies of CNF sheet with the concentration of $NaIO_4$.

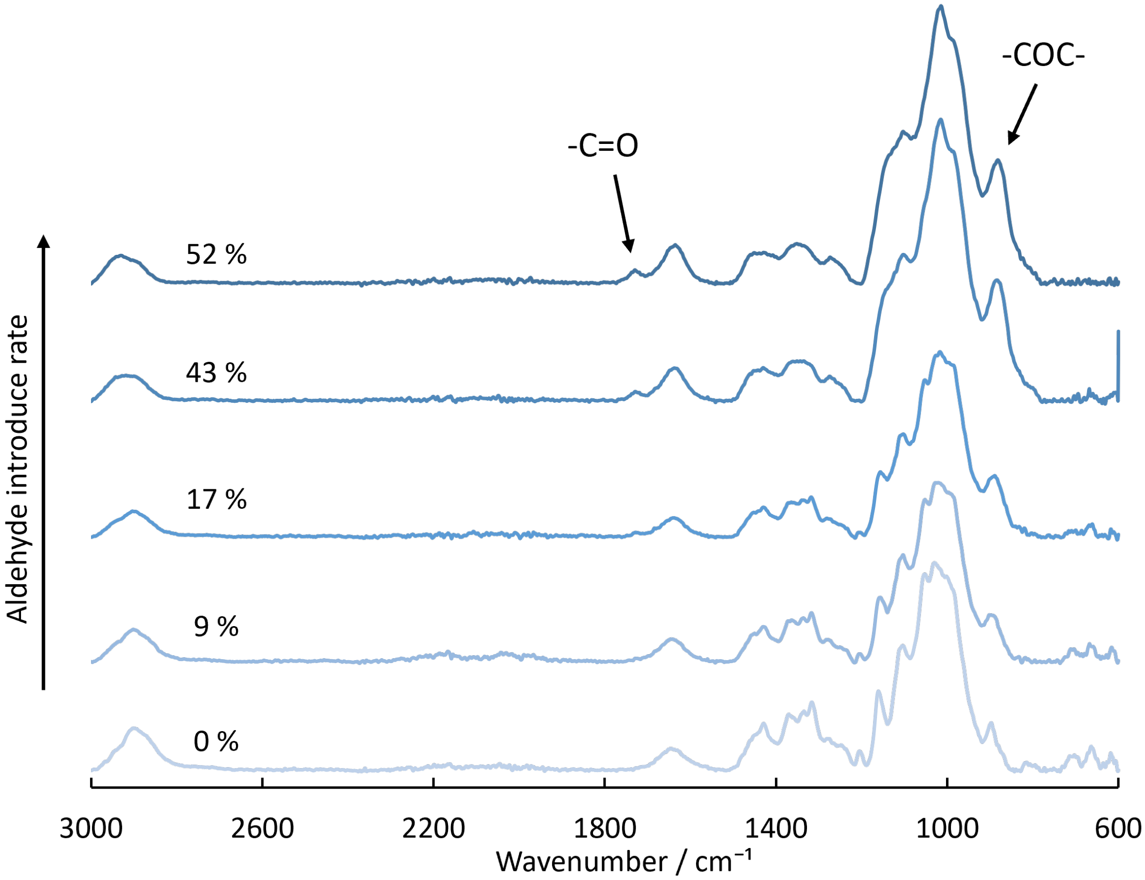

Figure 4.13: FT-IR results of OCNF sheet with various aldehyde introduction rate.

4.2.6 Changes in molecular weight of CNF sheet

The two most common techniques for measuring the molecular weight (degree of polymerization) of cellulose are viscometry and gel permeation chromatography (GPC). Since the viscometry method is simple to perform and has been extensively validated, it is also more tolerant of measuring cellulose (and possibly lignin) of plant. origin. [19] Therefor the molecular weight of CNF sheets is measured by dissolving the cellulose in a CED solution. The degree of polymerization is calculated from the limiting viscosity *eta* obtained from the viscosity measurement,

$$DP = \eta/K \tag{4.3}$$

The constant value K=0.57. The molecular weight of CNF is simply calculated as DP×162.14 (molecular weight of glucose residue). The result of viscosity determination is shown in Figure 4.14. It can be seen that periodic acid will rapidly reduce the molecular weight of CNF at the beginning of the oxidation reaction and increase the concentration of periodic acid. Both the reaction time and the reaction temperature can further reduce the molecular weight of CNF. The reaction time decreased rapidly in the first hour and then tended to be flat. As for the reaction temperature, it can be seen that the molecular weight has dropped by about half when the reaction temperature is 90 °C relative to 50 °C. In contrast, increasing the concentration of periodic acid is the most significant reduction in CNF molecular weight. Reacting at 50 °C in 15% periodic acid for one hour reduces the molecular weight of CNF to about 1/54.

In order to verify the molecular weight change of OCNF during degradation. The OCNF sheet, which was reacted in 10% periodic acid for 1 hour at 50°C, was placed in a 5% glycine solution. The molecular weight change with degradation time is shown in Figure 4.15. The molecular weight drops rapidly in the first 5 hours and then remains stable. It shows that the degradation reaction based on Schiff base reaction on OCNF is a relatively fast process.

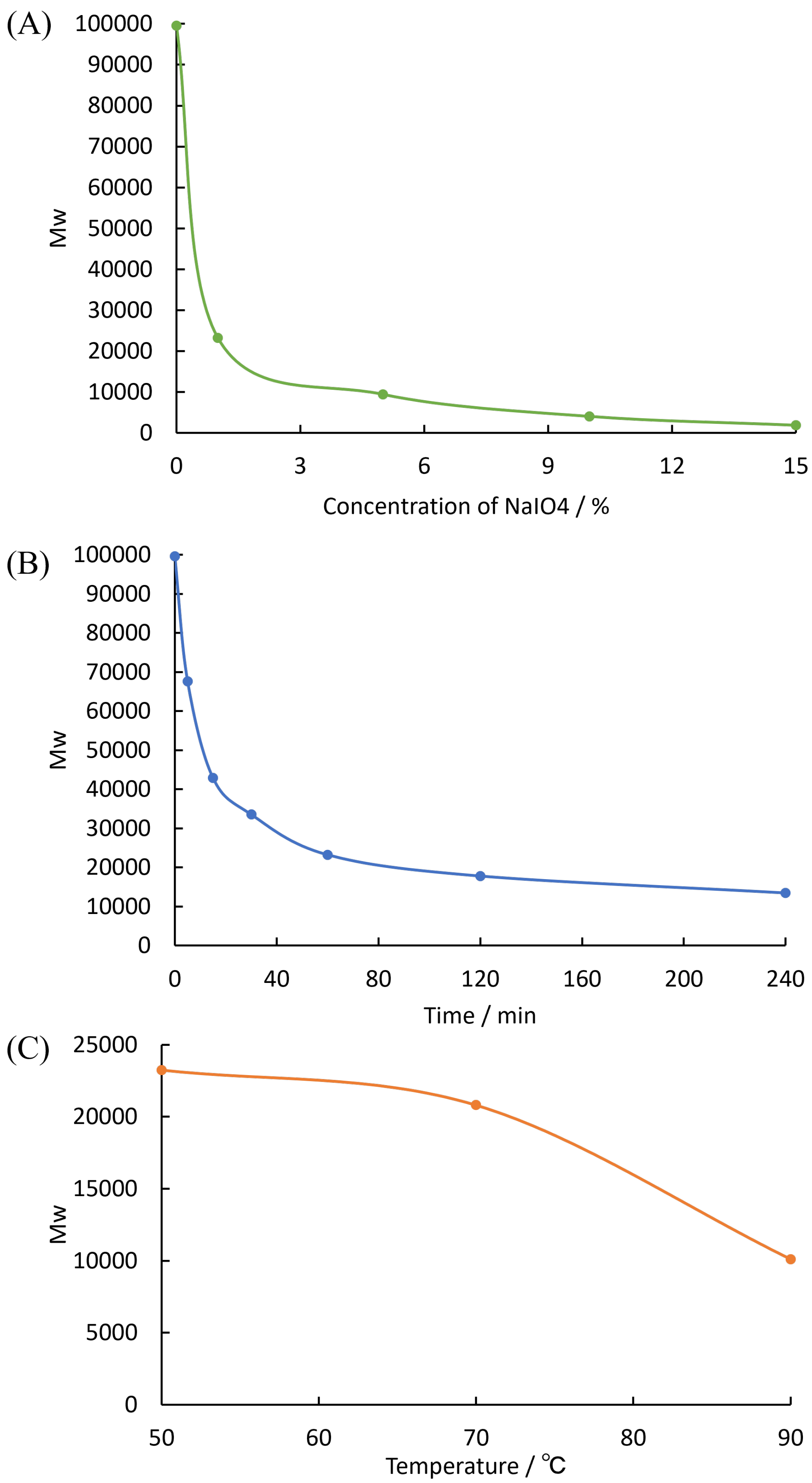

Figure 4.14: Molecular weight of OCNF sheet oxidized with different (A) concentration at 50 ℃ for 1 hour, (B) time in 1% $NaIO_4$ at 50 ℃, and (C) temperature in 1% $NaIO_4$ for 1 hour.

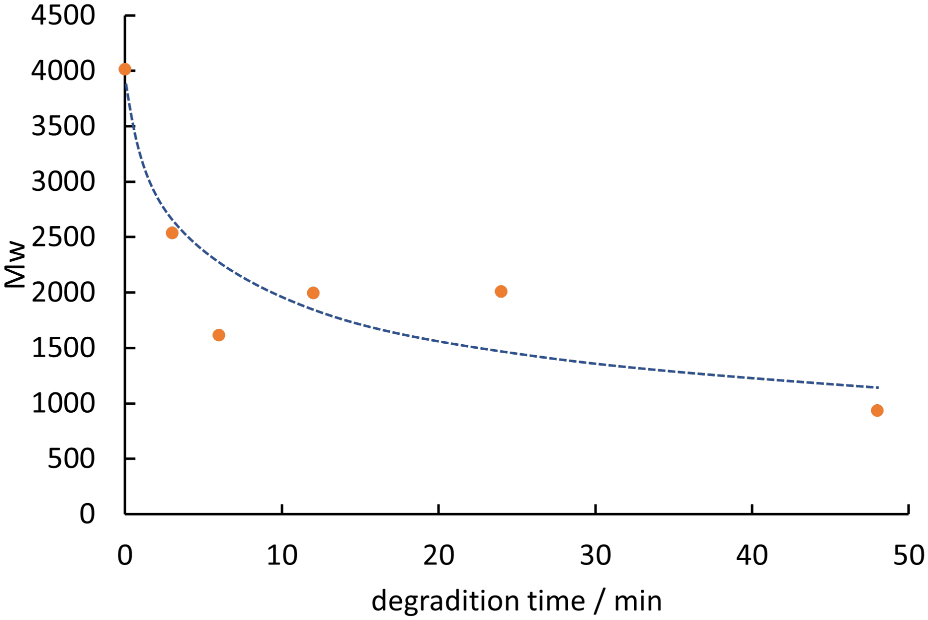

Figure 4.15: Molecular weight of OCNF-10 sheet during the degradation in 5% glycine. The dashed line is the approximate curve.

4.2.7 Changes in crystallinity index (CI) of CNF sheet

CNF contains crystalline (ordered) and amorphous (disordered) regions. The reactivity of these two regions in the periodate acidification and degradation reactions is very worthy of determination. Generally speaking, the amorphous area is more likely to react with acid, so the amorphous area can be removed by acid hydrolysis to obtain nano-sized cellulose nanocrystals. [20]

In this study, WAXD measurement was carried out on CNF sheet according to convention. [21] The resulting peaks were fitted by the deconvolution method. Four crystalline peaks (101, 10I, 021, and 002) were separated by the Voigt function. CI was calculated from the ratio of the area of all crystalline peaks to the total area. Figure 4.16 shows the effect of different concentrations of periodic acid acidification on the CI of CNF sheet. It can be seen that as the degree of oxidation increases, the molecular weight decreases while the CI also decreases. This shows that periodic acid can react with the crystalline area and reduce CI. The CI changes during the decomposition process. As shonw in Figure 4.17, OCNF sheets oxidized with 5% and 10% periodic acid that were degraded in 5% glycine, respectively. During the decomposition process, the molecular weight of OCNF decreased, but the CI increased significantly. Especially for OCNF oxidized by 10% periodic acid, its CI increased from 0.36 to 0.84, which was a significant change. The above results prove that CNF sheet degradation caused by the Schiff base mainly occurs in the amorphous region.

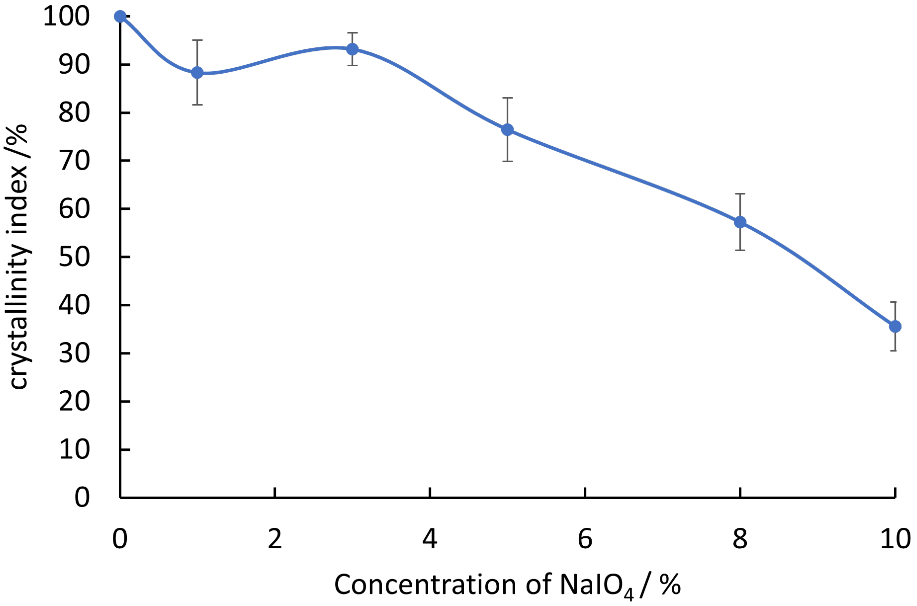

Figure 4.16: CI of OCNF sheet with defferent concentration of NaIO$_4$ at 50 ℃ for 1 hour.

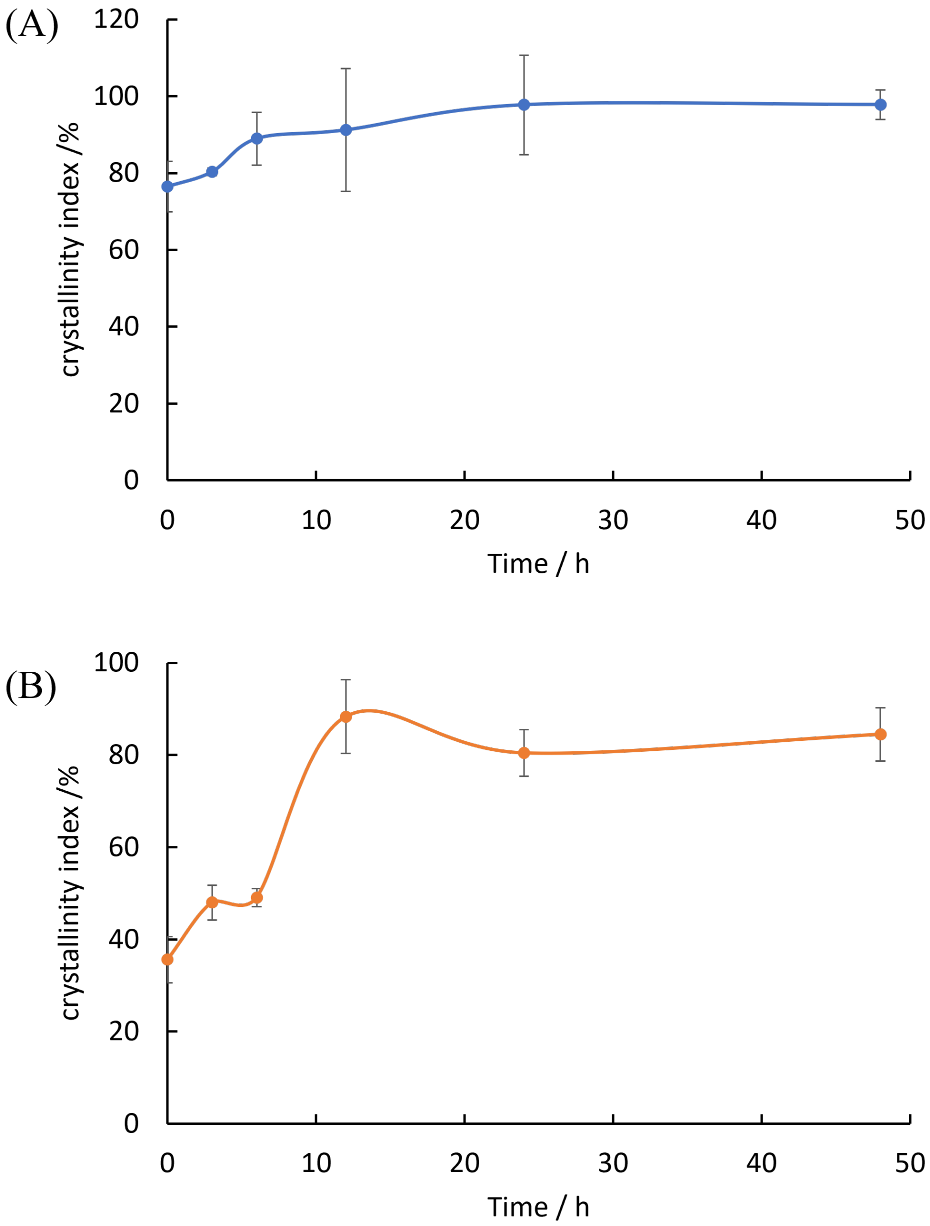

Figure 4.17: CI of OCNF sheet degraded in 5% glycine for 48 hours, (A) OCNF-5 and (B) OCNF-10.

4.3 Conclusions

In this study, cellulose powder and CNF were used in order to precisely control the degradation in the body through the Malaprade reaction. The effects of various reaction conditions on the degradability, as well as the changes in the molecular weight of CNF and CI in the process, were studied.

The porous material using OC was made based on the Malaprade reaction and had holes that allowed cells to grow. By adjusting the concentration of sodium periodate, the introduction rate of aldehyde groups can be controlled, and the increase of the introduction rate of aldehyde groups can increase the weight loss of OC in amino acids. Moreover, the degradation reaction rate increases with the increase of glycine concentration. Through research on CNF, it is found that CNF is allowed to be endowed with biodegradability in the same way. In the oxidation reaction, the molecular weight decreases significantly, and the trend of change is inversely proportional to the amino group introduction rate, which can be carried out in the air by changing the reaction temperature, reaction time, and sodium periodate concentration. During the degradation process, the molecular weight of CNF does not decrease significantly. Finally, the oxidation reaction based on sodium periodate can react with the crystalline area and cause the CI to decrease, and the subsequent Schiff base reaction reacts more with the non-qualitative area to increase the CI. Providing CNF with biodegradability can significantly broaden its applications, such as intelligent cell scaffolds that facilitate the recovery of cultured cells in vitro or implantation in the body. The results of the changes in the molecular weight and CI of CNF in the Malaprade and Schiff base reaction can allow for better design and development of new biomaterials based on CNF.

Reference

[1] B. D. Ulery, L. S. Nair, and C. T. Laurencin. Biomedical applications of biodegradable polymers. *Journal of polymer science Part B: polymer physics*, 49(12):832–864, 2011.

[2] L. S. Nair and C. T. Laurencin. Biodegradable polymers as biomaterials. *Progress in polymer science*, 32(8-9):762–798, 2007.

[3] P. Grossen, D. Witzigmann, S. Sieber, and J. Huwyler. Peg-pcl-based nanomedicines: A biodegradable drug delivery system and its application. *Journal of Controlled Release*, 260:46–60, 2017.

[4] M. Martina and D. W. Hutmacher. Biodegradable polymers applied in tissue engineering research: a review. *Polymer International*, 56(2):145–157, 2007.

[5] A. W. Lloyd. Interfacial bioengineering to enhance surface biocompatibility. *Medical device technology*, 13(1):18–21, 2002.

[6] S. J. Eichhorn, A. Dufresne, M. Aranguren, N. E. Marcovich, J. R. Capadona, S. J. Rowan, C. Weder, W. Thielemans, M. Roman, S. Renneckar, et al. Current international research into cellulose nanofibres and nanocomposites. *Journal of materials science*, 45(1):1–33, 2010.

[7] S. Kalia, A. Dufresne, B. M. Cherian, B. S. Kaith, L. Avérous, J. Njuguna, and E. Nassiopoulos. Cellulose-based bio-and nanocomposites: a review. *International journal of polymer science*, 2011, 2011.

[8] Y. Huang, C. Zhu, J. Yang, Y. Nie, C. Chen, and D. Sun. Recent advances in bacterial cellulose. *Cellulose*, 21(1):1–30, 2014.

[9] W. Chimpibul, T. Nagashima, F. Hayashi, N. Nakajima, S. Hyon, and K. Matsumura. Dextran oxidized by a malaprade reaction shows main chain scission through a maillard reaction triggered by schiff base formation between aldehydes and amines. *Journal of Polymer Science Part A: Polymer Chemistry*, 54(14):2254–2260, 2016.

[10] A. G. Vlessidis and N. P. Evmiridis. Periodate oxidation and its contribution to instrumental methods of micro-analysis—a review. *Analytica chimica acta*, 652(1-2):85–127, 2009.

[11] Y. Deng, T. G. Nevell, R. J. Ewen, and C. L. Honeybourne. Sulfur poisoning, recovery and related phenomena over supported palladium, rhodium and iridium catalysts for methane oxidation. *Applied Catalysis A: General*, 101(1):51–62, 1993.

[12] A. C. O'sullivan. Cellulose: the structure slowly unravels. *Cellulose*, 4(3):173–207, 1997.

[13] Z. Peter. Order in cellulosics: Historical review of crystal structure research on cellulose. *Carbohydrate Polymers*, page 117417, 2020.

[14] W. Tian, X. Gao, J. Zhang, J. Yu, and J. Zhang. Cellulose nanosphere: Preparation and applications of the novel nanocellulose. *Carbohydrate Polymers*, page 118863, 2021.

[15] C. M. Murphy, M. G. Haugh, and F. J. O'brien. The effect of mean pore size on cell attachment, proliferation and migration in collagen–glycosaminoglycan scaffolds for bone tissue engineering. *Biomaterials*, 31(3):461–466, 2010.

[16] Q. L. Loh and C. Choong. Three-dimensional scaffolds for tissue engineering applications: role of porosity and pore size. 2013.

[17] Q. G. Fan, D. M. Lewis, and K. N. Tapley. Characterization of cellulose aldehyde using fourier transform infrared spectroscopy. *Journal of Applied Polymer Science*, 82(5):1195–1202, 2001.

[18] P. Calvini, A. Gorassini, G. Luciano, and E. Franceschi. Ftir and waxs analysis of periodate oxycellulose: evidence for a cluster mechanism of oxidation. *Vibrational Spectroscopy*, 40(2):177–183, 2006.

[19] R. Kumar, G. Mago, V. Balan, and C. E. Wyman. Physical and chemical characterizations of corn stover and poplar solids resulting from leading pretreatment technologies. *Bioresource technology*, 100(17):3948–3962, 2009.

[20] V. Favier, H. Chanzy, and JrY Cavaillé. Polymer nanocomposites reinforced by cellulose whiskers. *Macromolecules*, 28(18):6365–6367, 1995.

[21] M. Siller, H. Amer, M. Bacher, W. Roggenstein, T. Rosenau, and A. Potthast. Effects of periodate oxidation on cellulose polymorphs. *Cellulose*, 22(4):2245–2261, 2015.

Chapter 5

General Conclusion

In this study, through systematic conditional design, firstly, the DLVO theory was used to explain the flocculation phenomenon of CNF and cells based on grafted concentrated polymer brushes. Secondly, the degradation of CNF based on the Malaprade reaction and Maillard reaction was explored.

In Chapter 2, four concentrated polymer brushes (CPBs) with different zeta potentials were successfully grafted on CNF (CNF-CPBs) as PSSNa, PAA, PDMAEMA, and PDMTAC. The zeta potential was found to be decisive for flocculation by cellular experiments. Among them, cationic CNF-CPBs caused cell death. For anionic CNF-CPBs, floc size increased with increasing incubation time, and floc size increased with decreasing concentration. The former proved that the cells kept growing, while the latter was due to the fact that more CNF-CPBs were wrapped around the cells in higher concentrations and larger flocs were difficult to form because of the charge repulsion between the cells wrapped with CNF-CPBs. On the other hand, PSSNa with a lower zeta potential formed larger flocs with the cells compared to CNF-PAA, demonstrating that a suitable zeta potential can promote cell flocculation. Moreover, CNF-PSSNa was further investigated in Chapter 3 using CNF-PSSNa as it can form larger flocs and enhance cell function.

The effect of fiber length on the flocculation of CNF-CPBs with cells was demonstrated in Chapter 3, where PSSNa was grafted onto each of the five fiber lengths of CNF in the form of concentrated polymer brushes and was well characterized. Three types of cells were used to culture with CNF-PSSNa. The results of the cell cultures demonstrated that the floc size became larger when the fiber length was reduced. The spatial repulsion of CNF-CPBs was considered to explain this flocculation phenomenon and when long CNF-PSSNa was adsorbed onto the cell surface, the cells were more difficult to approach each other because of the combined effect of charge repulsion and spatial repulsion.

The explanation of the flocculation phenomenon in Chapters 2 and 3 is consistent with that described by the DLVO theory. More importantly, the three cells demonstrate the same flocculation phenomenon, demonstrating the universality of the theoretical explanation and suggesting the possibility of future application to a wider range of cell lines. Further results demonstrate that when CNF-CPBs-based cells are flocculated, the cells can be uniformly dispersed in the flocs and cell function can be enhanced.

In Chapter 4, cellulose and CNF are oxidized by the Malaprade reaction to improve the biocomposition properties. For cellulose, which can be made porous by periodate acidification and freeze-drying, the aldehyde group introduced by the oxidation reaction can react with glycine in a Schiff base reaction and trigger the Maillard reaction to break the main chain. The rate of aldehyde group introduction affects the cellulose weight loss and the glycine concentration is related to the rate of degradation. A CNF sheet was then produced, and it was verified that CNF can also be degraded by the above reactions. The molecular weight of CNF decreases rapidly during the oxidation reaction and the oxidant concentration has the greatest effect on the molecular weight change. Amorphous domains make the crystallinity of CNF increase.

This thesis provides two different methods of modifying CNF to improve its cellular adsorption and decomposition. Both techniques were investigated by changing the conditions in order to precisely regulate them. These studies will contribute to the future development of CNF-based biomaterials. In future research, a combination of both techniques can be employed to produce CNF-CPBs with biomass degradation properties for applications such as the development of 3D cell culture systems.

Achievement

Conferences

- Yuan X., Matsumura K.

  2019 Annual conference of the Society of Fiber Science and Technology Japan, ,5th-7th Jun. 2019, Tokyo

  Degradability control of cellulose peroxide and its application to scaffolding materials

- Yuan X., Matsumura K.

  68th Symposium on Macromolecules, 25th-27th Sep.2019, Fukui

  Decomposition control of aldehyde-introduced cellulose

- Yuan X., Matsumura K.

  World Biomaterials Congress 2020 Virtual, 11th-15th Dec. 2020, Online

  Study on scaffold materials using biodegradable aldehyde-introduced cellulose

- Yuan X., Nonsuwan P., Sakakibara K., Matsumura K., Yoshikawa C.

  10th Hokushin'etsu Block Research Presentation (Japanese Society for Biomaterials), 19th Jan. 2021, Online

  3D culture system development using cellulose nanofibres modified with concentrated polymer brushes

- Yuan X., Nonsuwan P., Sakakibara K., Matsumura K., Yoshikawa C.

  43rd Annual Meeting of the Japanese Society for Biomaterials, 28th-30th Nov. 2021, Nagoya

  Development of 3D culture system using concentrated polymer brush-modified cellulose nanofibers

Papers

- Yuan X., Nonsuwan P., Shobo M., Rajan R., Yamazaki T., Sakakibara K., Matsumura K., Yoshikawa C. Cellular flocculation using concentrated polymer brush-modified cellulose nanofibers with different fiber lengths. DOI:10.1021/acs.biomac.1c01424 (in press)
- Yuan X., Yoshikawa C., Nonsuwan P., Sakakibara K., Matsumura K. Cellular Flocculation of Cells with Cellulose Nanofibers Surface-Modified with Concentrated Polymer Brushes: Effect of Surface Charge. (in preparation)

Other Publication

- Chnimpibul W., Nakaji-Hirabayashi T., Yuan X., Matsumura K. Controlling the degradation of cellulose scaffolds with Malaprade oxidation for tissue engineering. *Journal of Materials Chemistry B* **2020**, *8*(35), 7904-7913.

Acknowledgment

In a flash it has been five years and I would like to thank for all the encounters.

First of all, I would like to thank my instructor, Prof. Kazuaki Matsumura. Without him, I would not be the person I am today. He helped me revise my research direction and research lineage and provided me with many pertinent suggestions. In terms of life, my teacher also gave me a lot of help to make my study abroad life smoother. Prof. Matsumura is a rigorous-minded researcher who always has great patience with students. Every time I talked with Prof. Matsumura could help me to solve the confusion at that stage. He has always provided me with careful guidance and unfailing support throughout my semester and Ph.D. It is my good fortune to be in Prof. Matsumura's laboratory.

Secondly, I would like to thank our assistant professor Robin Rajan, a respectable researcher, and a reliable friend. I would like to thank Prof. Robin for accompanying me in my daily research to discuss my research and to help me solve my problems. He has a passion for research and bright ideas, and his interactions with me are always beneficial and give me a clearer understanding of my research work.

I would like to thank Dr. Chiaki Yoshikawa for providing me with a valuable internship opportunity and her help in my subsequent research. She is a great teacher who is very rigorous in her research and easy to get along with in life. Thanks to Dr. Yoshikawa, I was able to broaden the direction of my research and learn to be more academically rigorous. This research would not have been possible without the encounter with Dr. Yoshikawa. I would also like to thank Dr. Sakakibara for his great help during the writing and revision of my paper.

I would like to thank my Ph.D. defense committee members, Prof. Kaneko, Prof. Matsumi, and Associate Prof. Miyako, who provided me with valuable suggestions and comments to help me improve my thesis. I would also like to thank my partners in the Matsumura Laboratory for their support and help in giving me memories of these five years of happy research life. In particular, I would like to thank Dr. Punnida Nonsuwan, for her help in my research so that I could finish this research successfully.

It has been my dream to come to Japan to study Since I was a child, and I am grateful to my family and relatives who made my caprice possible. Especially my parents, Ms. Jinrong Qu and Mr. Fengli Yuan, raised me with their hardworking hands; and with their kind hearts, they set the right outlook for me. They always give their time and support my capriciousness, and I am lucky to be born into such a family. I would also like to thank my parents-in-law, Ms. Hong Xu and Mr. Min Guo, together with my parents, who supported me and encouraged me so that I could finish my education successfully.

It has been 6 years since I came to Japan, and I am grateful to my wife, Ms. Jing-Yu Guo, who has always been by my side. She is kind, intelligent, beautiful, and action-oriented. Her sparkle always attracts me, and I always find it beneficial to have a meeting of minds with her. She is also the one who encouraged me to take up the challenge of a Ph.D. I would like to take this opportunity to thank her for meeting and staying with me. I think I am a person who owes a lot to my friends. I am grateful for all the encounters I had in Japan and for my friends who never left me and let me experience the warmth of friendship again and again.

I came across the Rotary Yoneyama Memorial Scholarship when I was most in need financially. The Rotary Yoneyama Memorial Scholarship is not only about the money but also about the friends and Rotarians I have met and the experiences I have had that go beyond the money. I am incredibly grateful to Mr. Maeda, my counselor, and Mr. Shimizu, Mis. Hori, as well as everyone at the Nomi Rotary Club. I would like to thank the Rotary Yoneyama Memorial Scholarship Program.

Finally, I would like to take this opportunity to inspire myself to keep my heart in the right place and move forward despite the many difficulties of life. But do good things and don't ask questions about what's ahead. Everything is for a better future.